MaineDOT

Transportation Research Division

Technical Report 17- 4

Experimental Evaluation and Design of Unfilled and Concrete-Filled FRP Composite Piles

Task 7 – Final Report - Thesis

Final Report – Task 7, January 2017

Technical Report Documentation Page

1. Report No. ME 17-4	2.	3. Recipient's Accession No.	
4. Title and Subtitle Experimental Evaluation and Design of Unfilled and Concrete-Filled FRP Composite Piles Task 7 – Final Report - Thesis		5. Report Date May 2015	
		6.	
7. Author(s) Dale Lawrence		8. Performing Organization Report No.	
9. Performing Organization Name and Address University of Maine – Advanced Structures and Composites Center		10. Project/Task/Work Unit No.	
		11. Contract © or Grant (G) No. Contract # 20130731*535	
12. Sponsoring Organization Name and Address Maine Department of Transportation		13. Type of Report and Period Covered	
		14. Sponsoring Agency Code	
15. Supplementary Notes			

16. Abstract (Limit 200 words)

The overall goal of this project is the experimental evaluation and design of unfilled and concrete-filled FRP composite piles for load-bearing in bridges. This report covers Task 7, Final Report - Thesis.

This final report covers Tasks 1, 2, 3, 5 & 6: Mechanical properties, pile driving and dynamic testing, flexural testing, laminate durability testing, and axial compression testing.

17. Document Analysis/Descriptors Bridge piles, fiber reinforced polymer composites		18. Availability Statement	
19. Security Class (this report)	20. Security Class (this page)	21. No. of Pages 163	22. Price

EXPERIMENTAL EVALUATION OF FIBER REINFORCED POLYMER

PILES IN LOAD-BEARING APPLICATIONS

By

Dale Lawrence

B.S. University of Maine, 2013

A THESIS

Submitted in Partial Fulfillment of the

Requirements for the Degree of

Master of Science

(in Civil Engineering)

The Graduate School

The University of Maine

May 2015

Advisory Committee:

Thomas Sandford, Associate Professor of Civil and Environmental Engineering,

Co-Advisor

Roberto Lopez-Anido, Professor of Civil and Environmental Engineering,

Co-Advisor

Xenia Rofes, Structural Engineer, P.E.

THESIS ACCEPTANCE STATEMENT

On behalf of the Graduate Committee for Dale Lawrence we affirm that this manuscript is the final and accepted thesis. Signatures of all committee members are on file with the Graduate School at the University of Maine, 42 Stodder Hall, Orono, Maine.

Thomas Sandford	Date

Associate Professor of Civil and Environmental Engineering

Co-Advisor

Roberto Lopez-Anido	Date

Professor of Civil and Environmental Engineering

Co-Advisor

LIBRARY RIGHTS STATEMENT

In presenting this thesis in partial fulfillment of the requirements for an advanced degree at The University of Maine, I agree that the Library shall make it freely available for inspection. I further agree that permission for "fair use" copying of this thesis for scholarly purposes may be granted by the Librarian. It is understood that any copying or publication of this thesis for financial gain shall not be allowed without my written permission.

Signature:

Date:

EXPERIMENTAL EVALUATION OF FIBER REINFORCED POLYMER

PILES IN LOAD-BEARING APPLICATIONS

By: Dale Lawrence

Thesis Co-Advisors: Thomas Sandford and Roberto Lopez-Anido

This study was conducted to evaluate the performance of fiber reinforced polymer (FRP) piles in load-bearing applications for the Maine Department of Transportation, with the purpose of assessing pile strength, drivability, and durability. FRP piles were driven at a site between Richmond and Dresden, ME along the Kennebec River with dense glacial soils including cobbles and boulders. These piles were 12.2 m (40 ft) in length with a nominal diameter of 610 mm (24 in) and manufactured using a [0/45/90/-45] degree stitched E-glass fabric and a polyester resin. Piles were tested as concrete-filled samples with 4 layers of reinforcing fabric and a nominal thickness of 12.7 mm (0.5 in) or hollow samples with 8 layers of reinforcing fabric and a nominal thickness of 25.4 mm (1 in). One of the hollow piles had a 1.22 m (4 ft) concrete plug cast at its toe prior to pile driving. A Delmag D36-32 open ended diesel hammer with a maximum rated energy of 123 kN-m (90,560 ft-lbs) was used to drive piles to a target capacity of 2670 kN (600 kips). After driving, piles were extracted to document damage and evaluate residual properties using flexural and axial compression tests.

During driving, piles experienced varying levels of damage. Hollow piles exhibited a brooming failure at the head and the toe after encountering hard driving. The pile with a concrete plug at its toe experienced less severe damage at its toe than the hollow piles. The concrete-filled pile did not show signs of damage in the field, but the concrete-FRP bond failed during flexural testing. All piles achieved a geotechnical capacity over 1780 kN (400 kips).

Driven and extracted piles were brought to the University of Maine Advanced Structures and Composites Center to be tested in flexure and compared with undriven and load-cycled piles. Driving and cyclic loading did not appear to affect the stiffness of concrete-filled or hollow piles. There was no apparent loss in capacity due to driving or cyclic loading, but trends were ultimately inconclusive due to the small sample size and scatter of the data. Both piles that received hammer blows while filled with concrete lost composite action during flexural testing, indicating that additional reinforcement may be required for driving concrete-filled FRP piles.

Driven and undriven pile sections were also proof loaded in axial compression to 4450 kN (1000 kips). Hollow piles did not show any change in behavior due to driving, but trends in the concrete-filled piles were inconclusive due to differences in concrete age.

Mechanical and geotechnical properties of the FRP material were examined using flat FRP plates with 2 layers of reinforcing fabric and a nominal thickness of 6.4 mm (0.25 in). This testing established compressive, tensile, and shear properties along with interface friction values using three different granular soils (Ottawa sand, MaineDOT

Type B aggregate backfill, and glacial till) at two different relative densities (50% and 75%).

The FRP material was tested to verify compliance with the American Association of State Highway and Transportation Officials Guide Specification for Design of Bonded FRP Systems for Repair and Strengthening of Concrete Bride Elements [1] durability requirements. The material did not meet minimum property retention requirements.

ACKNOWLEDGEMENTS

TABLE OF CONTENTS

LIST OF TABLES

LIST OF FIGURES

CHAPTER 1 INTRODUCTION AND OBJECTIVES

1.1 Background of FRP Piles in Load-Bearing Applications

Although composite piles have existed for over 25 years, the piling industry has mostly used materials including timber, concrete, and steel over this period. However, these piles are susceptible to corrosion, rot, or attack by marine borers [2]. Fiber reinforced polymer (FRP) piles may provide improved durability performance over these materials. Additionally, this material can be tailored to optimize the orientation and magnitude of strength properties [3].

As composite materials have become more cost effective, they have made their way from high performance applications in the aerospace and defense industries into infrastructure [4]. Currently, limited data is available on full scale driving and laboratory testing of FRP piles, with even less data available for piles driven in dense glacial soils. Historically, steel H-piles have been used in Maine to accommodate unforgiving subsurface conditions that can include cobbles, boulders, dense soils, and hard bedrock. This study intends to provide insight on the durability, driving, and structural response of FRP piles driven in glacial soils of Maine, resulting in recommendations for their use in load-bearing applications.

1.2 Goals and Scope of Research

This research program has been broken into five categories: mechanical and geotechnical properties of the FRP material, drivability of FRP piles in Maine soils, residual properties of driven and cyclically loaded FRP piles tested in flexure, residual

properties of driven piles tested in axial compression, and durability properties of the FRP material.

Testing for mechanical properties was conducted on composite consisting of a stitched E-glass fabric and polyester resin to evaluate moduli, stresses, and strains of the FRP material for use in predictive models. FRP plates with 2 layers of reinforcing and a nominal thickness of 6.4 mm (0.25 in) were used to characterize the properties of hollow piles with 8 layers of reinforcement with a nominal thickness of 25.4 mm (1 in) and concrete-filled piles with 4 layers of reinforcement with a nominal thickness of 12.7 mm (0.5 in). These properties also serve as the baseline properties for environmental durability testing.

The interface friction angle of the FRP pile material was determined using a modified direct shear test. The bottom of the direct shear box was replaced with a flat FRP plate. Three different soils were tested on the FRP surface to produce characteristic values of interface friction for use in skin friction calculations.

Field installation of hollow and concrete-filled FRP piles was performed to evaluate their driving performance in glacial soils typical of Maine. A diesel hammer with a rated energy of 123 kN-m (90.6 kip-ft) was used to drive piles with a nominal length of 12.2 m (40 ft) and nominal diameter of 610 mm (24 in) to a target capacity of 2670 kN (600 kips). This experienced was used to examine limitations associated with the driving of FRP piles and their suitability for use in Maine. Piles were extracted to document damage and tested in flexure and axial compression.

Flexural testing was used to determine the ultimate moment capacity of the FRP piles and evaluate the effects of pile driving and cyclic loading. These tests included 2 undriven and 1 driven hollow FRP piles and 2 undriven, 1 driven, and 2 load-cycled concrete-filled piles.

Axial compression testing was used to proof load 1.52 m (5 ft) FRP pile sections to 4450 kN (1000 kips). Changes in the behavior of FRP piles due to driving were also examined.

FRP samples were conditioned in an alkali solution, water bath, freeze-thaw chamber, and ultraviolet light/condensation humidity chamber according to the American Association of State Highway and Transportation Officials (AASHTO) [1]. Changes in the tensile properties and glass transition temperature of FRP plates with 2 layers of reinforcement were monitored during testing. AASHTO requires that these samples retain 85% of their baseline properties after each environmental conditioning.

Ultimately, the results of these tests will be implemented to produce geotechnical and structural design specifications and construction specifications for the use of FRP piles in load-bearing applications by the Maine Department of Transportation.

CHAPTER 2 MECHANICAL PROPERTIES OF FRP PLATES

2.1 Description of FRP Material

The fiber reinforced polymer (FRP) composite used in this test program consists of a stitched E-glass fabric with a 0/45/90/-45 fiber architecture (Vectorply E-QX 10200 [5]) and a "pre-promoted unsaturated polyester resin" (CCP Composites STYPOL 040-8084 [6]). The infused reinforcing fabric with a sequence of 0/45/90/-45 was modeled as one layer. Flat FRP plates constructed with 2 layers of reinforcement, having a nominal thickness of 6.4 mm (0.25 in), were used to make coupons for testing. The coupons represent FRP piles constructed of 4 layers of reinforcement (concrete-filled piles), having a nominal thickness of 12.7 mm (0.5 in), or 8 layers of reinforcement (hollow piles), having a nominal thickness of 25.4 mm (1 in). Both in the piles and plates, all layers were placed in the same direction. Layers of all FRP plates and piles were always stacked with the 0 degree fibers orientation on the top, creating an asymmetric but balanced laminate. A summary of the fiber orientation can be seen in Table 2.1.

Table 2.1 Fabric Layup

Fiber Orientation	Percent by Areal Weight[a]
0°	50.5
45°	17.7
90°	14.1
-45°	17.7

[a] Given by Vectorply [5]

Tension, compression, and shear coupons were all tested in the longitudinal and hoop direction. The terms longitudinal and hoop refer to the orientation of the 0 degree fibers which also coincides with the longitudinal and hoop direction of the full scale FRP

piles. This is presented graphically in Figure 2.1. Glass transition temperature testing was only conducted in the hoop direction due to the high modulus of the material.
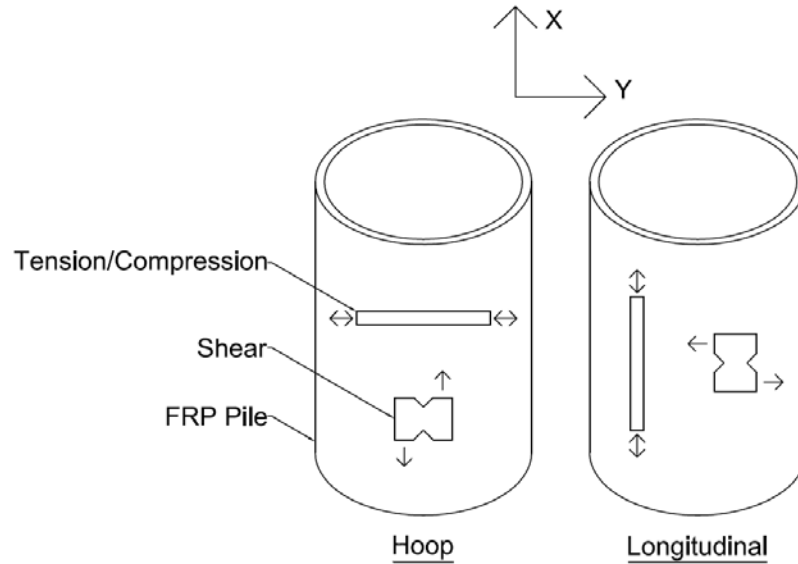
Figure 2.1 Orientation of Coupons for Mechanical Testing

All coupons were cut using a Flow Mach4 4020b abrasive cutting machine to the dimensions specified in their corresponding American Society for Testing and Materials (ASTM) standard. After cutting, all coupons were conditioned at 23 °C (73 °F) and 50% relative humidity for a minimum of 3 days prior to testing. Tension, Compression, and Shear testing was conducted using an Instron 8801 test frame and Instron Dynacell +/- 100 kN (22 kip) load cell. Glass transition temperature testing was conducted using a Thermal Analysis Instruments DMA Q800 dynamic mechanical analyzer.

2.2 Strain Measurement

Strains were monitored using ARAMIS [7] digital image correlation software with 1.3 megapixel cameras. Strain measurements were taken parallel and perpendicular to the loading direction at a frequency of 1 Hz. The ARAMIS system collected strain data

over the entire gage length of the samples by tracking the movement of dots in a black

and white, painted speckle pattern. The data was then trimmed to eliminate strain

concentrations at the edges of the sample and near the grips. The strains presented are the

average value over the area of interest. An example of the speckle pattern and strain field

created by ARAMIS software can be seen in Figure 2.2.

(a)   (b)
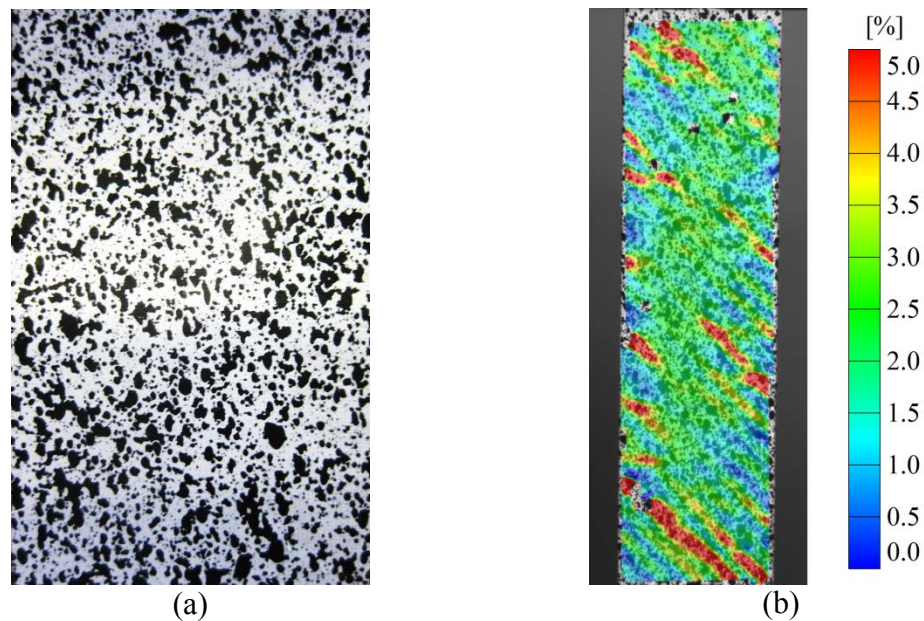
Figure 2.2 ARAMIS Speckle Pattern (a) and Strain Field (b)

The ARAMIS system is sensitive to vibrations created by nearby laboratory

activity, hydraulic systems, and temperature and humidity control systems. This can

create an error in strain measurement of approximately +/- 500 microstrain. The error is

relatively small in the direction of loading, but it will be larger when measuring strains

perpendicular to loading.

2.3 Tensile Properties

All tensile testing was conducted in accordance with ASTM D3039 [8]. Twelve tension coupons were tested in the longitudinal orientation and another twelve coupons were tested in the hoop orientation.

Some longitudinal tension samples slipped in the grips during testing with a maximum available gripping pressure of approximately 17.3 MPa (2.5 ksi). Grit paper was added to the grips of the Instron testing machine to limit slipping of the sample during tests. Several longitudinal tension samples were discounted due to slipping in the grips. The test fixture can be seen in Figure 2.3.

Figure 2.3 Tension Test (ASTM D3039)

Hoop tension samples showed a bi-linear stress-strain relationship. Elastic modulus and Poisson's ratio were calculated using a strain range of 1000 to 3000 microstrain to capture the initial slope of the stress-strain curve. The results of longitudinal and hoop tension tests can be seen in Table 2.2.

Table 2.2 Tension Test Results

Test	Statistic	Ultimate Stress (MPa)	Ultimate Strain (µstrain)	Modulus (GPa)	Poisson's Ratio
Longitudinal Tension	Mean	530	2.56E+04	22.5 (E_x)	0.31 (ν_{xy})
	Std. Dev.	11	9.85E+02	0.5	0.04
	COV	2.1%	3.9%	2.4%	13.6%
Hoop Tension	Mean	174	2.27E+04	13.7 (E_y)	0.17 (ν_{yx})
	Std. Dev.	8	1.10E+03	1.03+02	0.04
	COV	4.5%	4.9%	5.2%	21.5%

Stress-strain plots of longitudinal and hoop tension tests can be seen in Figure 2.4.
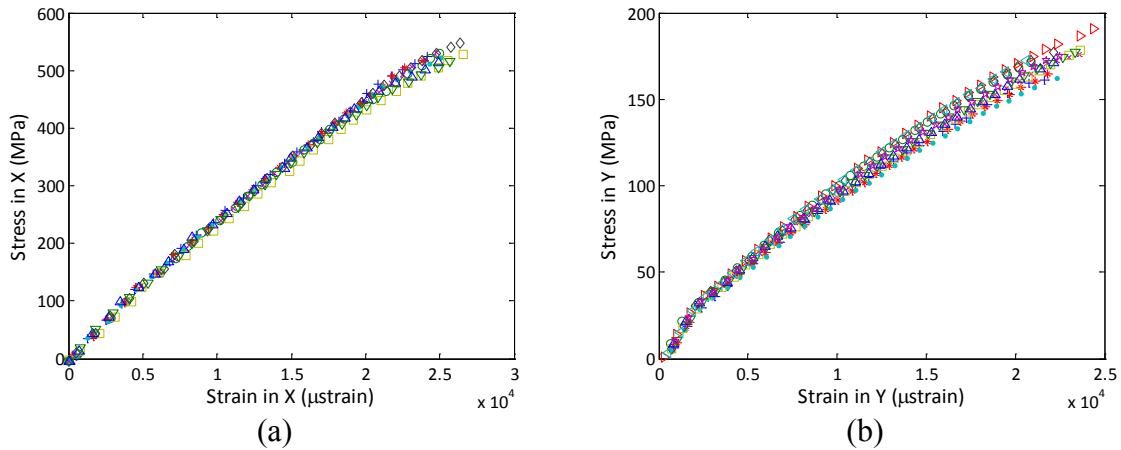
Figure 2.4 Longitudinal (a) and Hoop (b) Tension Stress-Strain Curves

The reciprocity condition for the elastic properties obtained from the tensions tests was checked using Equation 2.1. It was found that there was a difference of 32.5% between the left and right hand of the relationship.

$$\frac{\nu_{xy}}{E_x} = \frac{\nu_{yx}}{E_y}$$

Equation 2.1

This indicates that the material does not behave linear-elastically. Hoop tension tests show a bilinear trend, which is a likely cause of this difference. The difference in

8

strain ranges used in calculating properties for longitudinal and hoop tests may also

induce error. The bilinear trend in hoop tension tests can be seen in Figure 2.5.

(a)   (b)
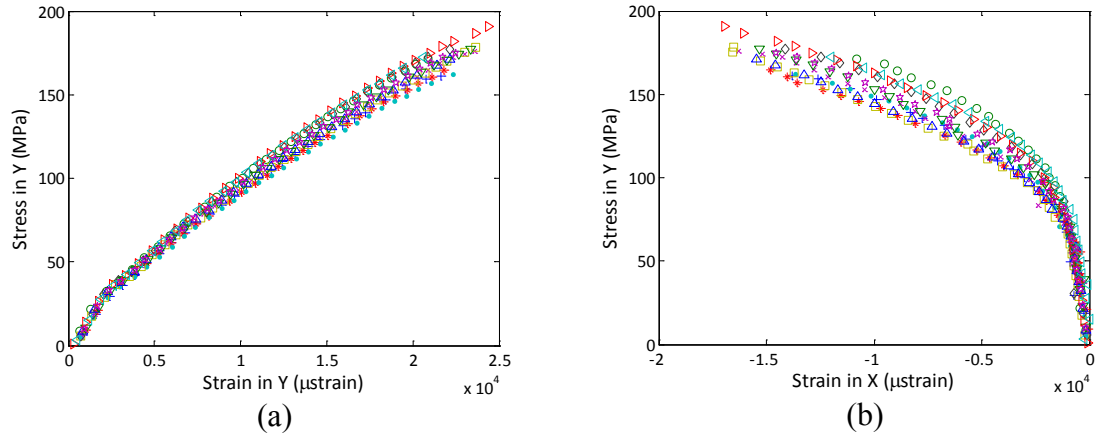
Figure 2.5 Strain Parallel (a) and Perpendicular (b) to Loading in Hoop Tension

Typical failure modes of tension coupons were classified using ASTM D3039 [8].

Longitudinal tension samples were characterized as having an "explosive gage middle"

(XGM) failure, while hoop tension samples had an "angled gage middle" (AGM) failure.

The failure modes can be seen in Figure 2.6.

(a)

(b)

(c)
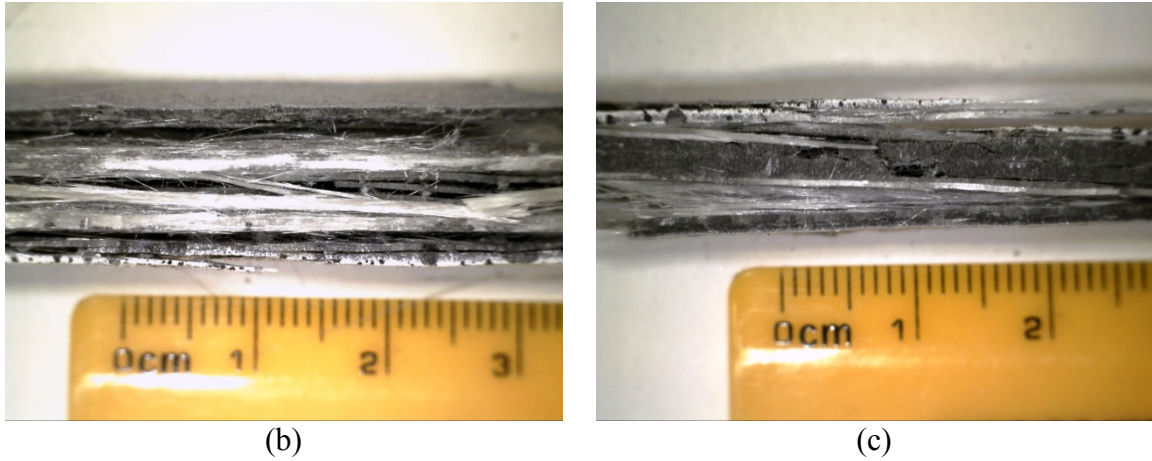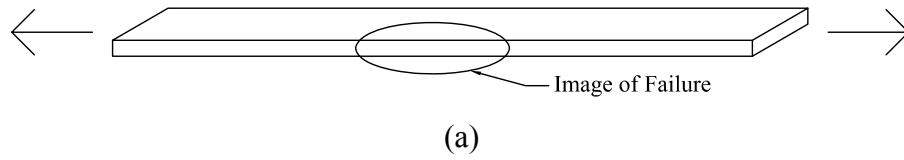
Figure 2.6 Image Location (a) of Failure in Longitudinal (b) and Hoop (c) Tension Samples

2.4 Compressive Properties

All compression testing was conducted in accordance with ASTM D6641 [9]. Twelve compression coupons were tested in the longitudinal orientation and another twelve coupons were tested in the hoop orientation.

The ASTM standard for this test suggests a bolt torque of 2.5 to 3.0 N-m (20 to 25 in-lbs). The bolt torque was increased to 5.6 N-m (50 in-lbs) to prevent samples from slipping in the test fixture. The test fixture can be seen in Figure 2.7.

Figure 2.7 Compression Test (ASTM D6641)

The results of longitudinal and hoop compression tests can be seen in Table 2.3.

Table 2.3 Compression Test Results

Test	Statistic	Ultimate Stress (MPa)	Ultimate Strain (µstrain)	Modulus (GPa)
Longitudinal Compression	Mean	497	2.17E+04	25.3 (E_x)
	Std. Dev.	35	2.90E+03	1.7
	COV	7.0%	13.4%	6.7%
Hoop Compression	Mean	235	1.65E+04	14.8 (E_y)
	Std. Dev.	13	1.51E+03	0.5
	COV	5.6%	9.1%	3.4%

Elastic modulus in the X and Y direction (E_x and E_y) and Poisson's ratio (v_{xy}) are adopted from the tension tests for design and calculation purposes.

Stress-strain plots of longitudinal and hoop compression tests can be seen in Figure 2.8.

(a)   (b)
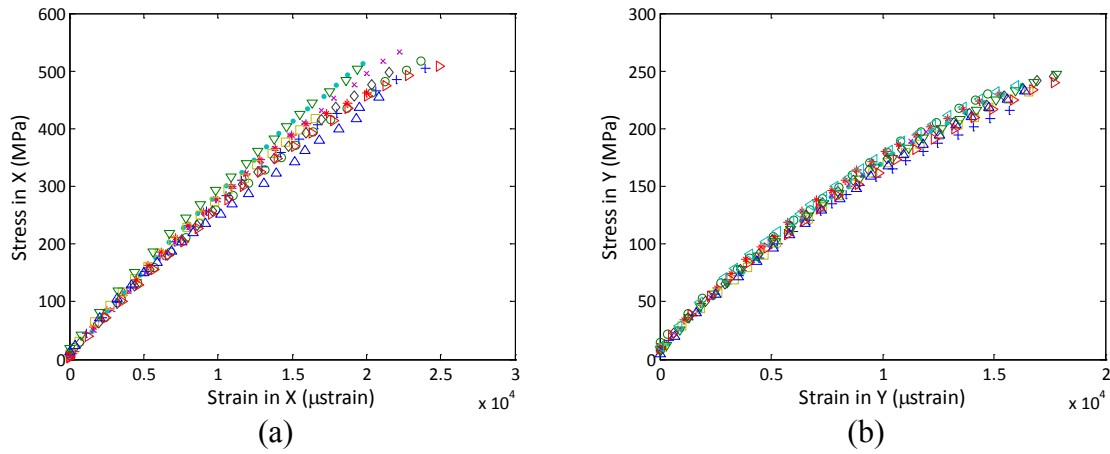
Figure 2.8 Longitudinal (a) and Hoop (b) Compression Stress-Strain Curves

Typical failure modes of compression coupons were classified using ASTM D6641[9]. Longitudinal and hoop compression samples were characterized as having a "brooming gage middle" (BGM) failure. The failure modes can be seen in Figure 2.9

(a)

(b)   (c)
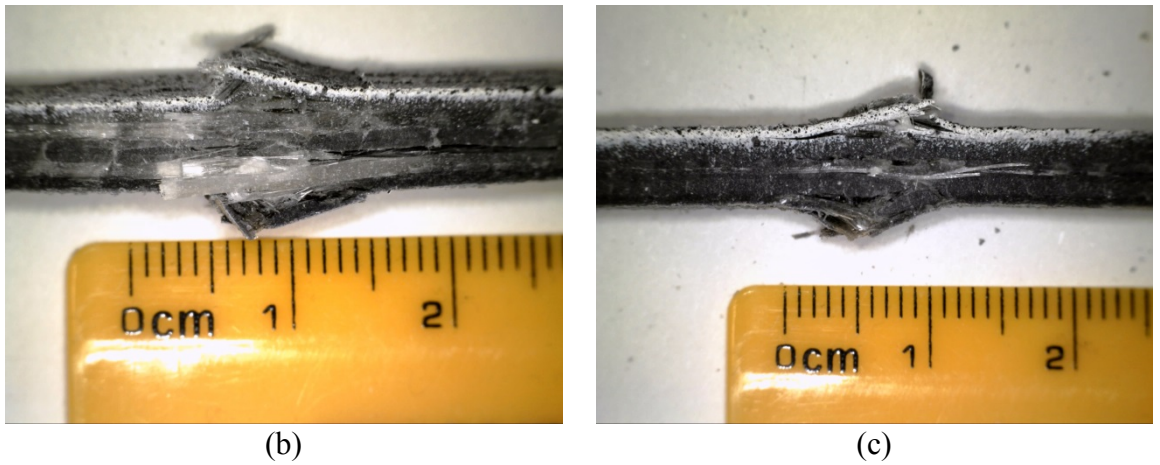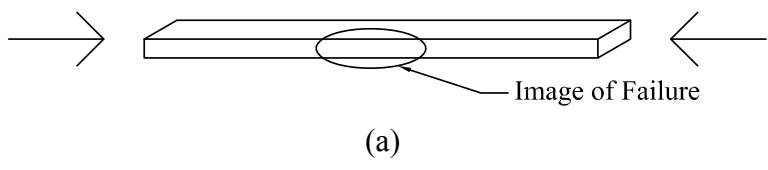
Figure 2.9 Image Location (a) of Failure in Longitudinal (b) and Hoop (c) Compression Samples

2.5 Shear Properties

All shear testing was conducted in accordance with ASTM D7078 [10]. Twelve shear coupons were tested in the longitudinal orientation and another twelve coupons were tested in the hoop orientation. The ASTM standard used for this test was designed for samples with reinforcing only in the 0 and 90 degree directions. This material has reinforcing in the 0, 90, and +/- 45 degree directions which gives the material a higher shear strength. The suggested bolt torque of 55 N-m (40 ft-lbs) allowed samples to slip in the test fixture before failure, so the bolt torque was increased to 75 N-m (55 ft-lbs). The test fixture can be seen in Figure 2.10.
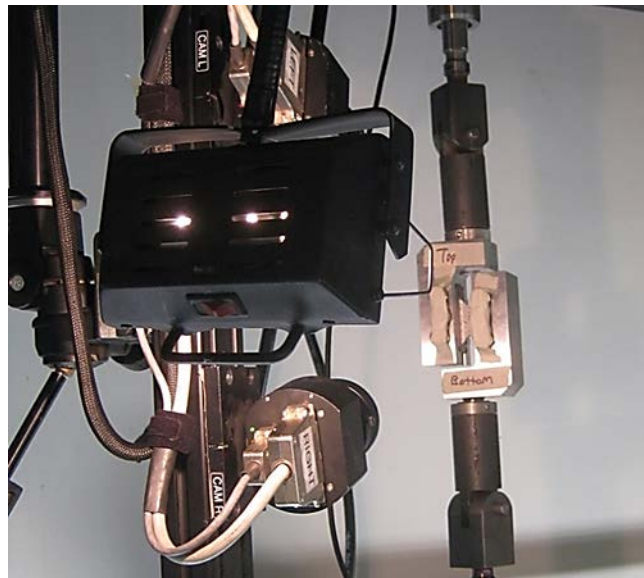
Figure 2.10 Shear Test (ASTM D7078) with ARAMIS System

The results of longitudinal and hoop shear tests can be seen in Table 2.4

Table 2.4 Shear Test Results

Test	Statistic	Ultimate Stress (MPa)	Ultimate Strain (μstrain)	Modulus (GPa)
Longitudinal Loading	Mean	168	3.63E+04	6.2 (Gxy)
	Std. Dev.	9	3.86E+03	0.2
	COV	5.6%	10.6%	2.6%
Hoop Loading	Mean	154	2.88E+04	5.9 (Gyx)
	Std. Dev.	15	4.23E+03	0.3
	COV	9.6%	14.7%	5.7%

Stress-strain plots of longitudinal and hoop shear tests can be seen in Figure 2.11.

(a)   (b)
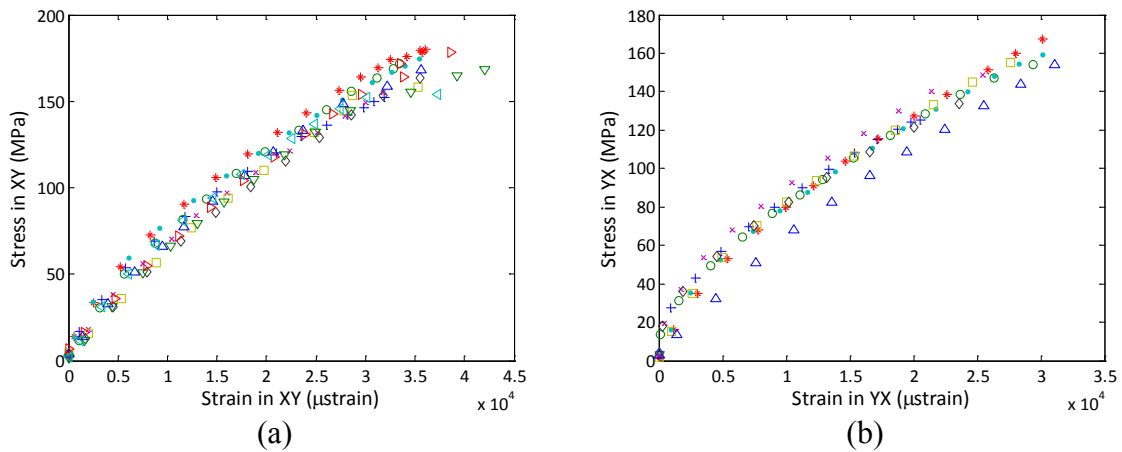
Figure 2.11 Longitudinal (a) and Hoop (b) Shear Stress-Strain Curves

Typical failure modes of shear coupons were classified using ASTM D7078 [10]. Longitudinal and hoop shear samples were characterized as having an "angled gage section between notches" (AGN) failure on one face and a "vertical cracking gage section between notches" (VGN) failure on the other face. The failure modes can be seen in Figure 2.12.

<center>(a)   (b)</center>
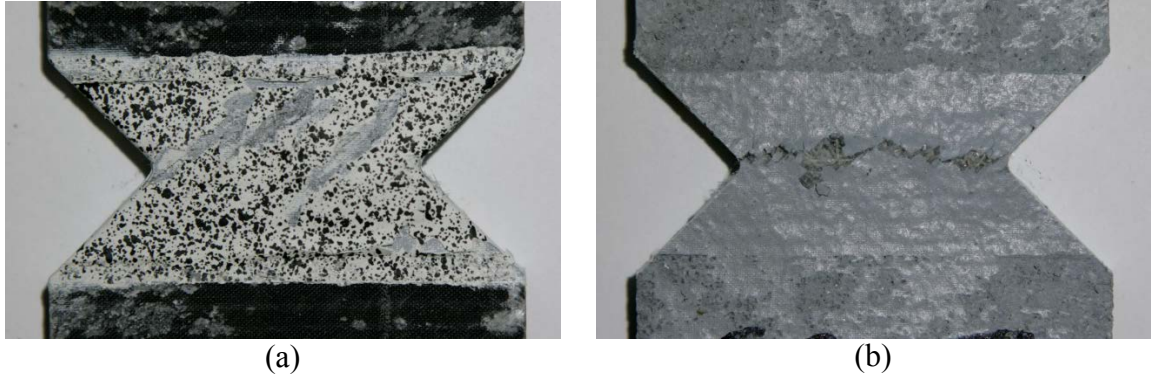
<center>Figure 2.12 Typical AGN Failure (a) and VGN Failure (b) of Shear Samples</center>

2.6 Glass Transition Temperature

Glass transition testing was conducted in accordance with ASTM E1640 [11]. A Thermal Analysis Instruments DMA Q800 dynamic mechanical analyzer was used to test samples. The 3 point bend test configuration was used to accommodate the thickness and modulus of the samples. The test set up can be seen in Figure 2.13.

<center>Figure 2.13 Glass Transition Temperature Test (ASTM E1640)</center>

Tests were conducted with a pre-load of 2 N, frequency of 1 Hz, temperature ramp of 3 °C per minute, and amplitude of 10 micrometers. The temperature range was 30 to 140 °C.

Dynamic mechanical analysis determines glass transition temperature (Tg) using 3 properties. Thermal Analysis Instruments [12] describes the 3 different glass transition temperatures as:

- "Onset of the change in slope of storage modulus: Occurs at the lowest temperature and relates to mechanical failure

- Peak of the loss modulus: Occurs at the middle temperature and is more closely related to the physical property changes attributed to the glass transition in plastics. It reflects molecular processes and agrees with the idea of Tg as the temperature at the onset of segmental motion

- Tan Delta Peak: Occurs at the highest temperature and is used historically in literature. It is a good measure of the 'leather like' midpoint between the glassy and rubbery states of a polymer. The height and shape of the tan delta peak change systematically with amorphous content"

For the purpose of this research, the onset of the change in slope of the storage modulus will be used as the glass transition temperature in accordance with ASTM E1640 [11], but the peak of the loss modulus and tan delta curve will be presented for comparison. A plot of glass transition temperature test results can be seen in Figure 2.14.
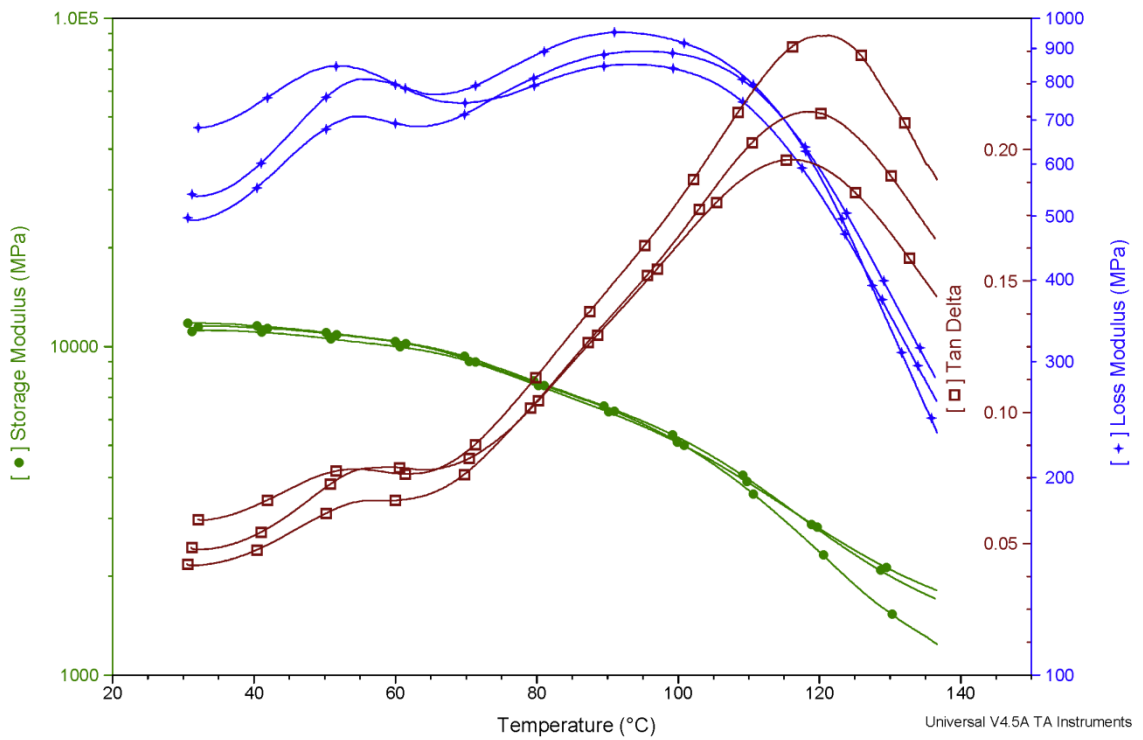
Figure 2.14 Glass Transition Temperature Results

A summary of the glass transition temperatures for each sample can be seen below in Table 2.5.

Table 2.5 Individual Glass Transition Temperature Results

Sample	Onset Point of Change in Slope of Storage Modulus (°C)	Peak of Loss Modulus (°C)	Peak of Tan Delta (°C)
Tg-1	89.0	91.4	121.2
Tg-2	86.3	95.0	118.2
Tg-3	84.2	93.2	116.2
Average	86.8	93.2	118.5

2.7 Discussion of Mechanical Properties

The following ratios of material properties were calculated to examine orthotropic material behavior. Ratios of longitudinal tension (TL) to longitudinal compression (CL) and hoop tension (TH) to hoop compression (CH) are expected to be 1 for an orthotropic material. The ratio of longitudinal to hoop ultimate strength (σ_u) and modulus of elasticity (E) for tension or compression tests are also expected to be equal. These ratios are presented in Table 2.6 and are believed to be within the range of an orthotropic material.

Table 2.6 Ratios of Mechanical Properties

Properties	Values of Properties	Ratio
$\dfrac{\sigma_{u,TL}}{\sigma_{u,CL}}$	$\dfrac{530 MPa}{497 MPa}$	1.07
$\dfrac{\sigma_{u,TH}}{\sigma_{u,CH}}$	$\dfrac{174 MPa}{235 MPa}$	0.74
$\dfrac{\sigma_{u,TL}}{\sigma_{u,TH}}$	$\dfrac{530 MPa}{174 MPa}$	3.05
$\dfrac{\sigma_{u,CL}}{\sigma_{u,CH}}$	$\dfrac{497 MPa}{235 MPa}$	2.11
$\dfrac{E_{TL}}{E_{CL}}$	$\dfrac{22.5 GPa}{25.3 GPa}$	0.89
$\dfrac{E_{TH}}{E_{CH}}$	$\dfrac{13.7 GPa}{14.8 GPa}$	0.93
$\dfrac{E_{TL}}{E_{TH}}$	$\dfrac{22.5 GPa}{13.7 GPa}$	1.64
$\dfrac{E_{CL}}{E_{CH}}$	$\dfrac{25.3 GPa}{14.8 GPa}$	1.71

Typical stress-strain curves of tension and compression samples are presented in Figure 2.15 to graphically present similarities and differences between longitudinal and hoop properties.
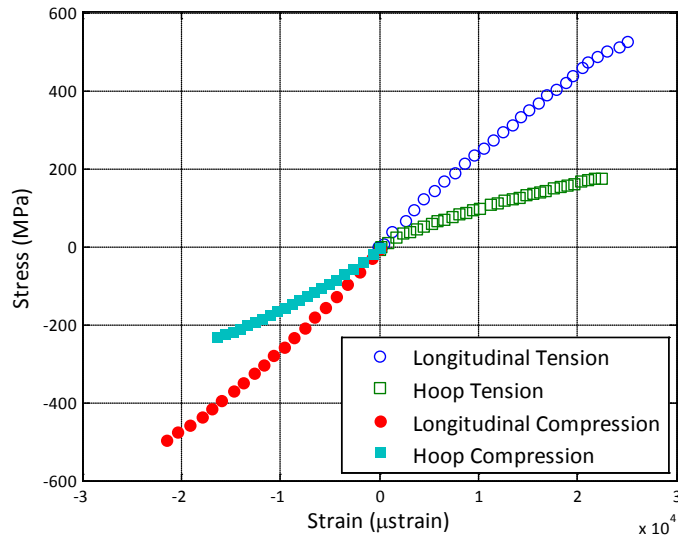
Figure 2.15 Typical Stress-Strain Curves of Tension and Compression Samples

Mechanical properties listed in Table 2.7 were used as inputs for predictive models.

Table 2.7 Summary of Mechanical Properties of FRP Plates

Test	Orientation of Properties	Ultimate Strength (MPa)	Ultimate Strain (μstrain)	Modulus (GPa)	Poisson's Ratio
Longitudinal Tension	X	530	2.56E+04	22.5	0.31 (ν_{xy})
Hoop Tension	Y	174	2.27E+04	13.7	—
Longitudinal Compression	X	497	-2.17E+04	25.3	—
Hoop Compression	Y	235	-1.65E+04	14.8	—
In-Plane Shear	XY	154	2.88E+04	5.9	—

CHAPTER 3 GEOTECHNICAL PROPERTIES OF FRP PLATES

3.1 Literature Review

Piles transfer load to the soil through skin friction along the shaft of the pile (both outside and inside for an open ended pipe pile) and end bearing at the toe. The skin friction of piles in granular soil is related to the horizontal soil pressure on the pile and the interface friction angle. The interface friction angle is dependent on many factors, including the soil properties and pile material. The total capacity of a pile is the sum of the skin friction and bearing capacity [13].

As a pile resists loads, shear stresses are induced along the shaft of the pile. During shear of loose and dense granular soils, at strains of approximately 10% or greater, the soil enters a critical state where there is no more change in volume during shear. Dense soils will reach a peak shear stress before reaching the critical state, while loose soils will reach the critical state without encountering a peak shear stress [14]. For the purpose of this research, the friction angle and interface friction angle at the peak shear stress will be denoted as φ_p and δ_p respectively. The friction angle and interface friction angle at the critical state will be denoted as φ_{cv} and δ_{cv} respectively, with "cv" representing "constant volume".

During shear, particles are rearranged as they move past each other. This creates a change in volume of the sample. In a direct shear test, the soil sample will change in height because all other dimensions are assumed to be fixed. Dense soils will dilate to

allow soil grains to pass each other, while the soil grains of a loose soil will slide into the voids of the soil and the soil will compress [14].

Pando et al [15] conducted interface friction testing of soil on two fiber reinforced polymer (FRP) pile materials manufactured by Lancaster Composites Inc. and Hardcore Composites Inc. and a prestressed concrete pile. The surface of the FRP materials were characterized with hardness and surface profile tests. These materials were then tested in direct shear with two sands; Density Sand and Model Sand. This study found that the surface profile of the FRP material affects the interface friction angle. Surfaces with larger relative height (ratio of the maximum peak to valley height of the material surface topography to the soil grain size at which 50% of the sample is finer) and smaller relative spacing (ratio of the distance between peaks of the material surface topography to the soil grain size at which 50% of the sample is finer) typically give larger interface friction values. It was also found that the hardness of the FRP material and angularity of the soil grains affected the interface friction angle. Softer FRP surfaces and more angular soil grains produced higher interface friction angles, because particles are able to penetrate the FRP surface.

Pando et al [2] expanded their previous research [15] to include a comparison of flat plates with and without a roughened surface treatment manufactured by Hardcore Composites Inc. The surface treatment improved the interface friction angle with both soils. The pile with the roughened surface treatment had an increase in peak interface friction angle of 3.5 degrees and 5.6 degrees for the Density Sand and Model Sand, respectively. This study also included the addition of a steel pile and reinforced plastic pile.

21

Sakr et al [16] used interface shear tests and pile pullout tests on model piles to characterize the frictional behavior between a dry, dense sand and pile surfaces (FRP and steel). This study also found that relative roughness of the FRP material has a significant effect on the interface shear behavior of FRP piles. The FRP material had a higher friction angle than the steel samples, resulting in higher frictional resistance. Interface friction angles were used to predict uplift capacity of model piles. Ratios of predicted uplift capacity to measured uplift capacity ranged from 0.92 to 1.14. This study concluded that the interface friction test is a reasonable and inexpensive method to predict the frictional resistance of FRP piles.

Frost and Han [17] tested the interface shear behavior of FRP and steel samples using 4 different soils to examine the effects of mean grain size, interface surface roughness, initial density of sand, normal stress, angularity of sand, specimen preparation method, rate of shearing, and thickness of sand specimen. The FRP and steel in this study behaved similarly for the different soil types. It was found that relative roughness, normal stress, initial density, and angularity of particles all affected the interface friction angle, while specimen preparation method, rate of shearing, and thickness of soil made little difference in the interface friction angle.

Reddy et al [18] examined the use of modified direct shear tests for determining interface friction angle. Interface friction testing was conducted on mild steel and aluminum alloy with two sands and compared to soil-pile-slip tests for aluminum alloy pile elements ranging from 12.7 to 38.1 mm (0.5 to 1.5 in) in diameter. Test results showed that the interface friction angle was larger in soil-pile-slip tests which is likely due to interface slip dilation seen in small piles. Test results were extrapolated to

determine that the interface friction angle found using a modified direct shear test were appropriate for a pile 1.7 m (5.6 ft) in diameter. However, the effects of pile installation were not taken into account for the soil-pile-slip tests and may be significant for large diameter piles. Reddy et al concluded that peak interface friction values from direct shear tests are conservative.

3.2 Soil Types

Three soils were used to determine the interface friction angle of the FRP material: Ottawa sand, Maine Department of Transportation (MaineDOT) Backfill, and a glacial till. Prior to all testing, grains above the number 8 sieve were removed to meet the requirements of ASTM D3080[19] for the minimum sample height to maximum grain size ratio in interface friction tests. The grain size distributions for these soils can be seen in Figure 3.1.
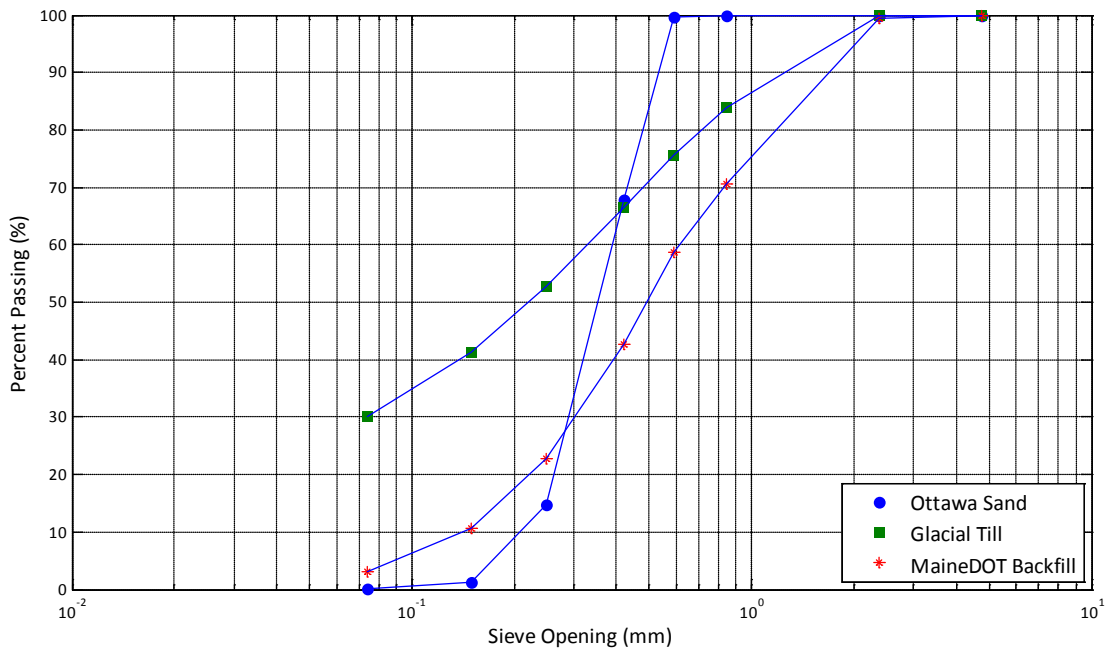
Figure 3.1 Grain Size Distribution of Selected Soils

23

3.2.1 Ottawa Sand

Ottawa sand was selected because it is a well-documented soil. Ottawa sand is sub-rounded with small range of grain sizes. The Ottawa sand can be seen in Figure 3.2.

Figure 3.2 Ottawa Sand

3.2.2 MaineDOT Backfill

This soil was selected because it is an engineered granular fill meeting the requirements for MaineDOT Type B Aggregate [20]. It is a sub-angular soil with little fines content. The MaineDOT Backfill can be seen in Figure 3.3.

Figure 3.3 MaineDOT Backfill

3.2.3 Glacial Till

A glacial till was selected because it is a soil that is commonly encountered in Maine and can produce difficult driving conditions. The till used in this testing was obtained from an open excavation at the corner of Long Road and Rangeley Road in Orono, ME. This soil is angular to sub-angular with high fines content. The glacial till can be seen in Figure 3.4.

Figure 3.4 Glacial Till

3.3 Characterization of Soil Properties

A series of index tests were performed on the soils to characterize their properties. These tests include:

- Grain Size Analysis (ASTM D6913 [21])

- Specific Gravity (ASTM D854 [22])

- Maximum Density (ASTM D4523 [23] and ASTM D1557 [24])

- Minimum Density (ASTM D4254 [25])

- Atterberg Limits (ASTM D4318 [26])

- Direct Shear (ASTM D3080 [19])

A summary of the soil properties can be seen in Table 3.1.

Table 3.1 Summary of Soil Properties for Interface Friction Testing

Soil	D10 (mm)	D30 (mm)	D60 (mm)	Plasticity Index	Min Void Ratio	Max Void Ratio	Specific Gravity
Ottawa Sand	0.203	0.279	0.406	NP	0.45[a]	0.71	2.65
MaineDOT Backfill	0.145	0.305	0.584	NP	0.39[a]	0.72	2.72
Glacial Till	0.025[c]	0.076	0.330	3	0.34[b]	0.98	2.70

[a] Determined using vibratory table [23]
[b] Determined using modified Proctor test [24]
[c] Grain size distributions were not determined using a hydrometer. D10 for the glacial till is a best estimate.

3.4 Friction Properties of Soil-FRP Interface

Interface friction tests were conducted by removing the bottom half of the direct shear box and replacing it with a flat FRP plate. The difference between direct shear and interface friction test fixtures can be seen in Figure 3.5.
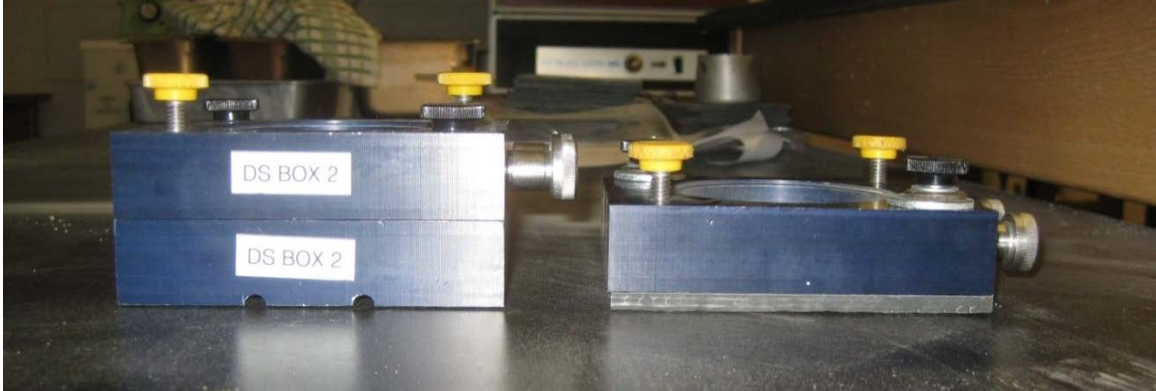
Figure 3.5 Direct Shear (Left) and Interface Friction (Right) Test Fixtures

Interface friction tests were also conducted at target relative densities of 50-55% and 70-75% prior to consolidation using pressures of 47.9, 95.8, and 239 kPa (1000, 2000, and 5000 psf). Tests were run using a constant vertical pressure and rate of horizontal displacement. The test frame used for direct shear and interface friction can be seen in Figure 3.6.
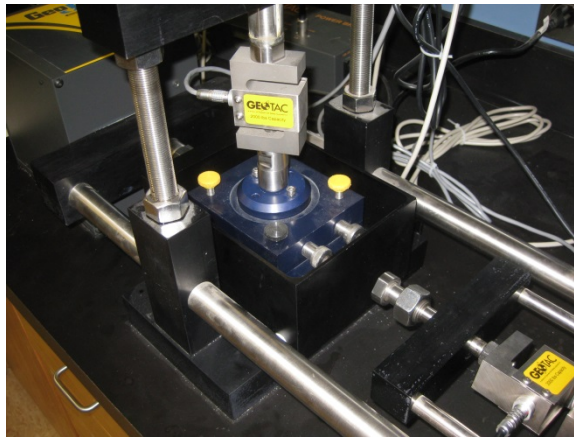
Figure 3.6 Direct Shear and Interface Friction Test Frame

FRP plates were not perfectly flat, which allowed soil grains to escape during compaction and consolidation. This led to errors in relative density calculations. A constant compactive effort was used to prepare samples as closely as possible to the

relative densities used in direct shear tests. Resulting angles of internal friction and interface friction can be seen in Table 3.2.

Table 3.2 Direct Shear and Interface Friction Test Results

Sample		Direct Shear		Interface Friction	
Soil	Density	Peak, φ_p (Degrees)	Constant Volume, φ_{cv} (Degrees)	Peak, δ_p (Degrees)	Constant Volume, δ_{cv} (Degrees)
Ottawa Sand	Med. Dense	36.4	31.5	28.2	26.3
	Dense	39.1	34.5	32.6	27.3
MaineDOT Backfill	Med. Dense	40.9	39.1	28.4	28.2
	Dense	42.1	35.3	31.8	28.9
Glacial Till	Med. Dense	39.4	38.4	31.6	30.9
	Dense	40.7	38.7	32.3	32.1

3.5 Discussion of Interface Friction Values

FRP plates used for the testing had a slight curvature. This curvature was not able to be removed prior to testing because the plates were manufactured using a thermoset resin. This curvature will depress under the normal stress applied during the test. This is illustrated in Figure 3.7. The test fixture was calibrated to account for the additional change in vertical height caused by the depression of the FRP plates.
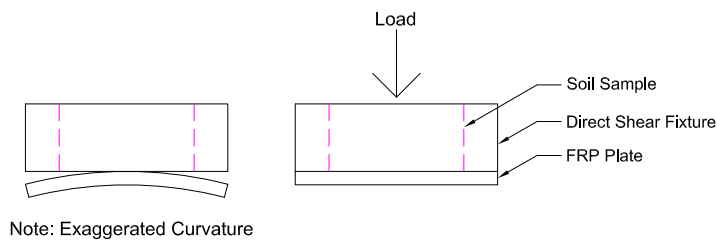
Figure 3.7 Flattening of FRP Plate under Load

Interface friction testing conducted on this FRP material showed dilatancy during shear. This is contrary to the behavior observed by Frost and Han [17] and Sakr et al [16],

who did not note any dilation. Work by O'Rourke et al [27] suggests that soil particles predominately slide across hard, smooth materials, creating little or no dilatant behavior. An example of dilatancy seen in interface friction testing of medium dense MaineDOT backfill can be seen in Figure 3.8.
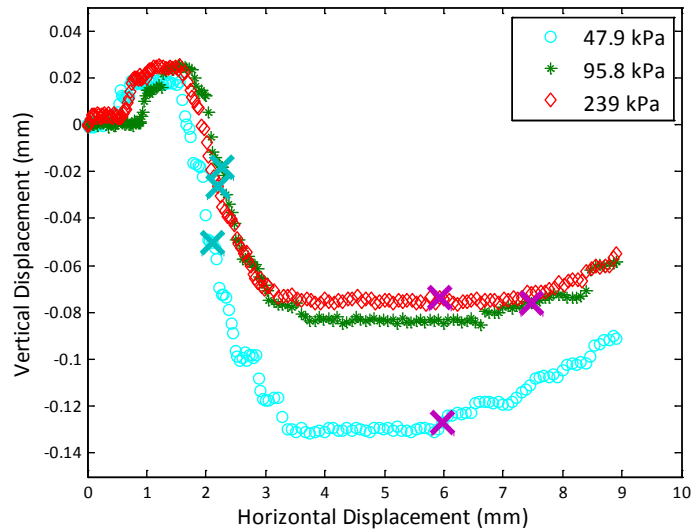
Figure 3.8 Dilatancy of Medium Dense MaineDOT Backfill during Interface Friction Testing

Upon further investigation, FRP plates showed striations and gouges that indicate soil grains may have become embedded in the FRP material. This would force soil grains to move over and around each other during shear, instead of sliding across the surface of the FRP. This embedment of soil grains would create interlocking of soil particles and increase the interface friction angle. Striations and gouges on the FRP material can be seen in Figure 3.9.

<center>(a)   (b)</center>
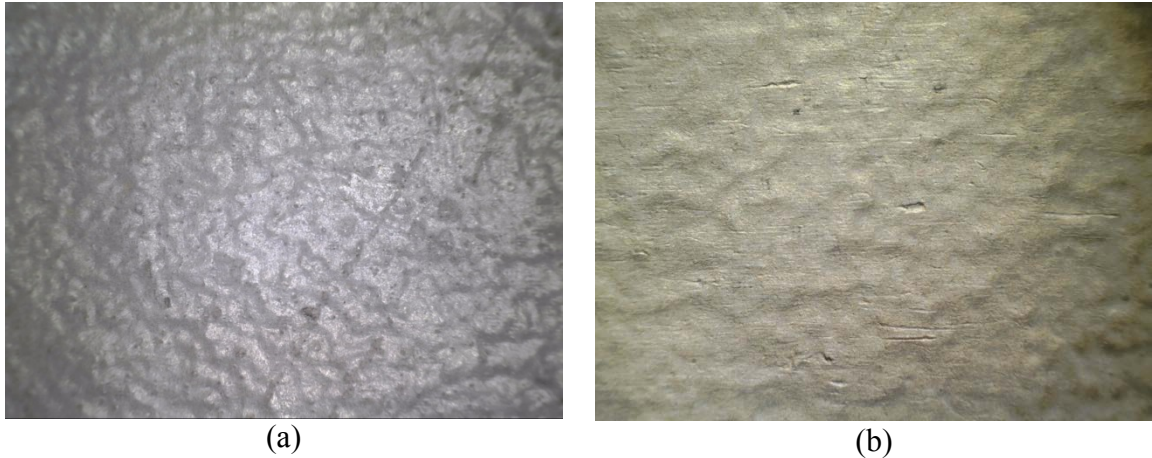
<center>Figure 3.9 Untested FRP Plate (a) and FRP Plate Used in Interface Friction Testing with Scrapes and Gouges (b)</center>

The Barcol Hardness of the material used in this study, as published by the resin manufacturer [6], is 47 for a neat resin casting and 48 for a laminate sample. This is similar to the manufacturer published Barcol Hardness of Composite Pile Type CP-A tested by Pando et al [15]. The density sand used by Pando et al appears to have similar properties to the Ottawa Sand used in this study, but interface friction values are significantly higher for the Harbor Technologies, LLC.'s FRP material and Ottawa Sand. This study does not have s surface profile of the FRP material or Vickers Hardness values to compare with the results of Pando et al [15],[2]. It should be noted that these properties have been found to play a significant role in the interface friction behavior of FRP materials and granular soils.

Interface friction values from this research compare well with similar test results published in literature for FRP pile materials. Pando et al [2] found peak interface friction values ranging from 19.7 to 37.3 degrees, with all but two pile-soil combinations falling between 27.3 and 33.4 degrees. Peak interface friction values determined by Sakr et al [16] were 27.6 and 32.3 degrees. It should be noted that the testing published by others

<center>30</center>

covered a wide range of FRP materials and different soil types. This study found peak

interface friction values to range from 28.2 to 32.6 degrees.

Piles that were driven at Richmond and Dresden had a roughened outer coating

which was not present on the FRP plates used for interface friction testing. If the trends

found in the study by Pando et al [2] hold true for this FRP material, the interface friction

angle may increase by several degrees on the driven piles. Interface friction angles found

using the uncoated FRP material will produce conservative pile capacities when used in

calculations.

CHAPTER 4 FIELD INSTALLATION OF FRP PILES

4.1 Literature Review

4.1.1 Hollow Piles

Mirmiran et al [28] conducted testing where a hollow fiber reinforced polymer (FRP) pile with a 450 mm (17.7 in) long conical tip was driven using a diesel hammer with rated energy of 15.6-37.0 kN-m (11.5 to 27.3 kip-ft) and a pile cap with a neoprene pad. The pile was 7.9 m (25.9 ft) long with an outer diameter of 348 mm (13.7 in) and wall thickness of 14 mm (0.55 in). This pile was noted to "bow like a string" during easy driving. Once the pile reached a layer of sand, the top of the pile began to fail at a maximum compressive stress of 80 MPa (11.6 ksi).

Sakr et al [29] drove filament wound FRP piles using a model pile hammer with an energy of 1.2 kN-m (885 ft-lbs) and a 51 mm (2 in) thick plywood cushion. The piles used in the study were 1.52 m (5 ft) long with an outer diameter of 162.4 mm (6.4 in) and wall thickness of 5 mm (0.20 in). Piles were driven into dense Fanshawe brick sand in a laboratory setting. The maximum driving force was found to be 282 kN (63.4 kip), which is an equivalent stress of 114 MPa (16.5 ksi) when converted using the given pile dimensions. None of the piles in this study exhibited damage.

The same study by Sakr et al [29] also examined the use of a toe driving method where a mandrel with a conical tip was inserted into the hollow piles. The hammer strikes this mandrel which delivers the driving energy to the soil at the pile toe and drags the FRP shell behind it. Stresses are transferred to the FRP shell using a system of springs. At

the end of driving, this mandrel is removed from the pile and can be reused. This method created a maximum driving force of 125 kN (28.1 kips) in tension, which is an equivalent stress of 50.6 MPa (7.3 ksi). Toe driving also did not cause damage to the piles.

Iyer [30] drove hollow FRP piles using a steel pipe mandrel contacting a flat steel driving shoe nested inside the FRP shell. Piles were driven through uniform soil profile in Rapid City, SD. A 300 mm (11.8 in) diameter filament wound FRP pile achieved a capacity of 1935 kN (435 kips) without any visible damage. The maximum reported driving stress was 107 MPa (15.5 ksi), but it was unclear from the report whether this was a compressive or tensile stress.

Guades and Aravinthan [31] examined the effect of varying impact energy and number of impacts on the damage to FRP tubes. This study looked at pultruded tubes that measured 100 mm (3.9 in) square and energies up to 742 N-m (547 ft-lbs). It was found that the strength of the tubes was reduced by a maximum of 6.8%, 0.3%, and 10% in compression, tension, and flexure, respectively.

4.1.2 Concrete-Filled Piles

Baxter et al [32] drove a concrete-filled FRP pile using a hydraulic hammer with rated energy of 71.9 kN-m (53.0 kip-ft). The pile cushion broke as the blow count approached 4 blows per 25 mm (1 in), and the concrete and FRP were damaged. Pile Dynamic Analyzer (PDA) data was not able to be collected for this pile due to detaching of the sensors, so the driving stress at failure is unknown.

Pando et al [2] conducted a study with a reinforced, concrete-filled FRP pile driven in Hampton, VA for a bridge on Route 351. This pile was filled with non-shrink,

self-compacting concrete and reinforced with 14 No. 25M (No. 8) steel bars running down the longitudinal axis of the pile and No. 10M (No. 3) gage wire with a 150 mm (5.9 in) pitch. The pile was driven with a single-acting diesel hammer with a rated energy of 108.6 kN-m (80.1 kip-ft) and a 230 mm (9.1 in) thick plywood cushion. The soil profile at the driving site is composed of "silty fine sand, approximately 1.0 m (3.3 ft) thick. The fill is underlain by loose to medium dense silty fine sand to a depth of 13.0 m (42.7 ft). The silty fine sand is underlain by stiff sandy clay to a depth of 15.5 m (50.9 ft). Beneath the clay, medium dense to dense silty and clayey sand was encountered to the bottom of the borings at a depth of 30.6 m (100.4 ft)." The pile was driven to a Case Method capacity 1960 kN (440 kip) with a maximum stress of 16.2 MPa (2.3 ksi) and 8.5 MPa (1.2 ksi) in compression and tension, respectively. Pre and post driving Pile Integrity Testing (PIT) showed no significant changes. Axial and lateral load tests were also conducted on this pile.

Pando et al [2] also drove unreinforced, concrete-filled FRP piles for a bridge on Route 40 in Virginia. The FRP shells were manufactured using filament winding, filled with expansive concrete, and driven using a hydraulic hammer with a rated energy of 85.4 kN-m (63.0 kip-ft) and 190 mm (7.5 in) thick plywood cushion. The subsurface at the driving site consisted of "7.9 m (25.9 ft) of loose to medium-dense silty sand with some gravel, underlain by very stiff to hard silty clay". Driving was stopped when the blow count was 6 blows per 25 mm (1 in), corresponding to a capacity of 3140 kN (706 kip) (56% skin friction and 44% end bearing) using TNOWAVE [33] signal matching software. Maximum driving stresses were found to be 19.2 MPa (2.8 ksi) in compression

and 2.9 MPa (0.4 ksi) in tension. No damage due to driving was reported for these piles. This study also included axial and lateral load testing.

Mirmiran et al [28] drove a concrete-filled FRP pile with the same equipment and dimensions discussed in 4.1.1. The pile was filled with concrete having a strength of 34.5 MPa (5.0 ksi). This study noted that the pile "showed no visible sign of cracking or damage to the tube or concrete."

4.2 Pile Sample Description

FRP piles were manufactured by Harbor Technologies LLC in June 2013. All piles were 12.2 m (40 ft) long with an additional 127 mm (5 in) steel driving shoe and had an outside diameter of 610 mm (24 in). The piles driven for this research program are summarized in Table 4.1. Piles were either fully filled with concrete prior to driving (F), driven with a 1.22 m (4 foot) concrete plug at the toe (P), driven hollow (H), or driven hollow and then fully filled with concrete prior to being restruck (HF). After being extracted piles were tested in bending (B) or axial compression (A) to evaluate their residual properties.

Table 4.1 Summary of Driven Piles

Pile	Layers of Reinforcement	Type of Concrete	Type of Test	Pile Designation
Pile A	4	F	B,A	Pile A-4FB
Pile B	8	P	B	Pile B-8PB
Pile C	8	HF	B	Pile C-8HFB
Pile D	8	H	A	Pile D-8HA

All Piles were driven using a steel driving shoe designed by Harbor Technologies. Driving shoes for hollow and concrete-filled piles can be seen in Figure 4.1.

<div align="center">(a)   (b)</div>

Figure 4.1 Driving Shoe for Hollow (a) and Concrete-Filled (b) Piles

Maine Department of Transportation (MaineDOT) Class A concrete [20] with a target 28 day compressive strength of 30 MPa (4350 psi) was placed in the piles on August 14, 2013. This concrete contained no expansive or non-shrink additives. A 0.76 cubic meter (1 cubic yard) concrete bucket was used to fill the piles while they stood vertically in the template used for driving. The filling process and driving template can be seen in Figure 4.2. Concrete was allowed to free-fall and 0.91 m (3 ft) at the head of the pile was consolidated using a pencil vibrator.

(a)   (b)

Figure 4.2 Concrete Placement (a) and Driving Template (b) for FRP Piles

4.3 Site Characteristics

FRP piles were driven by Reed and Reed Inc. at a bridge connecting Richmond, ME and Dresden, ME over the Kennebec River (MaineDOT PIN 12674) on August 28, 2013. The driving site was located between Pier 5 and Pier 6 of the proposed bridge at approximate station 121+65. A restrike of Piles C and D was conducted on October 11, 2013. The configuration of the piles can be seen in Figure 4.3.
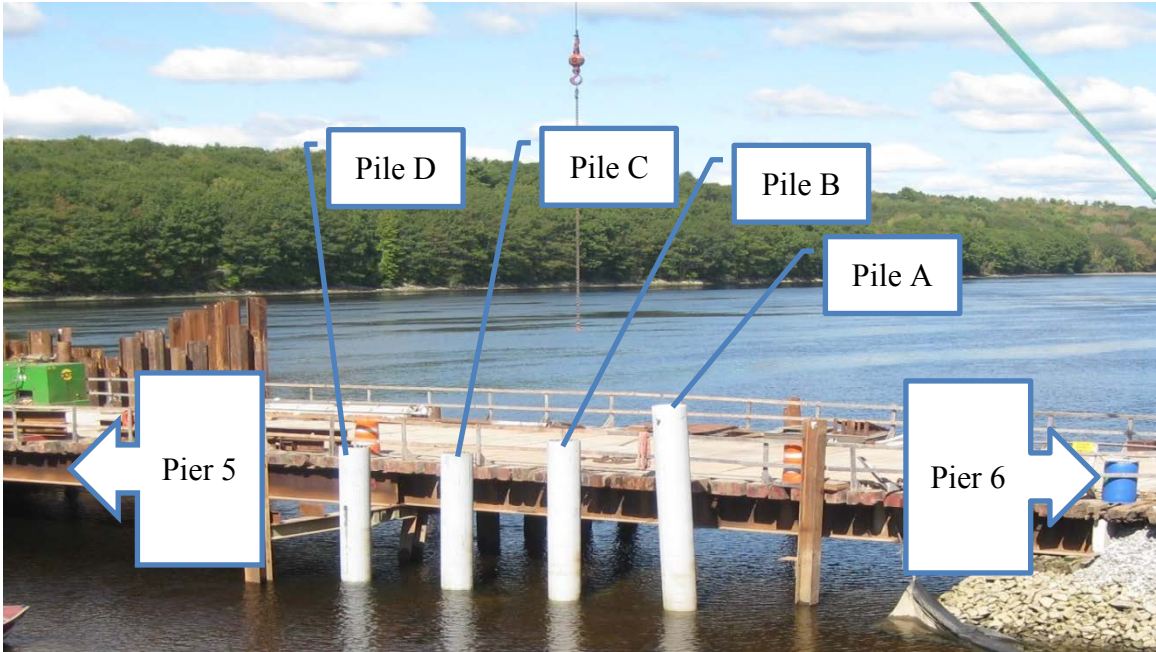
Figure 4.3 Configuration of Driven Piles (Looking Upstream)

Pier 5's soil conditions are characterized by glaciomarine silty clay overlain by alluvium and a depth to bedrock of approximately 4.57 m (15 ft). Pier 6's soil conditions are characterized by glacial till overlain by marine nearshore deposits and a depth to bedrock of approximately 6.10 m (20 ft). This can be seen in Figure 4.4 (courtesy of MaineDOT) [34, 35].
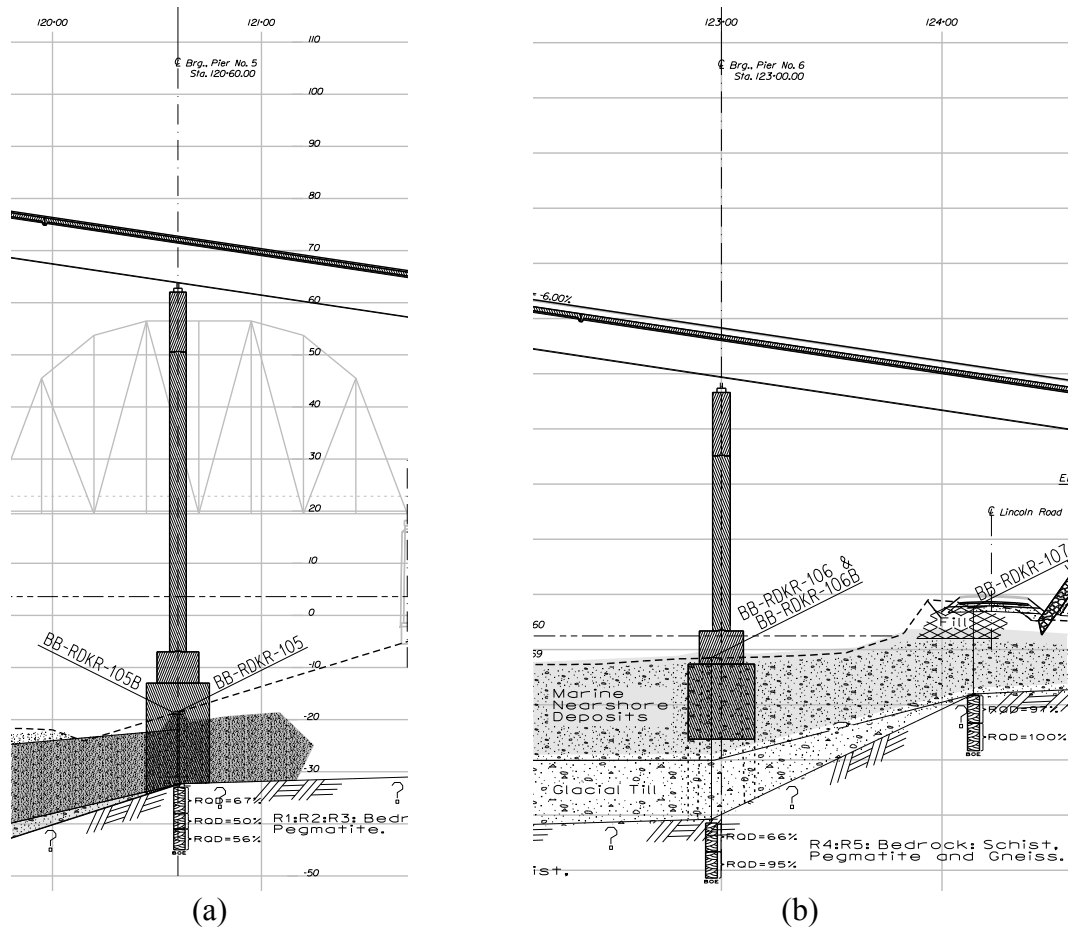
Figure 4.4 Soil Conditions at Pier 5 (a) and Pier 6 (b) of Proposed Bridge

Two supplementary borings were taken at the driving site on November 20, 2013. The logs show refusal at approximately 7.62 m (25 ft) with possible medium dense to very dense glacial till (about 5 ft thick) above refusal. This is overlain by soft clay and loose to medium fine sand deposits. This can be seen in Figure 4.5 [34, 36].
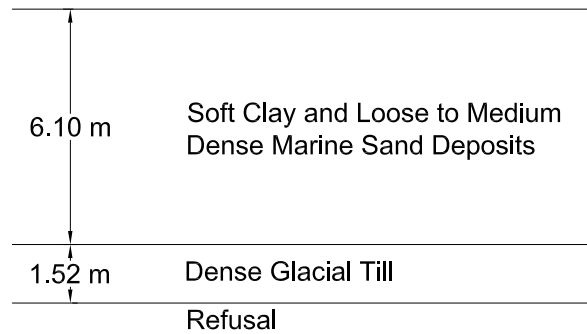
Figure 4.5 Subsurface Conditions from Supplementary Borings

4.4 Pile Driving Equipment

Driving was conducted using a Delmag D36-32 diesel hammer. This hammer has a maximum rated energy of 123 kN-m (90,560 ft-lbs), a 3600 kg (7,930 lb ram), and a variable fuel setting [37]. The target ultimate load for the piles was 2670 kN (600 kips). GZA GeoEnvironmental, Inc. (GZA) provided driving criteria, based on the use of fuel setting 2. This indicated that pile compressive stresses would be less than the specified maximum allowable stress of 82.7 MPA (12 ksi) set by Harbor Technologies LLC [34].

During initial driving, all piles were driven using a steel driving cap designed and manufactured by Reed and Reed Inc. Pile A, which was fully filled with concrete was driven with a 152 mm (6 in) thick plywood cushion between the steel driving cap and pile. All other piles were driven with the steel driving cap directly contacting the pile. The driving cap can be seen in Figure 4.6.

(a)	(b)

Figure 4.6 Driving Cap for Hollow (a) and Fully Concrete-Filled (b) Piles

During the restrike, a steel insert was added to the driving cap. Pile C was driven with a 76 mm (3 in) thick plywood cushion and Pile D was driven with a 25 mm (1 in) thick plywood cushion. This can be seen in Figure 4.7.

(a)	(b)

Figure 4.7 Steel Insert for Driving Cap (a) and Plywood Cushion (b) for Restrike

4.5 Results of Pile Driving

The capacities of the piles were calculated in the field using the Pile Dynamics, Inc. Case Method and then refined using a Case Pile Wave Analysis Program (CAPWAP) [38] with Pile Driving Analyzer (PDA) [39] data. Pile capacities after initial pile driving can be seen in Table 4.2 [34, 40]. Data for Pile A was not within the reportable range. Pile B was driven on fuel setting 3 for the last 51 mm (2 in).

Table 4.2 Pile Capacities after Initial Pile Driving

Pile ID	Field Capacity Capacity (kN)	Case Method Capacity (kN)	CAPWAP		
			Capacity (kN)	End Bearing (%)	Skin Friction (%)
Pile A	3780	No Data	———————— No Data ————————		
Pile B	2670	2360	2270	94	6
Pile C	2090	2310	2090	87	13
Pile D	2290	2270	1960	86	14

After initial pile driving, damaged sections at the head of the Piles C and D were removed, Pile C was cleaned out and completely filled with concrete, and Piles C and D were restruck. Pile capacities after the restrike can be seen in Table 4.3 [34, 41]. Data for Pile C was not within the reportable range. Pile D was driven on fuel setting 3 for the final 178 mm (7 in).

Table 4.3 Pile Capacities after Restrike

Pile ID	Field Capacity Capacity (kN)	Case Method Capacity (kN)	CAPWAP		
			Capacity (kN)	End Bearing (%)	Skin Friction (%)
Pile C	3340	No Data	———————— No Data ————————		
Pile D	2890	2050	1960	82	18

Some piles received excessive damage at the head and/or toe resulting in a reduction in length. The final configuration of the driven piles is illustrated in Figure 4.8. All elevations were determined using the elevation of the driving template and penetration data from the field driving logs. The driving template is assumed to be at a constant elevation of +1.98 m (+6.5 ft) for all piles. The mudline elevations were determined using visual references on extracted piles.
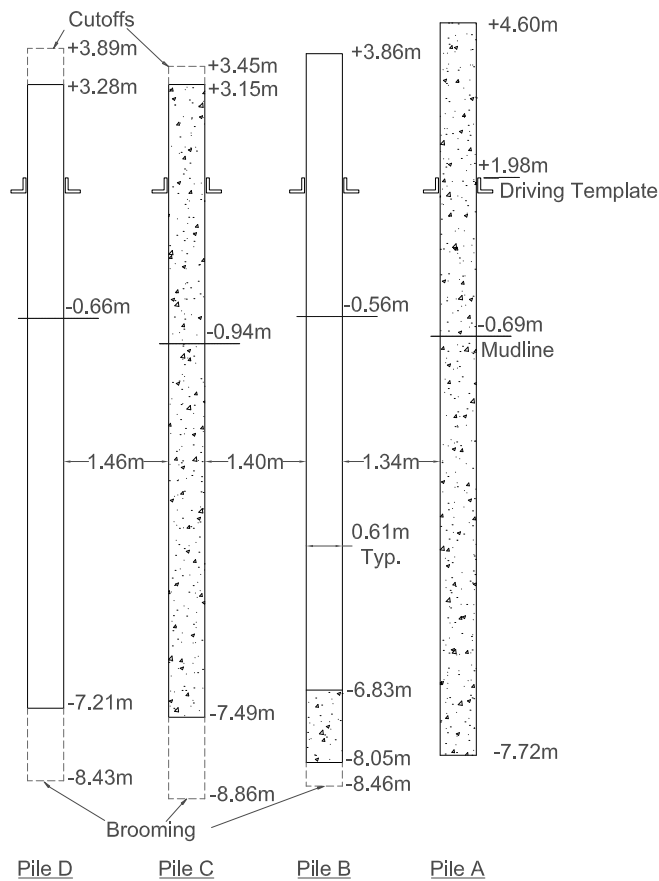
Figure 4.8 Pile Layout After Restrike

After pile driving, piles were extracted to document damage due to driving and evaluate residual properties. All piles showed various levels of damage, but all piles showed scrapes and gouges typical of those pictured in Figure 4.9. These scrapes and

43

gouges occurred above and below the mudline, and are therefore believed to have occurred during the extraction process, when a steel wedge was driven next to the piles to loosen the surrounding soil. These scrapes and gouges were present for all testing of residual properties but did not appear to affect the location of failure in flexural testing.

Figure 4.9 Typical Damage Due to Pile Driving/Extraction

4.5.1 Pile A

Pile A had 4 reinforcing layers, 12.7 mm (0.5 in) nominal wall thickness, and was filled with concrete prior to installation. No restrike was conducted on Pile A. After driving it was extracted and tested in bending.

Pile A was driven on fuel setting 3 and stroke of 1.52m (5 ft) to an elevation of -3.20 m (-10.5 ft). The pile was driven out of vertical alignment and driving was stopped to realign the pile. Pile A was then driven on fuel setting 2 to an elevation of -7.72 m (-25.33 ft). Stopping criteria for this pile was 8 blows per 25 mm (1 in) on fuel setting 2 with stroke of 1.89 m (6.2 ft). Driving was stopped at a final blow count of 4.5 blows per 25 mm (1 in). The reported capacity of Pile A in the field based on the Case Method was

3780 kN (850 kips) [34, 42]. The PDA showed possible damage/separation near the end of the pile. After analysis of the data, GZA found that the dynamic pile testing data was not within reportable limits [34, 40].

The condition of the head and toe of Pile A can be seen in Figure 4.10.

| (a) | (b) |

Figure 4.10 Head (a) and Toe (b) of Pile A after Initial Driving

4.5.2 Pile B

Pile B had 8 reinforcing layers, 25.4 mm (1 in) nominal wall thickness, and had a 1.22m (4 ft) concrete plug cast at its toe prior to installation. No restrike was conducted on Pile B. After driving it was extracted, the concrete plug was removed, and the pile was tested in bending.

Pile B was driven to an elevation of -8.46 m (-27.75 ft) on fuel setting 2 and stroke of 1.40 m (4.6 ft). Stopping criteria for this pile was 8 blows per 25 mm (1 in) at fuel setting 2 and stroke of 2.65 m (8.7 ft). Driving was stopped at 6.8 blows per 25 mm (1 in). Upon extraction, it was found that 0.40 m (1.3 ft) was lost due to a brooming

failure. The reported capacity of Pile B in the field based on the Case Method was 2670 kN (600 kips) [34, 42]. However, after further analysis GZA revised the Case Method capacity to 2360 kN (530 kips) and calculated a Case Pile Wave Analysis Program (CAPWAP) capacity of 2270 kN (510 kips) with 6% skin friction and 94% end bearing [34, 40].

The condition of the head and toe of Pile B can be seen in Figure 4.11.

(a)   (b)

Figure 4.11 Head (a) and Toe (b) of Pile B after Driving

The concrete plug was removed from Pile B prior to residual strength testing. The bottom portion of the plug was mainly sand and coarse aggregate. The same concrete used for this plug was also used to fill Pile A, but had very different visual properties. The upper 152 mm (6 in) resembled chalk and was lightweight and could easily be broken by hand. The removed concrete can be seen in Figure 4.12. It is believed that water infiltrated the piles, potentially through the driving shoe, during concrete placement and washed the cement from the concrete. The concrete was placed in the pile while its toe was in the water. By inspection, the concrete in the plug did not meet the specified

46

strength. The concrete from Pile B was also tested with a Schmidt Concrete Test Hammer. This equipment was not calibrated, but was verified against concrete with known design strengths in at the Advanced Structures and Composites Center at the University of Maine. The concrete did not register on the test hammer's scale, which has a minimum value of 10 MPa (1450 psi).

| (a) | (b) |

Figure 4.12 Concrete Plug of Pile B (a) and Removed Concrete (b)

When Pile A was cut for disposal, the concrete at the toe of the pile did not show any of the deterioration that was seen in Pile B. However, the strength of the concrete at the toe of Pile A was not tested to verify its strength.

4.5.3 Pile C

Pile C had 8 reinforcing layers, 25.4 mm (1 in) nominal wall thickness, and was initially driven hollow. This pile was cleaned out, completely filled with concrete, and restruck. After driving, it was extracted tested in bending.

4.5.3.1 Initial Driving

Pile C was driven to an elevation of -8.08 m (-26.5 ft). At this depth, the PDA
showed damage approximately 1.52 m (5 ft) from the end of the pile. Driving continued
to an elevation of -8.79 m (-28.83 ft) when the top of the pile failed. Stopping criteria for
this pile was 11 blows per 25 mm (1 in) at fuel setting 2 and stroke of 2.59 m (8.5 ft). At
failure, the blow count was 2 blows per 12 mm (1/2 in). The reported capacity of Pile C
in the field based on the Case Method was 2090 kN (470 kips) [34, 42]. After further
analysis, GZA revised the Case Method capacity to 2310 kN (520 kips) and calculated a
CAPWAP capacity of 2090 kN (470 kips) with 13% skin friction and 87% end bearing
[34, 40].

The condition of the head of Pile C after initial driving can be seen in Figure 4.13.

Figure 4.13 Head of Pile C after Initial Driving

4.5.3.2 Restrike

The damaged end of this pile was removed to the bottom of the lifting hole (approximately 0.30 m (1 foot)). Pile C was cleaned and filled with MaineDOT Class A concrete prior to the restrike. During the cleanout process, the contractor encountered an object approximately 1.52 m (5 ft) from the end of the pile that could not be broken or removed. The object was believed to be a boulder, but potentially may have been the detached steel driving shoe which was cast into the concrete filling of the pile. It was initially driven at fuel setting 2 for 4 blows. Then the fuel setting was increased to 3 and the pile was driven 229 more mm (9 in) to a final elevation of -8.86 m (-29.08 ft). The reported capacity of Pile C in the field based on the Case Method was 3340 kN (750 kips) [34, 43]. After analysis of the data, GZA found that the dynamic pile testing data was not reliable for Pile C [34, 41].

Upon the extraction of Pile C, it was found that 1.37 m (4.5 ft) had broomed at the pile toe. The condition of the toe of Pile C after the restrike can be seen in Figure 4.14.

Figure 4.14 Toe of Pile C after Restrike

4.5.4 Pile D

Pile D had 8 reinforcing layers, 25.4 mm (1 in) nominal wall thickness, and was driven hollow for the initial driving and restrike. After the pile was extracted, it was cut into 1.52 m (5 ft) samples and tested into axial compression.

4.5.4.1 Initial Driving

Pile D was driven to an elevation of -7.62 m (-25 ft). At this depth, the PDA showed damage 6.10 m (20 ft) from the top of the pile. Driving continued to an elevation of -8.08 m (-26.5 ft) when the top of the pile failed. Stopping criteria for this pile was 11 blows per 25 mm (1 in) at fuel setting 2 and stroke of 2.59 m (8.5 ft). At failure, the blow count was 2 blows per 25 mm (1 in). The reported capacity of Pile D in the field based on the Case Method was 2670 kN (600 kips) [34, 42]. After further analysis, GZA revised the Case Method capacity to 2270 kN (510 kips) and calculated a CAPWAP capacity of 1960 kN (440 kips) with 14% skin friction and 86% end bearing [34, 40].

The condition of the head of Pile D after initial driving can be seen in Figure 4.15.

Figure 4.15 Head of Pile D after Initial Driving

50

4.5.4.2 Restrike

Pile D was driven on fuel setting 2 for 178 mm (7 in) and showed plugging at an elevation of -6.98 m (-22.91 ft). The fuel setting was then increased to 3 and driven for an additional 178 mm (7 in) to a final elevation of -8.43 m (-27.67 ft). During driving the pile was visibly flexing. The reported capacity of Pile D in the field based on the Case Method was 2890 kN (650 kips) [34, 43]. After further analysis, GZA revised the Case Method capacity to 2050 kN (460 kips) and calculated a CAPWAP capacity of 1960 kN (440 kips) with 18% skin friction and 82% end bearing [34, 41].

Upon the extraction of Pile D, it was found that 1.22 m (4 ft) had broomed at the pile toe. The condition of the toe of Pile D after the restrike can be seen in Figure 4.16.

Figure 4.16 Toe of Pile D after Restrike

4.6 Discussion of FRP Pile Driving

4.6.1 Allowable Driving Stresses

Currently, there is no standard method for determining allowable driving stresses in FRP piles. The Federal Highway Administration [44] has set criteria for conventional piling materials, which can be seen in Table 4.4, where f_y is the yield stress of steel or steel reinforcing bars, f_c' is the compressive strength of concrete, f_{pe} is the effective prestress after losses, and σ_a is the American Association of State Highway and Transportation Officials (AASHTO) allowable working stress for the specific species of timber pile. Allowable driving stresses for FRP piles may be dictated by the manufacturing process, type of reinforcement, and orientation of fibers used to construct the piles.

Table 4.4 Allowable Driving Stresses for Conventional Pile Materials

Pile Type	Maximum Allowable Driving Stress	
Steel Pipe and H-Piles	$0.90\ f_y$	
Prestressed Concrete	$0.85\ f_c' - f_{pe}$	Compression
	$0.25\ \sqrt{f_c'} + f_{pe}$	Tension (SI Units)
Reinforced Concrete	$0.85\ f_c'$	Compression
	$0.70\ f_y$	Tension
Timber	$3\ \sigma_a$	

For the piles in this study, pile heads failed at 11% of the coupon-level compressive strength. This is notably smaller than allowable driving stresses for any of the conventional pile materials. Guades and Aravinthan [31] found that impacted FRP tubes appear to reach a limit of strength degradation at smaller driving energies. As the number of blows increases, strength loss appears to stop changing. This may mean that the use of smaller hammers at higher blow counts will limit damage.

52

Impacted FRP tubes exhibit micro-cracking when examined under a microscope, even in samples that did not become visibly damaged [31]. This may result in a decrease in strength of the composite or increased susceptibility to environmental damage.

4.6.2 Tensile Pile Driving Stresses in Concrete

The FRP piles driven at Richmond-Dresden were tested to failure in flexure in the laboratory after being extracted. This is discussed further in Chapter 5. Both concrete-filled FRP piles that received hammer blows during initial driving and during the restrike (Piles A and D, respectively), failed in flexure when the concrete infill slid relative to the FRP shell. The movement of the concrete was relatively small in Pile A because it was restrained by the closed driving shoe. The loss of composite action in Pile A was evident due to a loud cracking noise and the pile jumping in its supports. The movement of concrete in Pile C was much more noticeable because the concrete infill was not restrained by an end cap. This behavior was not seen in any of the baseline piles that had been filled with concrete or piles subjected to 20,000 load cycles. Therefore it is believed that horizontal cracks formed during driving and created a plane for the pile to fail by loss of composite action. The loss of composite action can be seen in Figure 4.17.

| (a) | (b) | (c) |
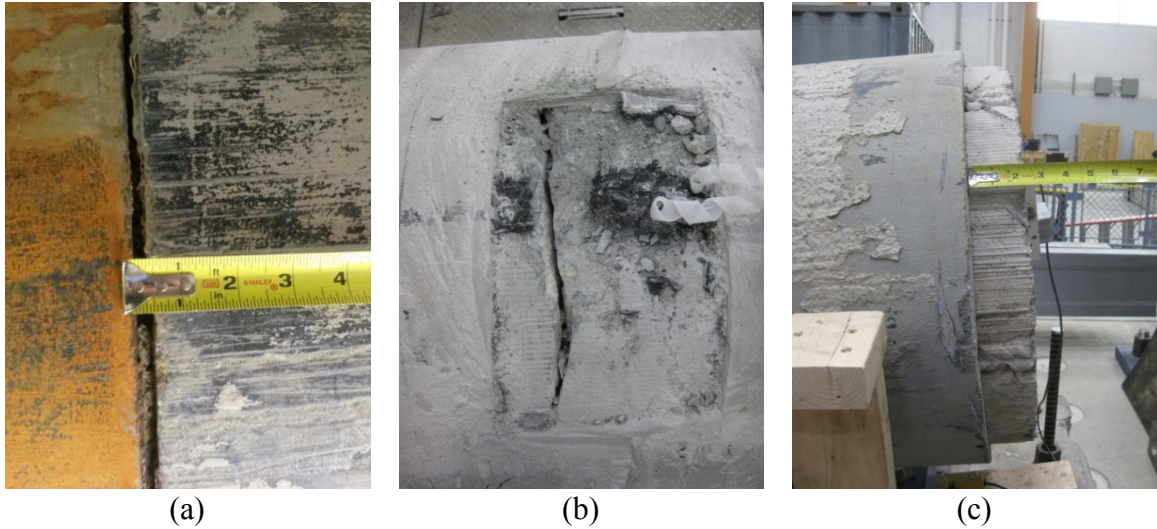
Figure 4.17 Concrete Movement in Pile A (a), Internal Cracking in Pile A (b), and
Concrete Movement in Pile C after Loss of Composite Action (c)

Concrete-filled FRP piles driven by Baxter et al [32] had pile integrity testing
(PIT) conducted before and after driving. The pre-driving PIT test showed a potential
crack that was believed to have occurred during transport or handling. The post-driving
PIT test showed a highly irregular wave which is indicative of significant cracking and
damage. This damage is believed to have occurred when the pile encountered heavy
driving.

Mirmiran et al [28] found that during driving their concrete-filled FRP pile
reached an axial tensile stress of 23 MPa. The theoretical allowable tensile strength of the
unreinforced concrete on this project would be 3.6 MPa using Equation 4.1, where f_c' is
the compressive strength of the concrete in MPa [45]. It should be noted that this is an
allowable static stress in flexure, and the FRP shell may provide some longitudinal
reinforcement during driving. This may mean that cracks developed during pile driving
that went undetected; however no PIT tests are available to confirm this. This damage
would be similar to that seen by Baxter et al [32] and this study. No damage was noted to

the unreinforced piles driven by Pando et al [2], but tensile driving stresses did not exceed the theoretical limit found using Equation 4.1.

$$f_t = 0.62\sqrt{f_c'}$$
<div align="right">Equation 4.1</div>

4.6.3 Toe Driving

Sakr et al [29] found that FRP piles require 43% less energy when installed using toe driving compared to conventional driving, while steel piles required only 7% less energy. They believe this is related to the lower impedance of FRP piles and direct transfer of energy to the soil. The toe driving system also reduced driving stresses in the pile wall. FRP piles driven using conventional methods had a peak force of 282 kN in compression, while the piles driven with the toe driving system saw a peak force of 125 kN in tension. The magnitude of the peak forces is not only reduced using this method, but they switch from compression to tension. The failure mode seen in the piles driven at Richmond-Dresden appears to be caused by compression as layers of reinforcement delaminate. If the major driving forces are converted from compression to tension, then this failure mode may be eliminated.

A study by Guades and Aravinthan [31] shows that the reduction in tensile strength of bench-scale piles with simulated driving at the pile head is negligible. This may be a favorable trait for piles driven using the toe driving technique. If the largest driving stresses correspond to the loading orientation with the least reduction due to impact, then damage may be avoided. It was also demonstrated that the tensile strength of bench-scale piles is not very sensitive to the number of impacts, while the compressive and flexural strengths were greatly reduced [31].

Iyer [30] also demonstrated that FRP piles could be driven to a capacity of 1935 kN (435 kip) using a steel pipe mandrel and flat driving shoe. The pile in this study did not show any damage.

4.6.4 Lateral Restraint at Critical Areas

Hollow FRP piles in this study exhibited a brooming failure when layers of reinforcement delaminated at the head of the pile under impact loading. Adding lateral restraint at critical locations such as the pile head may increase the allowable driving stress.

One possible method for adding lateral restraint is used to limit damage in timber piles. Metal strapping is used to prevent a similar failure at the head of timber piles [44]. However, this solution may not be effective for hollow FRP piles if there is nothing for the metal strapping to react against inside the pile.

4.6.5 Selecting Appropriate Sites

If FRP piles are driven to bedrock in areas with sloping bedrock or encounter obstructions such as boulders, the toe of the pile may see stress concentrations. The relatively low driving stresses at failure seen at the pile head indicate that stress concentrations at the toe may be a critical concern. This is illustrated in Figure 4.18.
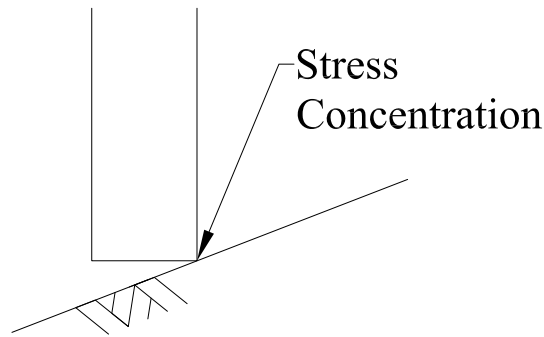
Figure 4.18 Stress Concentration on Sloping Bedrock

The geotechnical report for the Richmond-Dresden driving site [34, 35] shows bedrock with an approximate linearly interpolated slope of 3.2% between Pier 5 and Pier 6 of the proposed bridge. This slope was calculated using bedrock elevations and stations from boring logs BB-RDKR-207 and 208. Boring logs at Pier 5 and Pier 6 also indicated cobbles and boulders. The toe damage seen on piles that were driven hollow is more severe on one side of the pile, indicating that it may have occurred when an obstacle or sloping bedrock was encountered. The orientation of the toe damage relative to the interpolated bedrock elevation is unknown. The toe damage can be seen in Figure 4.19.

(a)   (b)

Figure 4.19 Sloping Toe Damage on Pile C (a) and Pile D (b)

Until a method for limiting stresses and damage at the toe of FRP piles has been developed, it may be appropriate to limit their use to certain subsurface conditions. These piles may be more suitable in scenarios where a significant portion of their capacity is developed as skin friction and in areas without obstructions. Similar limitations are suggested for timber piles by the FHWA [44].

4.6.6 Temperature During Driving

Temperature at the top of the pile may also be a concern. During driving, temperatures increase as energy is imparted from the hammer to the pile cushion. The temperature can rise to levels where plywood pile cushions can catch fire during heavy driving. The Canadian Plywood Association notes a typical autoignition temperature of 273 °C (523 °F) for plywood [46]. This is over three times higher than the glass transition temperature of the FRP shell, which is discussed in 2.6. This means the FRP shell may have been damaged if the glass transition temperature was exceeded, leading to failure at the top of the pile. No temperature measurements were taken in the field to suggest this caused the failure of piles in this study.

CHAPTER 5 RESIDUAL PROPERTIES OF DRIVEN AND CYCLICALLY LOADED FRP PILES TESTED IN FLEXURE

5.1 Literature Review

5.1.1 Static Loading

Helmi et al [47] studied the effects of pile driving on the flexural capacity of concrete-filled fiber reinforced polymer (FRP) piles. This test loaded 357 mm (14 in) diameter piles in four point bending with a span of 5 m (16.4 ft). A sample was cut from the head and toe of a driven pile and compared to an undriven control sample. The driven piles did not exhibit a cracking load, which suggests that the concrete was cracked during driving. Driving reduced the ultimate moment of the piles by 5% in flexure, but driving did not affect the stiffness of the piles. This study also demonstrated a splice for FRP piles that exceeded the moment resistance of the FRP pile.

Fam and Rizkalla [48] tested concrete-filled FRP tubes ranging from 89 to 942 mm (3.5 to 37 in) in diameter with 1.07 to 10.4 m (3.5 to 34.1 ft) span lengths. This study examined tubes of different fiber architecture and materials. It was found that tubes with a large percentage of the reinforcement in the axial direction exhibit higher strength and stiffness in flexure, but a lack of adequate hoop reinforcement may allow concrete-filled piles to fail in compression or shear. Some samples were tested with a longitudinal hole inside the concrete. This led to higher strength/weight ratios than FRP piles with a solid concrete core. Testing showed that the load-deflection relationship of concrete-filled FRP piles was approximately linear due to the low cracking moment/ultimate moment ratio. A similar trend was seen in testing by Helmi et al [47].

Ahmad et al [49] tested concrete-filled FRP tubes with span/depth ratios of 0.9 to 6.25 to compare the behavior of short, deep, and slender beams. Despite the small span/depth ratios, shear failures were not observed in this testing. This program found that deep beams saw more slippage of concrete relative to the FRP shell than slender beams, which could be an artifact of the short development length for shear resistance to develop at the FRP-concrete interface. Deep beams also had higher moment capacities. Specimens were cut after testing to reveal compression struts had formed, which transferred load directly to the end supports.

Davol et al [50] conducted a series of tests to produce a model of concrete-filled FRP tubes in flexure that incorporates confined concrete, shear behavior of concrete-filled tubes, and moment curvature of flexural tests. Flexural testing was conducted on two hollow FRP beams with different properties. These tests found that the piles failed by local buckling at 0.55% and 0.83% longitudinal compressive strain. The pile which failed at a higher strain had more hoop reinforcement.

Cole and Fam [51] conducted tests on concrete-filled FRP tubes with longitudinal reinforcement. This study looked at glass fiber reinforcing bars, carbon fiber reinforcing bars, and conventional steel rebar. This study found that the concrete-filled FRP tubes with steel rebar were much more ductile and exhibited a progressive failure. Tubes with carbon or glass fiber reinforcing bars failed suddenly. Cole and Fam also present a model that predicts the performance of reinforced concrete-filled FRP tubes.

5.1.2 Cyclic Loading

Heimi et al [52] conducted fatigue tests on full-scale concrete-filled FRP tubes and FRP coupons. The FRP tubes were cycled at 0.05 Hz in fully reversed cyclic bending, with one sample cycled at 60% of the ultimate moment and one sample cycled at 45% of the ultimate moment. These samples failed after 2,365 cycles and 28,619 cycles respectively. This study showed that strains and deflections gradually increase during fatigue, which indicates a decrease in stiffness. Fatigue tests on FRP coupons suggest that this change in stiffness may be related to cracking of the matrix in the layers of hoop reinforcement.

Ahmad et al [53] conducted fatigue testing on concrete-filled FRP beams with four different fiber architectures and properties. This study found that FRP tubes with lower reinforcement indexes exhibit larger decreases in stiffness and ultimately a shorter fatigue life. Two beams were compared in fatigue loading, one with end restraints and one without end restraints, and it was noted that the end restraints prevented concrete slippage and increased the fatigue by 200 times. Ahmad et al recommend that loading is kept below 25% of the ultimate static strength of the FRP tube. Zhu et al [54] used the findings of these tests to create a model that simulates damage due to fatigue loading in concrete-filled FRP piles.

5.2 Flexural Test

5.2.1 General Test Configuration

All piles were tested in a four-point bending configuration which can be seen in Figure 5.1. The span length for each test was 10.1 m (33 ft). The load was applied using a

single 1330 kN (300 kip) actuator with a spreader beam. Load points were at the 1/3

points of the span, except for testing Pile C when load points were adjusted to create

higher moments. Changes in the test configuration for Pile C will be discussed further in

5.6.

Figure 5.1 Flexural Test Configuration

Saddles with a curvature equal to that of the piles were used at loading points and

end supports to distribute load over the pile. Each saddle was lined with neoprene to aid

in load distribution and a plastic sheet to allow lateral translation. These saddles were

mounted on pinned supports that allowed rotations associated with the large expected

deflections. A saddle and pinned support can be seen in Figure 5.2.

Figure 5.2 Saddle and Support Configuration

5.2.2 Instrumentation

All piles were instrumented with 2 sets of 3 strain gages oriented in the longitudinal direction of the pile. Each set of strain gages has 1 gage at the extreme tension fiber, 1 gage at the mid-height of the cross section, and 1 gage at the extreme compression fiber. An additional strain gage was oriented in the hoop direction at the mid-span of the pile. Strain gages can be seen in Figure 5.3.

(a)   (b)
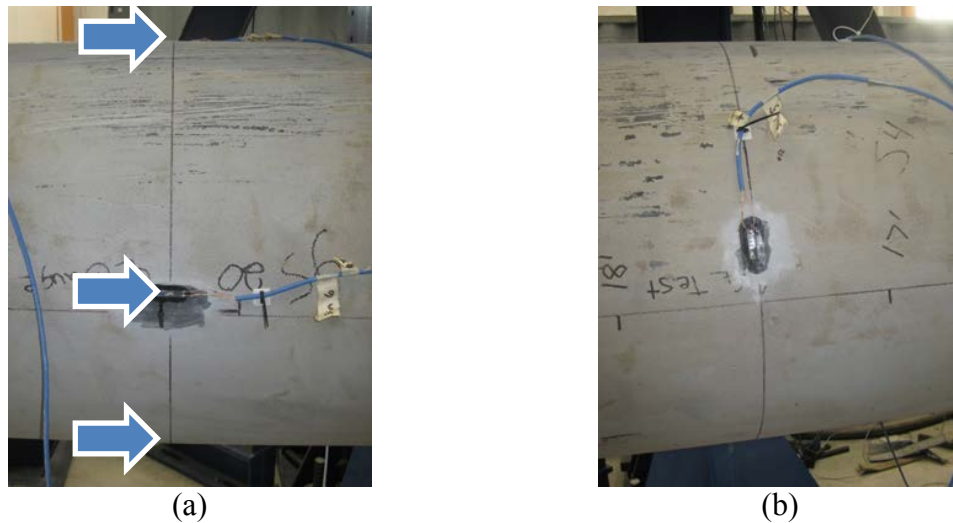
Figure 5.3 Typical Longitudinal (a) and Hoop (b) Strain Gage

Deflections were measured at the mid-point of the span and both loading points using Celesco SP2-50 string potentiometers (string pots). Lateral translations were measured at each support using Celesco SP2-25 string pots. These can be seen in Figure 5.4. All measurements were taken at the mid-height of the cross section.

(a)

(b)
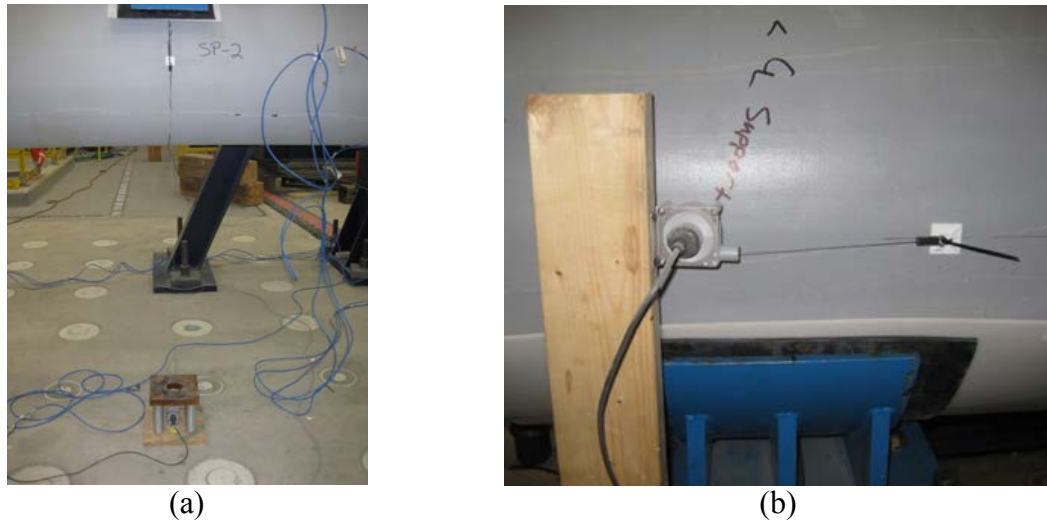
Figure 5.4 Measurement of Vertical Deflection (a) and Lateral Translation (b)

Axial rotation was measured at each pinned end support using +/- 60 degree TURK B2N60H-Q20L60-2LU3/S97 inclinometers. This can be seen in Figure 5.5.

Figure 5.5 Longitudinal Rotation Measurement

64

For hollow piles, ovalization of the piles was measured using Celesco SP2-4 string pots mounted inside the piles. For concrete-filled piles, the same string pot was used to determine concrete-to-shell composite action by measuring relative displacement of the concrete to the FRP shell. These can be seen in Figure 5.6.

(a)   (b)
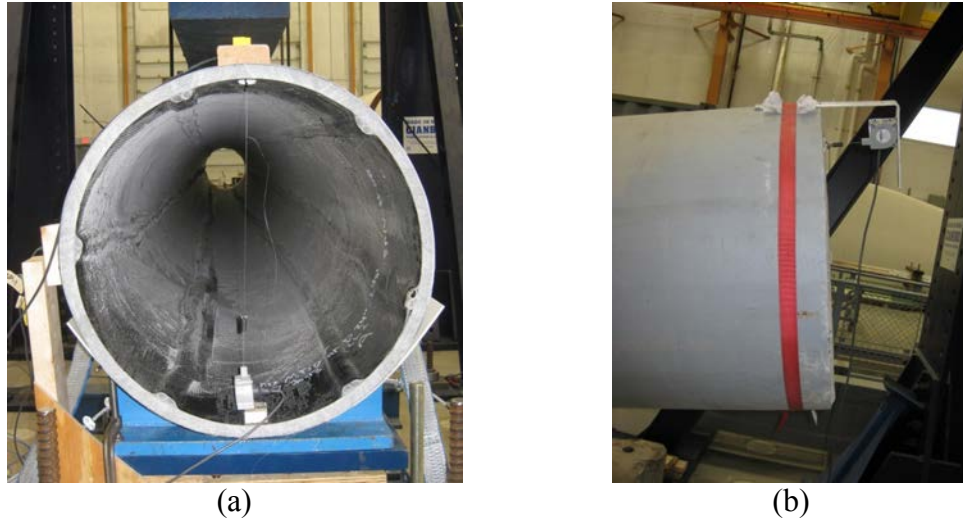
Figure 5.6 Measurement of Ovalization (a) and Concrete-FRP Composite Action (b)

5.2.3 Pile Loading

Flexural tests fell into 2 categories; statically loaded and cyclically loaded. Static piles were loaded to failure by controlling the rate of displacement. Piles were loaded at a rate of 38.1 mm (1.5 in) per minute for the first 381 mm (15 in) of deflection. Then the loading rate was transitioned to 25.4 mm (1 in) per minute using a sinusoidal ramp. A plot of the loading profile can be seen in Figure 5.7.
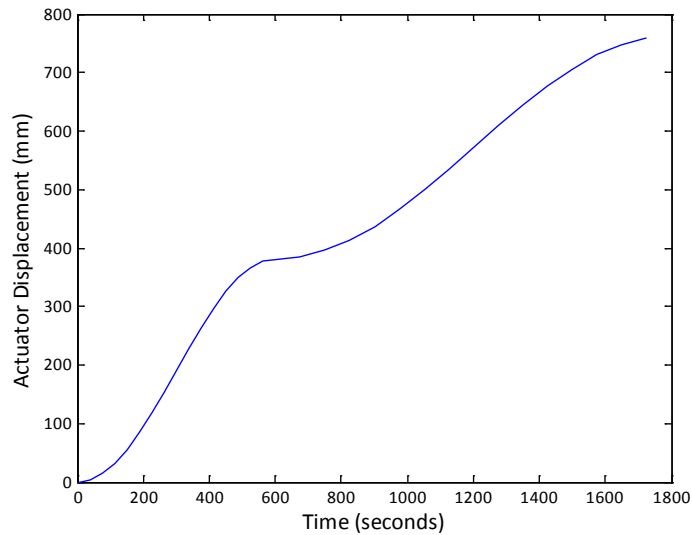
Figure 5.7 Static Loading Profile

Load-cycled piles were loaded to approximately 50% of the average ultimate load piles determined during static testing. This load was determined to be 334 kN (75 kips). The piles were cycled between 33.4 kN (7.5 kips) and 334 kN (75 kips) for 10,000 cycles at a frequency of 0.05 Hz. After 10,000 cycles, the piles were rotated 180 degrees about their longitudinal axis and subjected to an additional 10,000 cycles. Then, the piles were tested statically to failure. Strain and displacement measurements were taken at the maximum and minimum load of each cycle. Data was collected over the entire loading cycle for 10 cycles every 1,000 cycles. A plot of the loading profile can be seen in Figure 5.8.
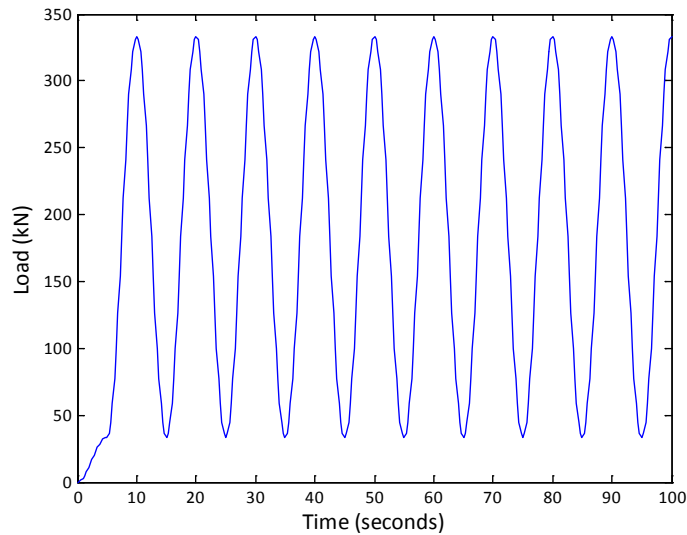
Figure 5.8 Cyclic Loading Profile

5.3 Description of Piles

Driven piles were delivered to the Richmond-Dresden bridge site in early August 2013. This set of piles contained (1) 4 ply pile with a nominal shell thickness of 12.7 mm (0.5 in) and (3) 8 ply piles with a nominal shell thickness of 25.4 mm (1 in). On August 14, 2013, (1) 4 ply pile (Pile A) was completed filled with concrete and (1) 8 ply pile (Pile B) had a 1.22 m (4 ft) concrete plug cast at its toe. All piles to be driven were stored on site until pile driving took place on August 28, 2013. Piles remained in the ground until they could be removed and shipped to the University of Maine on October 15, 2013 and November 8, 2013.

Baseline and load-cycled piles were delivered to the Richmond-Dresden bridge site in early September. This set of piles contained (4) 4 ply piles and (2) 8 ply piles. On September 27, 2013, (4) 4 ply piles were filled with Maine Department of Transportation (MaineDOT) Class A concrete having a target 28 day compressive strength of 30 MPa

67

(4.35 ksi). These piles also remained on site until they could be shipped to the University

of Maine on October 15, 2013 and November 8, 2013.

A summary of all the piles can be seen in Table 5.1.

Table 5.1 Summary of Piles Tested in Flexure

Letter Designation	Number of Plys in Shell	Type of Concrete	Pile ID	Type	Delivered Length (m)
A	4	F[a]	Pile A-4FB	Driven	12.3
B	8	P[b]	Pile B-8PB	Driven	11.9
C	8	HF[c]	Pile C-8HFB	Driven	10.6
E	4	F	Pile E-4FB	Load-Cycled	12.2
F	4	F	Pile F-4FB	Load-Cycled	12.2
G	4	F	Pile G-4FB	Baseline	12.2
H	4	F	Pile H-4FB	Baseline	12.2
I	8	H[d]	Pile I-8HB	Baseline	12.2
J	8	H	Pile J-8HB	Baseline	12.2

[a]F denotes piles that are completely filled with concrete
[b]P denotes piles that were driven with a 1.22 m concrete plug which was removed prior to flexural testing
[c]HF denotes piles that were initially driven hollow and filled with concrete before the restrike
[d] H denotes a hollow pile

Pile D was not tested in flexure due to excessive damage from the pile extraction

process. The damage can be seen in Figure 5.9.

Figure 5.9 Damage to Pile D from Pile Extraction

5.4 Hollow Pile Test Results

5.4.1 Baseline Pile Test Results

5.4.1.1 Pile I-8HB

Pile I failed by compression at a load of 543 kN (122 kips) and a corresponding moment of 912 kN-m (673 kip-ft). It is believed that the layers of reinforcement delaminated, and then buckled locally. The failure occurred approximately 0.30 m (1 ft) from the nearest loading point (inside the constant moment region) and can be seen in Figure 5.10.

Figure 5.10 Compression Failure of Pile I

5.4.1.2 Pile J-8HB

Pile J failed by compression at a load of 400 kN (90 kips) and a corresponding moment of 667 kN-m (492 kip-ft). It is believed that the layers of reinforcement delaminated, and then buckled locally. The failure occurred at the mid-span of the pile and can be seen in Figure 5.11.

Figure 5.11 Compression Failure of Pile J

5.4.2 Driven Pile Test Results

5.4.2.1 Pile B-8PB

Pile B failed by compression at a load of 485 kN (109 kips) and a corresponding moment of 812 kN-m (599 kip-ft). It is believed that the layers of reinforcement delaminated, and then buckled locally. The failure occurred approximately 0.30 m (1 ft) from the nearest loading point (inside the constant moment region) and can be seen in Figure 5.12. Upon further investigation, this pile contained folds in the reinforcing fabric and pockets of high resin content located near the failure. This is discussed further in 5.4.4.

Figure 5.12 Compression Failure of Pile B

5.4.3 Summary of Hollow Piles

Maximum loads and deflections of hollow piles tested in flexure are presented in Table 5.2. Load-deflection and moment-curvature relationships are presented in Figure 5.13 and Figure 5.14 respectively.

Table 5.2 Maximum Loads and Deflections of Hollow Piles in Flexure

Pile ID	Type	Maximum Load at Actuator (kN)	Maximum Deflection at Mid-span (mm)	Maximum Deflection at Load Point (mm)
Pile I-8HB	Baseline	543	186	190
Pile J-8HB	Baseline	400	161	140
Pile B-8PB	Driven	485	204	177
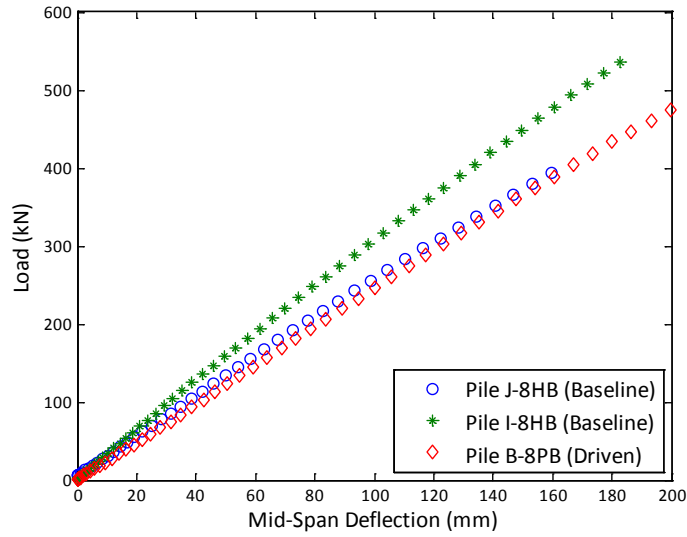
Figure 5.13 Load-Deflection of Hollow Piles in Flexure
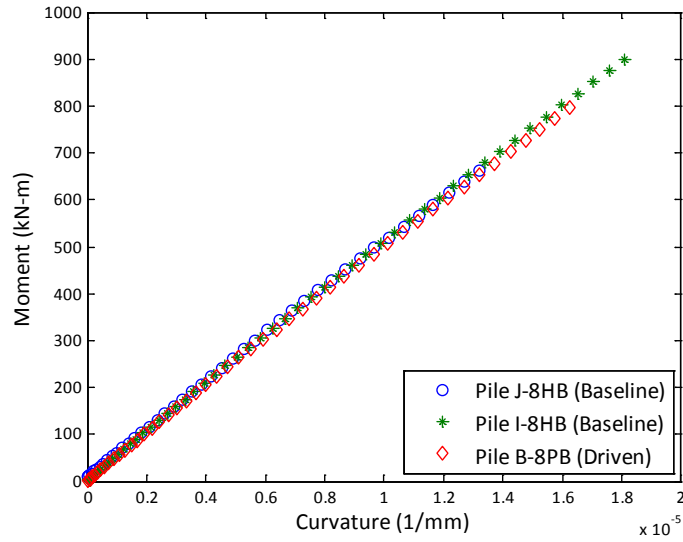
Figure 5.14 Moment-Curvature of Hollow Piles in Flexure

5.4.4 Discussion of Hollow Piles

Piles were cut into approximately 1.52 m (5 ft) sections for disposal. When Pile B was cut for disposal, defects were exposed in the FRP shell near the location of failure. Folds in the reinforcing fabric and areas of high resin content were noted. These can be seen in Figure 5.15. These defects were not seen in any other piles, but may have gone undetected.
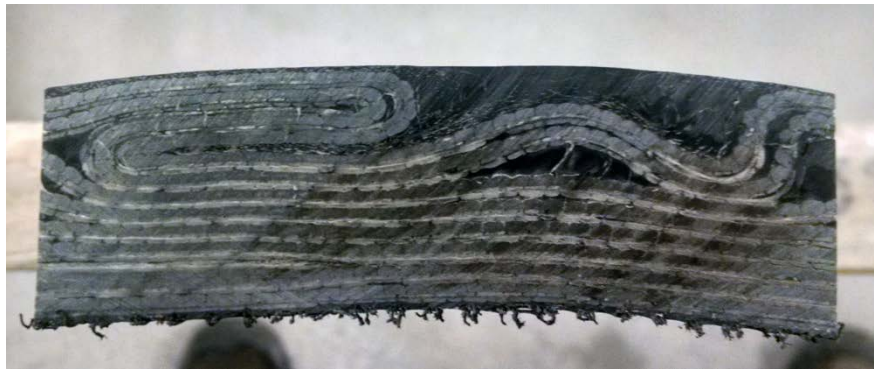
Figure 5.15 Folds in Reinforcing Fabric and Areas of High Resin Content in Pile B

Fiber volume fraction (FVF) testing was conducted on hollow piles according to ASTM D2584 [55]. A sample was cut near each end support and near the failure to examine any changes in FVF along the length of the pile. Fiber volume fraction testing results can be seen in Table 5.3. The FVF values at "End Support A" and "End Support B" do not correspond to a specific end support. This notation is used to show that the samples were cut from opposite ends of the pile.

Table 5.3 Fiber Volume Fraction Results for Hollow Piles in Flexure

Pile ID	FVF at End Support A	FVF at Failure	FVF at End Support B
Pile I	50.5	55.3	49.6
Pile J	51.0	52.7	49.7
Pile B	56.3	41.3 , 58.9[a]	53.3

[a] Multiple samples tested due to areas of high resin content and high fiber content

The samples tested near the failure of Pile B included defects. One sample with high resin content was tested and another sample with high fiber content was tested to provide an approximate upper and lower bound of FVF values. These samples can be seen in Figure 5.16.

(a)　　　　　　　　　　(b)　　　　　　　　　　(c)
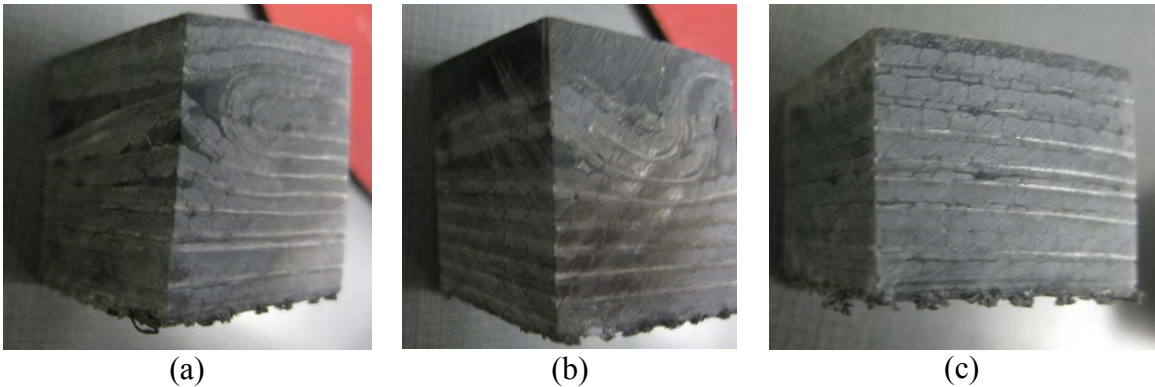
Figure 5.16 FVF Samples with High Fiber Content in Pile B (a), High Resin Content in Pile B (b), and Typical Fiber/Resin Content (c)

5.5 Concrete-Filled Piles

5.5.1 Baseline Pile Test Results

5.5.1.1 Pile G-4FB

Pile B failed at a load of 890 kN (200 kips) and a corresponding moment of 1490 kN-m (1099 kip-ft) when fibers on the tension face appeared to rupture. The failure

occurred approximately 0.30 m (1 ft) from the nearest loading point (outside the constant moment region) and can be seen in Figure 5.17.

Figure 5.17 Tension Failure of Pile G

Strain data for this test could not be recovered over +/- 5000 microstrain due to an error in the data collection system.

5.5.1.2 Pile H-4FB

Pile H failed at a load of 529 kN (119 kips) and a corresponding moment of 884 kN-m (652 kip-ft) when fibers on the tension face appeared to rupture. The failure occurred at the mid-span of the pile and can be seen in Figure 5.18.

Figure 5.18 Tension Failure of Pile H

Strain data for this test could not be recovered over +/- 5000 microstrain due to an error in the data collection system.

5.5.2 Driven Pile Test Results

5.5.2.1 Pile A-4FB

Pile A failed at a load of 774 kN (174 kips) and a corresponding moment of 1299 kN-m (958 kip-ft) when fibers on the tension face appeared to rupture. The failure occurred approximately 0.61 m (2 ft) from the nearest loading point (inside the constant moment region) and can be seen in Figure 5.19.

Figure 5.19 Tension Failure of Pile A

A compression wrinkle developed approximately 0.30 m (1 ft) from the nearest loading point (outside of the constant moment region) at an approximate load of 689 kN (155 kips) and a corresponding moment of 1157 kN-m (853 kip-ft). After testing, the FRP shell was cut at the compression wrinkle and a crack that went through the cross-section was discovered. It is believed that this crack occurred during driving. The compression wrinkle and crack can be seen in Figure 5.20.

(a)   (b)

Figure 5.20 Compression Wrinkle (a) and Internal Cracking (b) in Pile A

When the compression wrinkle occurred, the concrete moved with respect to the

FRP shell of the pile. The concrete displacement measurement during the test was

unreliable due to a failure of the string pot. The concrete movement was measured to be

6.22 mm (0.245 in) at the end of the pile. This can be seen in Figure 5.21.

Figure 5.21 Concrete Movement in Pile A

Test data was lost for portions of this test due to an error in the data collection

system. Data was recovered for the failure of the pile and loss of composite action.

5.5.3 Load-Cycled Pile Test Results (Static Test to Failure)

5.5.3.1 Pile E-4FB

Pile E was subjected to 20,000 load cycles as described in 5.2.3. During cyclic

loading, Pile E developed small cracks along the tension face. This can be seen in Figure

5.22. The cracks appeared to only be surficial.

Figure 5.22 Cracking of FRP Shell in Pile E during Cyclic Loading

After cyclic loading, Pile E was tested statically to failure. This pile initially
showed a compression failure at 703 kN (158 kips) and the load dropped to 663 kN (149
kips). The load started to rise again to 703 kN (158 kips) and a corresponding moment of
1181 kN-m (871 kip-ft) where the pile appeared to fail in tension. The failure occurred at
the mid-span of the pile and can be seen in Figure 5.23.

Figure 5.23 Tension Failure of Pile E

5.5.3.2 Pile F-4FB

Pile F was subjected to 20,000 load cycles as described in 5.2.3. After cyclic loading, Pile F was tested statically to failure. Pile F failed at a load of 565 kN (127 kips) and a corresponding moment of 948 kN-m (699 kip-ft) when fibers on the tension face appeared to rupture. The failure occurred at the mid-span and can be seen in Figure 5.24.

Figure 5.24 Tension Failure of Pile F

5.5.4 Summary of Concrete-Filled Pile Tests

Maximum loads and deflections of concrete-filled piles tested in flexure can be seen in Table 5.4. Load-deflection and moment-curvature relationships are presented in Figure 5.25 and Figure 5.26 respectively.

Table 5.4 Maximum Loads and Deflections of Concrete-Filled Piles in Flexure

Pile ID	Type	Maximum Load at Actuator (kN)	Maximum Deflection at Mid-span (mm)	Maximum Deflection at Load Point (mm)
Pile G-4FB	Baseline	890	551	475
Pile H-4FB	Baseline	529	236	238
Pile A-4FB	Driven	774	495	432
Pile E-4FB	Load-Cycled	703	363	308
Pile F-4FB	Load-Cycled	565	253	217
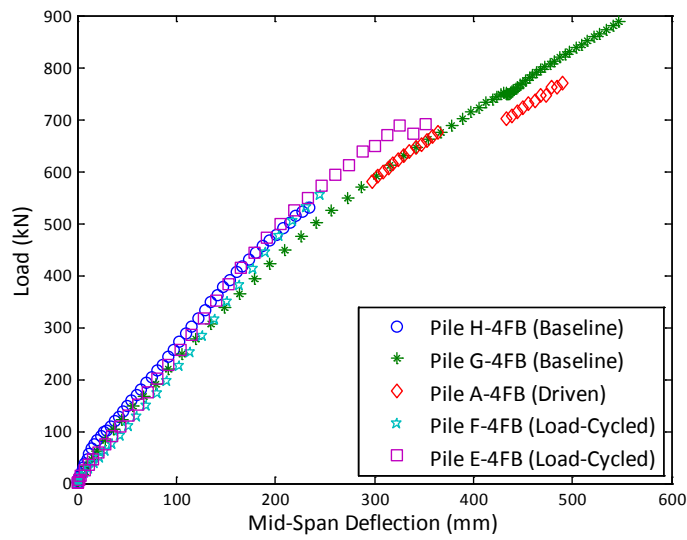
Figure 5.25 Load-Deflection of Concrete-Filled Piles in Flexure
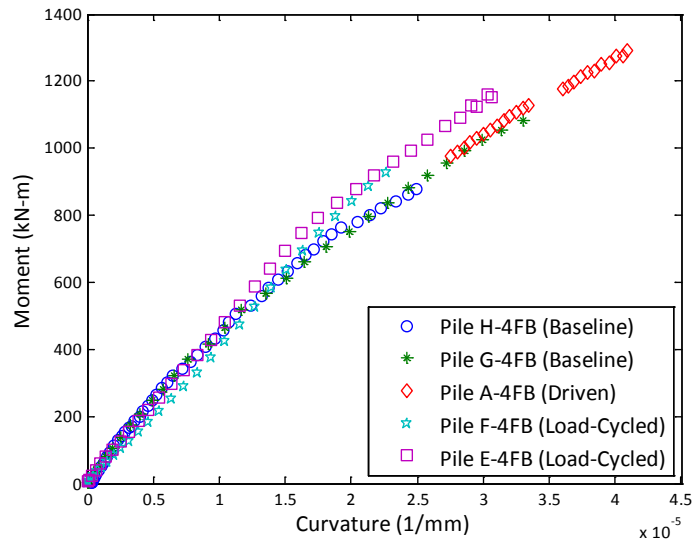
Figure 5.26 Moment-Curvature of Concrete-Filled Piles in Flexure

5.5.5 Discussion of Concrete-Filled Piles

When concrete-filled piles were cut for disposal, the concrete showed a clear compression and tension zone. This can be seen in Figure 5.27.
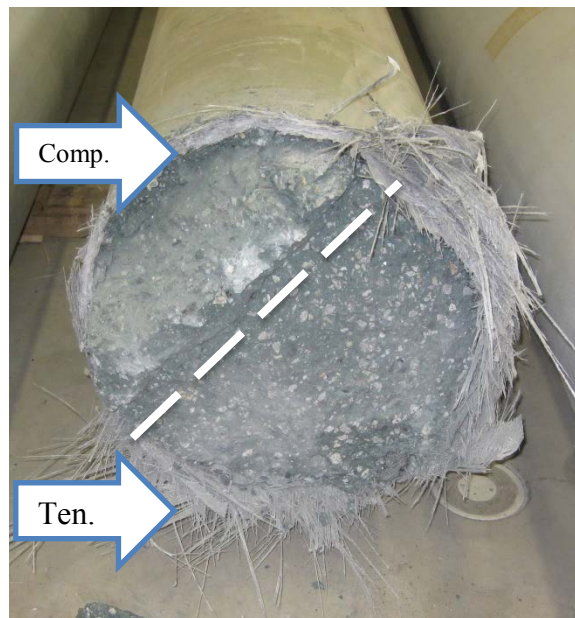
Figure 5.27 Tension and Compression Zone in Concrete-Filled Pile

The interface between the concrete and FRP shell was also examined after piles were cut for disposal. No gaps or damage at the interface were seen in the cross-sections of baseline or load-cycled piles. A typical cross section can be seen in Figure 5.28.

Figure 5.28 Concrete-FRP Interface

5.6 Pile C Tests

Pile C was constructed using 8 layers of reinforcement and was filled with concrete. This pile exceeded the capacity of the test equipment with the span length used for other piles. The loading points were adjusted to increase the maximum available moment with a 1330 kN (300 kip) actuator. Changes in the test geometry are summarized in Table 5.5 and illustrated in Figure 5.29.

Table 5.5 Test Geometry of Pile C Tests

Test	"a" Dimension (m)	Maximum Available Moment (kN-m)
Pile C Test 1	3.35	2237
Pile C Test 2	3.66	2440
Pile C Test 3	3.96	2644
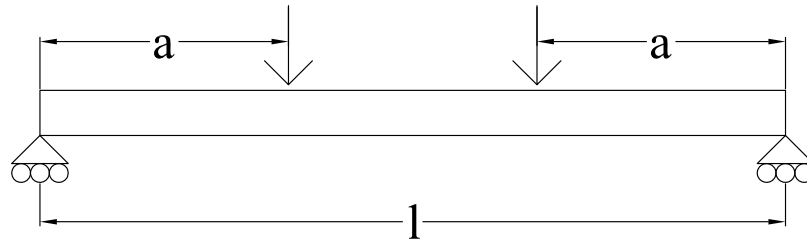
Figure 5.29 Four-Point Bend Configuration

5.6.1 Pile C Test 1

Pile C was first tested using the same test dimensions as all other hollow and concrete-filled piles. The load cell reached its capacity at an applied load of 1330 kN (300 kips) and corresponding moment of 2237 kN-m (1650 kip-ft), ending the test with no failure. The pile developed a series of hairline cracks along the tension face at two points: 0.76 m (2.5 ft) from the nearest load point (inside the constant moment region) and 1.07 m (3.5 ft) from the nearest load point (outside the constant moment region. These cracks can be seen in Figure 5.30.

<div align="center">(a)   (b)</div>
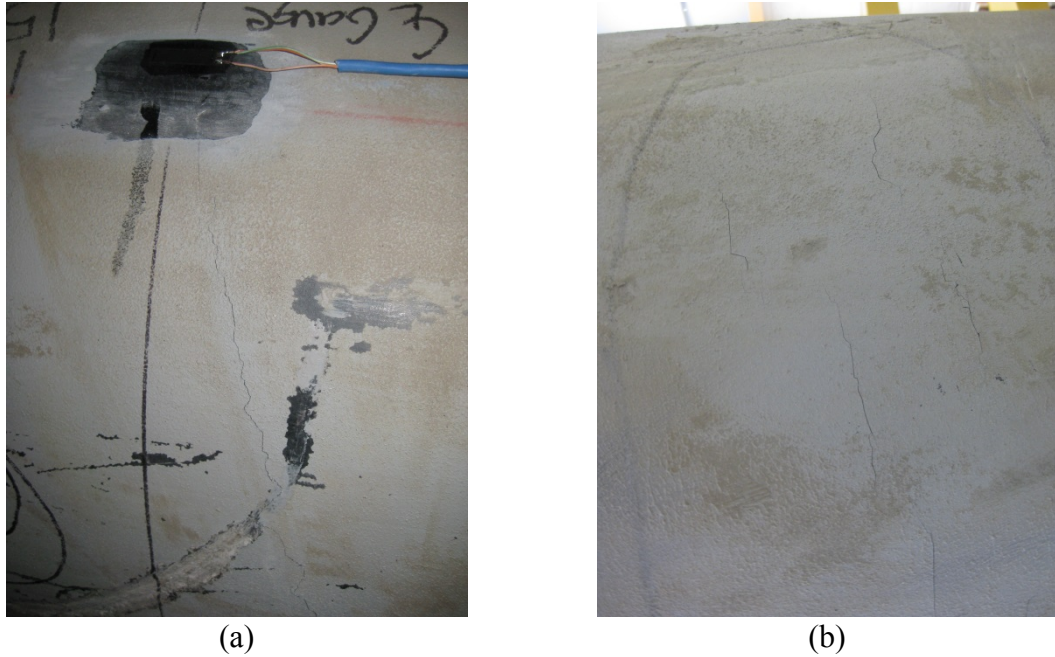
Figure 5.30 Cracks Inside (a) and Outside (b) of the Constant Moment Region

5.6.2 Pile C Test 2

Pile C was tested a second time, with the loading points adjusted to 3.66 m (12 ft) from the end supports. The load cell reached its capacity again at an applied load of 1330 kN (300 kips) and corresponding moment of 2440 kN-m (1800 kip-ft), ending the test with no failure.

5.6.3 Pile C Test 3

Pile C was tested a third time, with the loading points adjusted to 3.96 m (13 ft) from the end supports. After the first two tests, Pile C was rotated 90 degree. This rotation placed previously cracked concrete in the compression zone for test 3. This is illustrated in Figure 5.31.
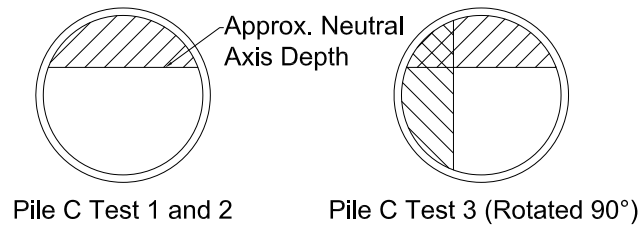
Figure 5.31 Rotation of Pile C prior to Test 3

Composite action was lost during this test when the concrete slid relative to the FRP shell. This occurred when there was a loud crack at an approximate load of 823 kN (185 kips) and corresponding moment of 1631 kN-m (1203 kip-ft). At this load, the concrete measurement recorded by the string pot was found to be 1 mm (0.04 in). When the pile failed, the concrete displacement was much greater and was measured to be 57 mm (2.25 in) after the test. The sliding of the concrete can be seen in Figure 5.32.
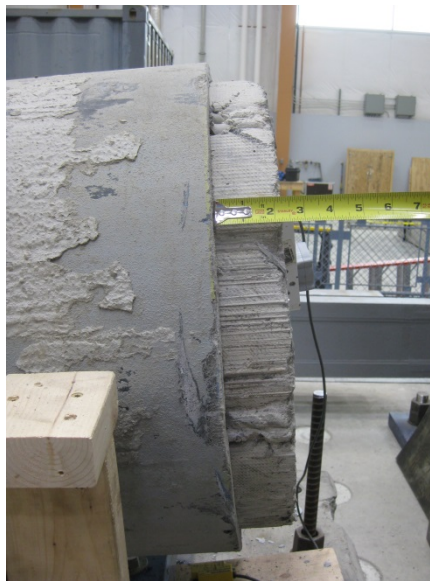
Figure 5.32 Loss of Composite Action in Pile C

Pile C failed in compression at a load of 1170 kN (263 kips) and corresponding moment of 2318 kN-m (1710 kip-ft), which are lower than the load and moment seen in

Pile C Test 2. The pile was able to fail in compression because the concrete slid relative to the FRP shell, creating a void in the pile at the failure location. This can be seen in Figure 5.33.
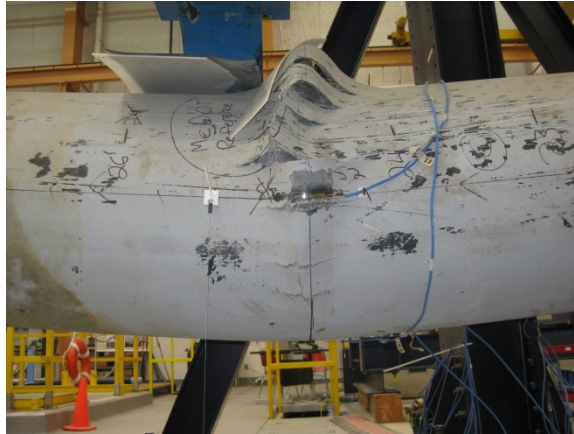
Figure 5.33 Compression Failure of Pile C

5.6.4 Summary of Pile C Tests

Maximum loads and deflections of Pile C tests can be seen in Table 5.6. Load-deflection and moment-curvature relationships are presented in Figure 5.34 and Figure 5.35 respectively. The loss of composite action in Pile C Test 3 can be seen as a discontinuity in Figure 5.34. Load-deflection plots are not directly comparable due to the changes in test dimensions.

Table 5.6 Maximum Loads and Deflections of Pile C in Flexure

Pile ID	"a" Dimension (m)	Maximum Load at Actuator (kN)	Maximum Deflection at Mid-span (mm)	Maximum Deflection at Load Point (mm)
Pile C Test 1	3.35	1330+	454	392
Pile C Test 2	3.66	1330+	475	429
Pile C Test 3	3.96	1170	539	506
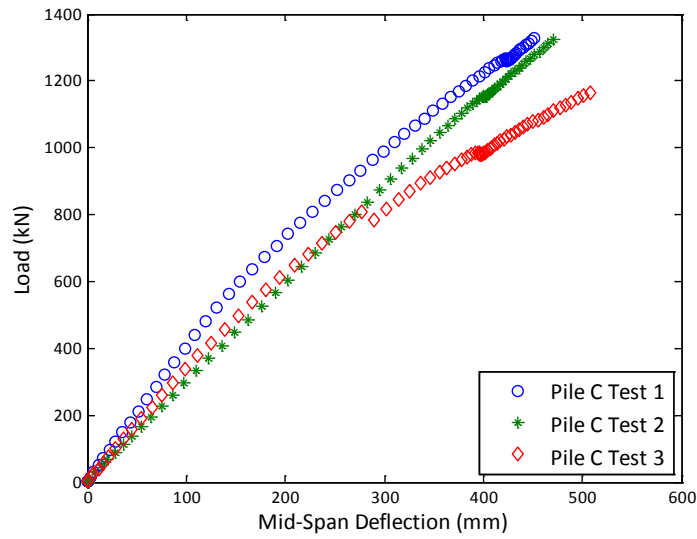
Figure 5.34 Load-Deflection of Pile C in Flexure
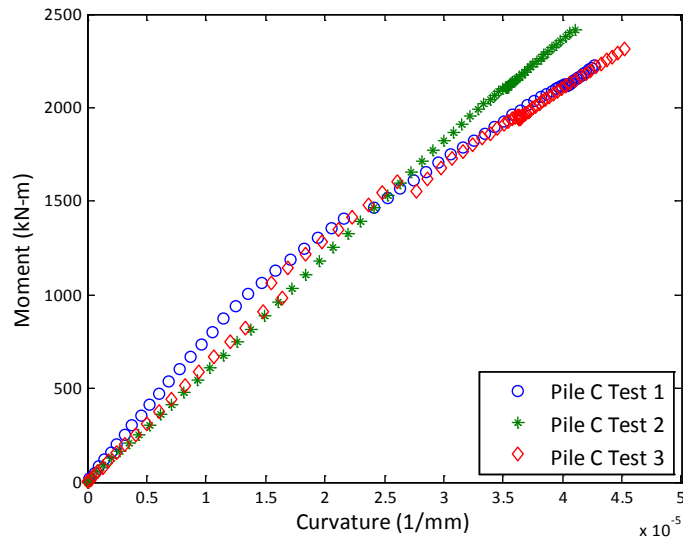
Figure 5.35 Moment-Curvature of Pile C in Flexure

88

5.6.5 Discussion of Pile C Tests

During the third test of Pile C, composite action was lost at an approximate load of 823 kN (185 kips). During this test, higher hoop strain measurements were recorded than during the previous tests of Pile C and all other concrete-filled piles. A plot of hoop strain for Pile C tests can be seen in Figure 5.36.
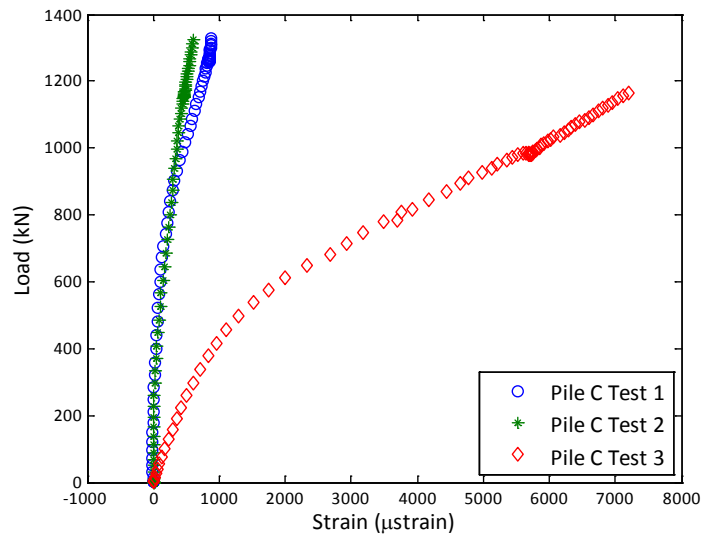
Figure 5.36 Hoop Strain During Pile C Tests

This may indicate that the hoop direction is trying to expand as the concrete slides relative to the FRP shell. This would be a similar phenomenon to dilatancy in direct shear and interface friction testing. Ridges on the flow media, coating the inside the FRP shell, create a mechanical interlocking with the concrete filling. In order for the concrete to slide relative to the FRP shell, this interlocking would need to be overcome by either the concrete sliding over/past the ridges or structural failure of the ridges/concrete. This

sliding may have created the large hoop strains. The ridges in the FRP shell and interlocking with concrete can be seen in Figure 5.37.

(a)   (b)
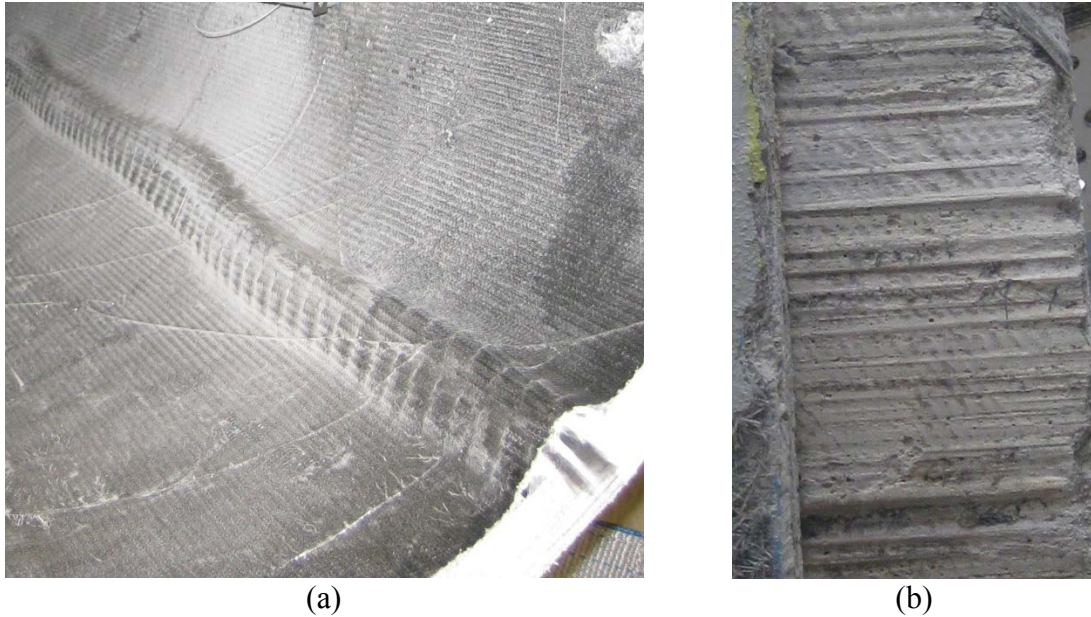
Figure 5.37 Ridges inside FRP Shell (a) and Impressions on Concrete (b)

5.7 Load-Cycled Tests

5.7.1 Summary of Load-Cycled Tests

The behavior of load-cycled piles in static tests did not appear to change after being subjected to 20,000 load cycles. The load-deflection and moment-curvature relationships for load-cycled piles are presented in Figure 5.38 and Figure 5.39 respectively. There was no initial static test for Pile F, so the curves presented as "Pile F Initial" were extracted from a dynamic cycle. This is why these curves do not go through the origin. The static tests to failure of load-cycled piles are described further in 5.5.3.
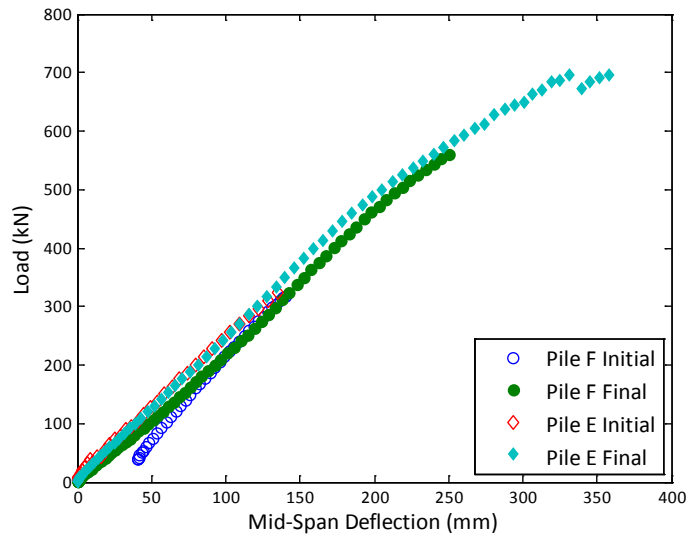
Figure 5.38 Load-Deflection of Load-Cycled Piles in Flexure
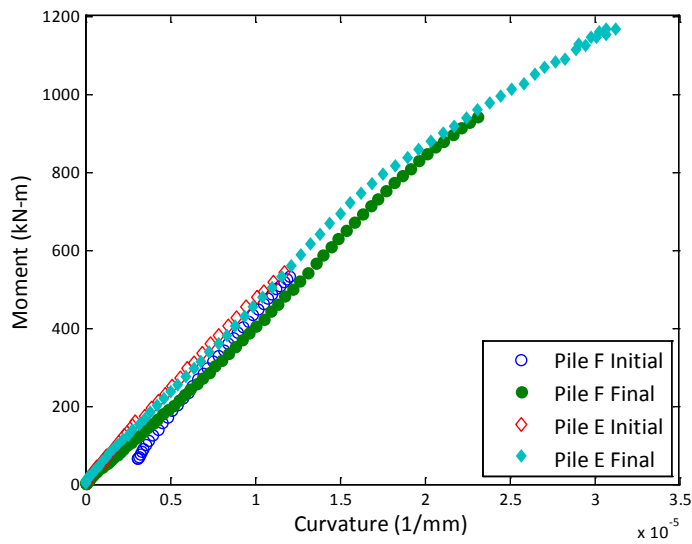
Figure 5.39 Moment-Curvature of Load-Cycled Piles in Flexure

5.7.2 Discussion of Load-Cycled Tests

Stiffness loss due to dynamic loading appears to occur over the first 5,000 cycles

of load-cycled tests. After this initial loss in stiffness, the stiffness remained relatively

constant. This can be seen in Figure 5.40. The pile was rotated 180 degrees after the

initial 10,000 cycles, resulting in an increase in stiffness.

The loss in stiffness seen during cyclic loading was not apparent in the static test

conducted at the beginning of cyclic loading and static test to failure of Pile E. Pile E

showed an increase in stiffness of 0.4% in these static tests, but showed a decrease of

10.1% over the course of cyclic loading. Pile F showed a similar decrease of 14.3% over

the course of cyclic loading. There was no initial static test of Pile F to compare with its

static test to failure.
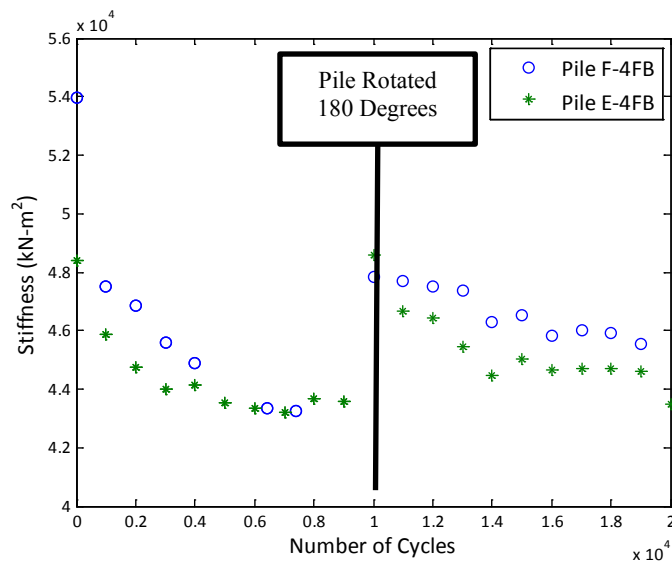
Figure 5.40 Reduction in Dynamic Stiffness with Cyclic Loading

This trend is also apparent when looking at the magnitude of the mid-span

deflection which can be seen in Figure 5.41.
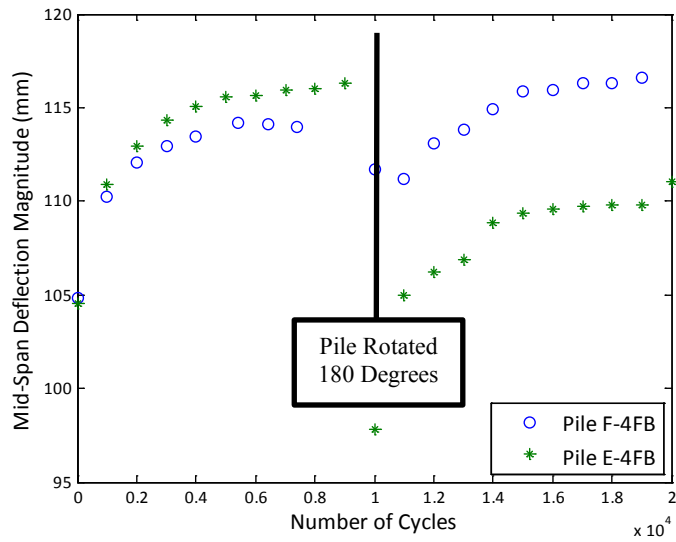
Figure 5.41 Increased Deflection Magnitude with Cyclic Loading

A similar increase in deflection magnitude and loss in stiffness was noted by

Helmi et al [52] and Ahmad et al [53] during fatigue testing of concrete-filled FRP piles.

5.8 Comparison of Flexural Test Results to Predictions

5.8.1 Ultimate Moment Capacity

The ultimate moment and corresponding compressive and tensile strain measured

during testing are presented in Table 5.7. The strain at failure during flexural testing is

compared to the failure strain of longitudinal and compressive coupon tests. The value in

bold denotes the failure mode observed during flexural testing.

Table 5.7 Flexural Strength of FRP Piles

Pile ID	Type	Ultimate Moment (kN-m)	Ultimate Comp. Strain (µstrain)	Percent of Ultimate Coupon Comp. Strain	Ultimate Ten. Strain (µstrain)	Percent of Ultimate Coupon Ten. Strain
Pile I-8HB	Baseline	912	-5.41E+03	**25.7**	5.40E+03	21.2
Pile J-8HB	Baseline	667	-4.09E+03	**19.4**	4.09E+03	16.0
Pile B-8PB	Driven	812	-4.93E+03	**23.4**	4.95E+03	19.4
Pile G-4FB	Baseline	1490		No Strain Data at Failure		
Pile H-4FB	Baseline	884				
Pile A-4FB	Driven	1299	-8.74E+03	41.5	1.69E+04	**66.2**
Pile E-4FB	Load-Cycled	1181	-5.76E+03	27.3	1.26E+04	**49.4**
Pile F-4FB	Load-Cycled	948	-4.59E+03	21.8	9.75E+03	**38.2**
Pile C-8HFB Test 1	Driven	2237+	-8.95E+03	42.5	1.53E+04	60.0
Pile C-8HFB Test 2	Driven	2440+	-9.22E+03	43.8	1.65E+04	64.9
Pile C-8HFB Test 3	Driven	2318	-5.95E+03	**28.2**	1.32E+04	51.6

Testing did not show a clear reduction in the ultimate moment capacity of FRP piles due to driving or cyclic loading. Baseline hollow and concrete-filled piles created an upper and lower bound which bracketed driven and load-cycled piles, making any trend in strength loss inconclusive. This may be a result of the small sample size, or an indication that defects in the piles controlled the ultimate moment. It should be noted that defects in the FRP shell were only discovered in Pile B.

Flexural tests did not reach the ultimate strain seen in coupon level tests. Hollow piles failed in compression at an average of 23% of the coupon strain, while concrete-filled piles failed at an average of 51% of the coupon strain. This may indicate that coupon properties are not a good predictor of the structural capacity of full scale FRP piles.

The ultimate moment found in flexural testing was compared to several models using the average strain at failure from flexural tests. This comparison uses the AASHTO LRFD Guide Specifications for Design of Concrete-Filled FRP Tubes for Flexural and Axial Members [56], a model developed by Davol et al [50], and a calculation developed by Advanced Infrastructure Technologies (AIT). These methods were not developed by the author. The results are presented in Table 5.8. Data for Pile G and Pile H were omitted from the average maximum moment because strain data was unavailable to calculate the average tensile strain at failure. The number in parenthesis indicates the percent difference between the ultimate moment determined by the structural model and the flexural test.

Table 5.8 Correlation Between Flexural Tests and Structural Models for Concrete-Filled Piles

Pile ID	Type	Ultimate Moment from Flexural Test (kN-m)	AASHTO LRFD Simplified Method (kN-m)	Davol et al Moment-Curvature Model (kN-m)	AIT (kN-m)
Pile A-4FB	Driven	1299	1303 (0.3)[a]	1448 (11.5)[a]	1296 (2.3)[a]
Pile E-4FB	Load-Cycled	1181	1025 (13.2)[a]	1166 (1.3)[a]	987 (16.4)[a]
Pile F-4FB	Load-Cycled	948	832 (12.2)[a]	906 (4.4)[a]	777 (18.0)[a]
Average of Pile A, E, F	Various	1143	1058	1217	1023
N/A	Coupon Properties	N/A	1827	2001	1910

[a] Percent difference between the flexural test data and the structural model

These methods predict the ultimate moment within 18.0% when the failure strain from experimental data is used as an input. When failure strains from coupon tests were used as inputs, the ratio of ultimate moment from coupon properties to the average of Pile A, E, and F was 1.73, 1.64, and 1.87 for the AASHTO LRFD simplified method [56], method developed by Davol et al [50], and the method developed by Advanced Infrastructure Technologies respectively. This shows that coupon properties do not predict the failure of the FRP piles well. This may result from defects in the FRP shell due to manufacturing differences from flat FRP plates (such as folds in the reinforcing fabric, resin rich areas, misaligned fibers, and differences in fiber volume fraction), effects of scaling from 6.4 mm (0.25 in) to 12.7 mm (0.5 in) or 25.4 mm (1 in) thick FRP samples, or stress concentrations due to cracking and separating concrete during flexure.

The ultimate moment for hollow piles was predicted using the strength of materials relationship presented in Equation 5.1. With the average strain at failure from flexural testing (ε_{ult}), average elastic modulus from coupon testing (E), assumed depth to the neutral axis (c), and moment of inertia (I), Equation 5.1 can be solved for the ultimate moment. The elastic modulus of the FRP shell in longitudinal compression was used for this calculation, because the piles failed in compression during flexural testing.

$$\varepsilon_{ult} * E = \frac{M_{ult} * c}{I} \hspace{4cm} \text{Equation 5.1}$$

The predictions were compared with flexural test data. These results are presented in Table 5.9.

Table 5.9 Ultimate Moment Prediction of Hollow Piles

Pile ID	Type	Ultimate Moment from Flexural Test (kN-m)	Ultimate Moment Prediction (kN-m)	Percent Difference
Pile B-8PB	Driven	812	781	4.0
Pile I-8HB	Baseline	912	856	6.3
Pile J-8HB	Baseline	667	647	3.0
Average of Pile B, I, J	Various	797	761	4.6
N/A	Coupon Properties	N/A	3432	N/A

This method predicts the ultimate moment of the piles well, with a maximum percent difference of 6.3%. Differences could be due to the use of nominal dimensions or the material having slightly different elastic moduli for longitudinal and compression.

5.8.2 Bending Stiffness

Pile stiffness was calculated using load and deflection data over an approximately linear region of the load-deflection curve. The range selected for each pile type is presented in Table 5.10.

Table 5.10 Load Range for Stiffness Calculations

FRP Shell Thickness (mm)	Pile Type	Load Range (kN)	Corresponding Moment Range (kN-m)
12.7	Concrete-Filled	133 - 445	223 - 745
25.4	Concrete-Filled	133 - 445	Varies[a]
25.4	Hollow	67 – 311	112 - 521

[a] Test dimensions were changed for each test of Pile C

Linear-elastic beam equations for four point bending were used to solve for the stiffness according to Equation 5.2 and Equation 5.3. The subscript "a" denotes the load point of the pile and "mid" denotes the mid-span of the pile.

$$\Delta_{mid} = \Delta_{mid,moment} + \Delta_{mid,shear} \qquad \text{Equation 5.2}$$

$$\Delta_{a} = \Delta_{a,moment} + \Delta_{a,shear} \qquad \text{Equation 5.3}$$

If there is no shear in the constant moment region between the load point and the mid-span of the pile, then the deformation due to shear is equal at the load point and the mid-span. This is expressed in Equation 5.4.

$$\Delta_{mid} - \Delta_{a} = \Delta_{mid,moment} - \Delta_{a,moment} \qquad \text{Equation 5.4}$$

With moment (m), deflections (Δ), span length (l), and distance from support to load point (a) known, Equation 5.7 can be solved for the pile stiffness (EI) by substituting Equation 5.5 and Equation 5.6 into Equation 5.4.

$$\Delta_{mid,moment} = \frac{M}{24EI}(3l^2 - 4a^2)$$ Equation 5.5

$$\Delta_{a,moment} = \frac{M}{6EI}(3la - 4a^2)$$ Equation 5.6

$$\Delta_{mid} - \Delta_a = \frac{M}{24EI}(3l^2 - 4a^2) - \frac{M}{6EI}(3la - 4a^2)$$ Equation 5.7

Pile curvature was calculated by fitting a straight line through each set of 3 longitudinal strain gages on the pile. When a gage failed prematurely, a straight line was fit through the remaining strain gages. The gages were assumed to be located exactly at the ultimate tension fiber, mid-height of the cross section, and ultimate compression and no rotation about the longitudinal axis of the pile occurred during testing. Stiffness was calculated by using the curvature over the same load range to validate stiffness found using linear-elastic beam equations. A summary of pile stiffness values can be seen in Table 5.11.

Table 5.11 Bending Stiffness of FRP Piles

Pile ID	Type	EI from Moment-Curvature (kN-m^2)	EI from Beam Deflection Eqn. (kN-m^2)	Percent Difference
Pile I-8HB	Baseline	5.07E+04	No Data	No Data
Pile J-8HB	Baseline	5.04E+04	4.44E+04	11.8
Pile B-8PB	Driven	4.95E+04	4.64E+04	6.3
Pile G-4FB	Baseline	3.44E+04	3.32E+04	3.5
Pile H-4FB	Baseline	3.64E+04	No Data	No Data
Pile A-4FB	Driven	No Data		
Pile E-4FB	Load-Cycled	4.61E+04	4.36E+04	5.4
Pile F-4FB	Load-Cycled	4.47E+04	4.13E+04	7.7
Pile C-8HFB Test 1	Driven	7.56E+04	7.37E+04	2.6
Pile C-8HFB Test 2	Driven	5.95E+04	5.65E+04	4.9
Pile C-8HFB Test 3	Driven	6.16E+04	5.85E+04	5.1

Testing did not show a change in stiffness when piles were subjected to driving or cyclic loading. The stiffness calculated from the moment-curvature relationship of the driven hollow pile (Pile B) was reduced by 2.1%, when compared to baseline piles, which is believed to be within the error of the test. The concrete-filled piles had more variation in stiffness, with load-cycled piles showing stiffness values 28.2% higher than baseline piles.

Filling hollow piles (8 layers of reinforcement) with concrete appears to increase the stiffness by 22.7% when comparing all hollow piles to Pile C Test 3, while increasing the moment at failure by 191%. Concrete-filled piles with 8 layers of reinforcement showed a stiffness 52.5% greater than concrete-filled piles with 4 layers of reinforcement. The concrete-filled piles with 8 layers of reinforcement also had an ultimate moment 99.8% higher than concrete-filled piles with 4 layers of reinforcement. It appears that adding reinforcement to the FRP shell creates a larger increase in pile stiffness due to cracking of the concrete, but filling piles with concrete has a larger influence on the ultimate moment capacity of the pile by changing the failure mode from compression to tension.

Stiffness was also calculated using moment and deflection in 2.71 kN-m (2 kip-ft) increments with linear-elastic beam equations. Concrete-filled piles were assumed to behave linearly over a small increment of moment. This method was used to show degradation in stiffness over the duration of the test. The degradation in stiffness can be seen in Figure 5.42. These plots include stiffness data that was calculated at the loading point and the mid-span of the pile. Concrete-filled piles exhibited an initial decrease in stiffness up to an approximate moment of 100 kN-m (74 kip-ft).
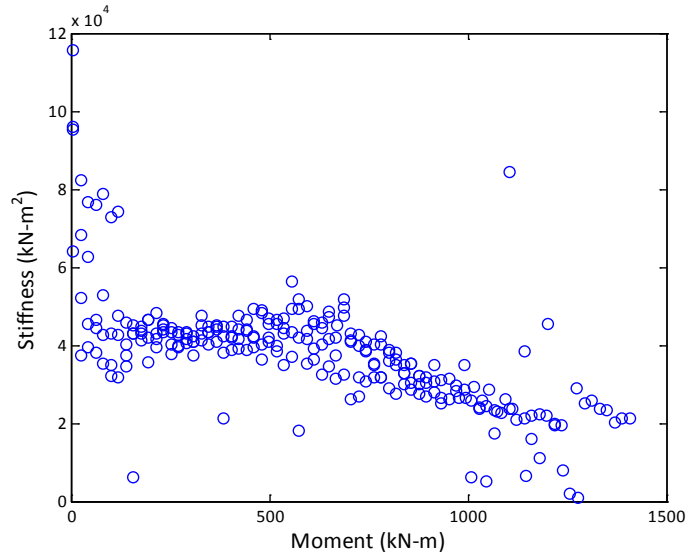
Figure 5.42 Decrease in Stiffness during Flexural Testing of Concrete-Filled Piles

Bending stiffness was calculated for hollow piles using the elastic modulus from coupon testing and moment of inertia calculated using nominal dimensions. This was compared to the bending stiffness found using the moment curvature relationship found during flexural testing. This can be seen in Table 5.12.

Table 5.12 Bending Stiffness Prediction for Hollow Piles

Pile ID	Type	EI from Moment-Curvature (kN-m^2)	EI from Coupon Properties (kN-m^2)	Percent Difference
Pile I-8HB	Baseline	5.07E+04	4.72E+04	6.9
Pile J-8HB	Baseline	5.04E+04	4.72E+04	6.3
Pile B-8PB	Driven	4.95E+04	4.72E+04	4.6

Coupon properties predicted the stiffness of hollow piles well, with a maximum percent difference of 6.9%.

102

5.8.3 Hollow Pile Predictions

The deflections and rotations of hollow piles were compared to predictions made using linear-elastic beam equations. Deflections at the mid-span and loading point were calculated using Equation 5.5 and Equation 5.6 respectively. Rotation at the supports was calculated using the principle of virtual work. These comparisons are presented in Table 5.13.

Table 5.13 Predicted Deflections and Rotations of Hollow Piles in Flexure

Pile ID	Deflection at Loading Point		Deflection at Mid-span		Rotation at Support	
	Measured (mm)	Predicted (mm)	Measured (mm)	Predicted (mm)	Measured (deg.)	Predicted (deg.)
Pile I	190	205	186	236	3.70	3.68
Pile J	140	150	161	172	2.19	2.78
Pile B	177	182	204	210	2.85	3.48

These equations over-predicted the deflections in all cases, with a percent difference ranging from 2.8% to 7.9%. This range ignored the mid-span deflection of Pile I, which was less than the deflection at the loading point and is considered invalid. The principle of virtual work did not predict the rotations as closely. This ranged from under-predicting rotations by 0.5% to over-predicting them by 26.9%.

CHAPTER 6 RESIDUAL PROPERTIES OF DRIVEN FRP PILES TESTED IN AXIAL COMPRESSION

6.1 Axial Compression Test

6.1.1 General Test Configuration

Axial compression samples were loaded under a test frame with 4 concentric hydraulic cylinders. Load was distributed over the top of the pile section using a 76.2 mm (3 in) thick steel plate and at the bottom using a 50.8 mm (2 in) thick steel plate supporting a larger 25.4 mm (1 in) thick steel plate that was used to move samples in and out of the frame. The test configuration can be seen in Figure 6.1.

Figure 6.1 Axial Compression Test Configuration

Pile sections were proof loaded to 4450 kN (1000 kips) using 4 double acting

1330 kN (300 kip) Enerpac RR1502 hydraulic cylinders powered by a 68.9 MPa (10 ksi)

Enerpac ZU4 Series hydraulic pump. The cylinders and pump can be seen in Figure 6.2.

(a)   (b)

Figure 6.2 150 Ton Enerpac Cylinders (a) and Hydraulic Pump (b)

6.1.2 Instrumentation

Pile sections were instrumented with 3 longitudinal strain gages placed at the mid-

height of the sample. Longitudinal gages were placed at intervals of 120 degrees around

the circumference of the sample. Hoop strains were measured by 1 strain gage at the mid-

height of the pile section and 1 strain gage located 0.38 m (1.25 ft), 1/4 of the sample

height, from the top of the pile section. Deflections were measured using 2 string

potentiometers which were attached to the 76.2 mm (3 in) steel loading plate. A sketch of

the instrumentation can be seen in Figure 6.3
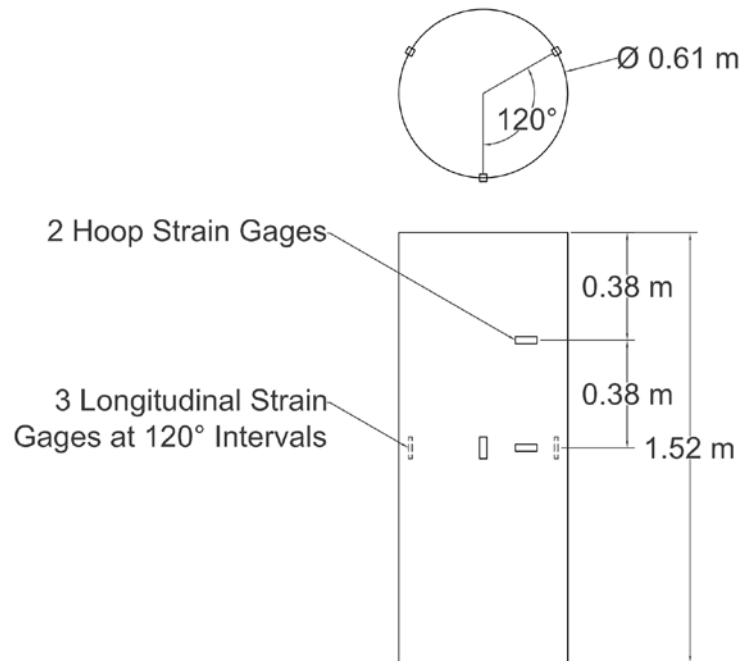
Figure 6.3 Instrumentation for Axial Compression Testing

6.1.3 Loading

Pile sections were manually loaded using increments of 10.3 MPa (1500 psi) of hydraulic pressure to 51.7 MPa (7500 psi), and then loaded to 55.2 MPa (8000 psi) and 60.0 MPa (8700 psi). Pressure readings were taken from a calibrated dial gauge, as pictured in Figure 6.4, and matched to strain and deflection data using timestamps. The load was held for 5 seconds at each pressure increment to correlate data acquisition.

Figure 6.4 Dial Gauge Used for Pressure Readings

Some error may be introduced into the data due to the manual loading of the pile sections. The dial gage used to monitor hydraulic pressure had a resolution of 689 kPa (100 psi). Pressure readings are believed to be within +/- 345 kPa (50 psi) which is equivalent to +/- 27.1 kN (6.1 kips). A maximum hydraulic pressure of 60.0 MPa (8700 psi), which is an equivalent load of 4750 kN (1068 kips), was selected to ensure all pile sections exceeded the proof load of 4450 kN (1000 kips).

6.2 Description of Piles

Fiber reinforced polymer (FRP) piles were tested as hollow and concrete-filled samples, with each of these pile types having driven and undriven samples. All piles were cut into 3 axial compression samples measuring nominally 1.52 m (5 ft) in height. Hollow piles had a 25.4 mm (1 in) thick FRP shell, while concrete-filled piles had a 12.7 mm (0.5 in) FRP shell. A summary of the axial compression samples is presented in Table 6.1.

Table 6.1 Summary of Piles Tested in Axial Compression

Letter Designation	Number of Plys in Shell	Type of Concrete	Pile ID	Type	Delivered Length (m)
A	4	F	Pile A-4FB	Driven	12.3
D	8	H	Pile D-8HA	Driven	10.5
K	8	H	Pile K-8HA	Baseline	6.1
L	4	F	Pile L-4FA	Baseline	6.1

6.3 Axial Compression Test Results

6.3.1 Hollow Piles

All hollow piles achieved the proof load of 4450 kN (1000 kips) without failing. The results of baseline and driven hollow piles can be seen in Table 6.2 and Table 6.3 respectively. Poisson's ratio calculations for Pile D Specimen 3 were not considered reliable due to irregular strain gage data in the hoop direction.

Table 6.2 Longitudinal Modulus and Poisson's Ratio of Baseline Hollow Piles

Test	Longitudinal Modulus (GPa)	Poisson's Ratio
Pile K Specimen 1	26.8	0.35
Pile K Specimen 2	26.8	0.33
Pile K Specimen 3	26.3	0.39
Pile K All Data	26.6	0.36

Table 6.3 Longitudinal Modulus and Poisson's Ratio of Driven Hollow Piles

Test	Longitudinal Modulus (GPa)	Poisson's Ratio
Pile D Specimen 1	26.3	0.38
Pile D Specimen 2	25.9	0.37
Pile D Specimen 3	27.4	No Data
Pile D All Data	26.5	0.38

Deflection, longitudinal strain, and hoop strain during axial compression testing are presented in Figure 6.5, Figure 6.6, and Figure 6.7 respectively. Load was converted to stress using nominal dimensions of the piles and is presented as an applied apparent

108

stress. This applied apparent stress was used in calculations of longitudinal modulus for

hollow piles.
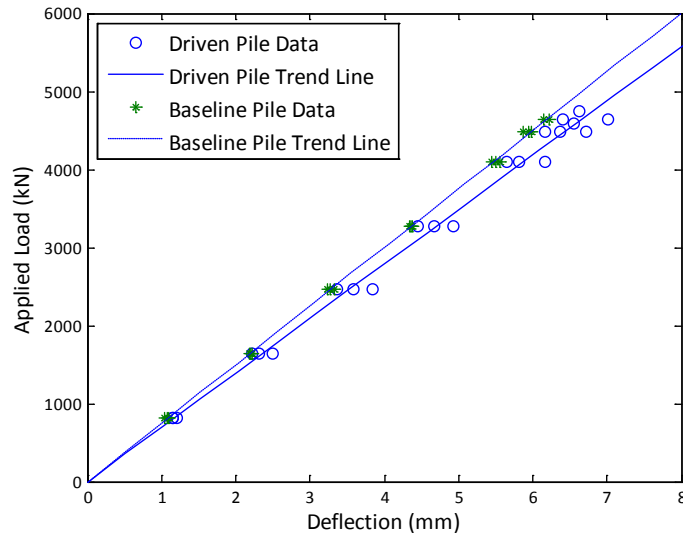
Figure 6.5 Deflection during Axial Compression of Hollow Piles
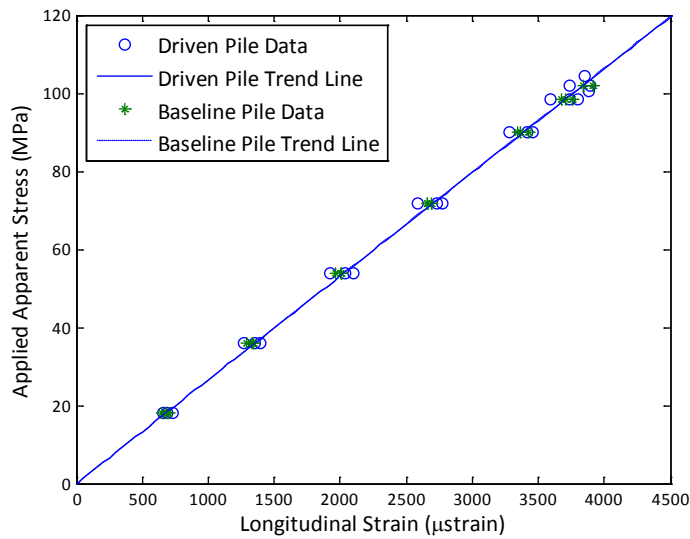
Figure 6.6 Longitudinal Strain during Axial Compression of Hollow Piles
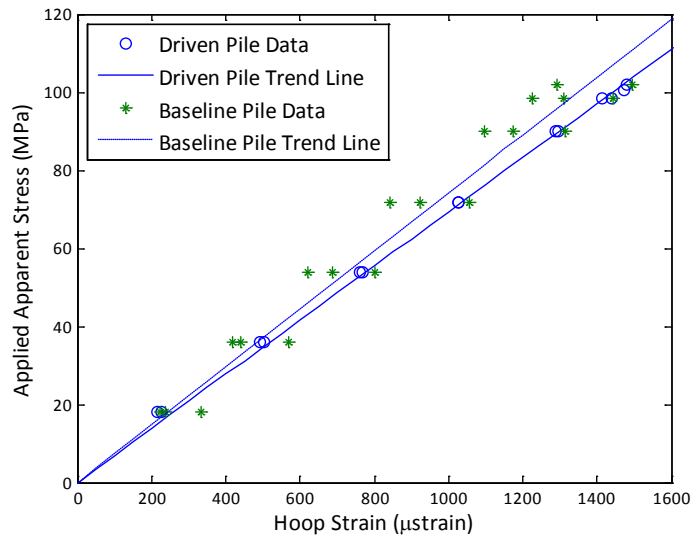
Figure 6.7 Hoop Strain during Axial Compression of Hollow Piles

6.3.2 Concrete-Filled Piles

All concrete-filled piles achieved the proof load of 4450 kN (1000 kips) without failing. The third specimen cut from Pile A was not tested, because the ends did not meet the squareness specification of 1.59 mm (1/16 in) across the pile diameter. The results of baseline and driven concrete-filled piles can be seen in Table 6.4 and Table 6.5 respectively. Poisson's ratio is not presented because calculations were considered unreliable for a concrete-filled pile.

Table 6.4 Apparent Longitudinal Modulus
of Baseline Concrete-Filled Piles

Test	Apparent Longitudinal Modulus (GPa)
Pile L Specimen 1	19.9
Pile L Specimen 2	23.0
Pile L Specimen 3	21.3
Pile L All Data	21.2

Table 6.5 Apparent Longitudinal Modulus
of Driven Concrete-Filled Piles

Test	Apparent Longitudinal Modulus (GPa)
Pile A Specimen 1	23.9
Pile A Specimen 2	28.9
Pile A All Data	25.9

Deflection, longitudinal strain, and hoop strain during axial compression testing are presented in Figure 6.8, Figure 6.9, and Figure 6.10 respectively. Load was converted to stress using nominal dimensions of the piles and is presented as an applied apparent stress. This applied apparent stress was used in calculations of apparent longitudinal modulus for concrete-filled piles.
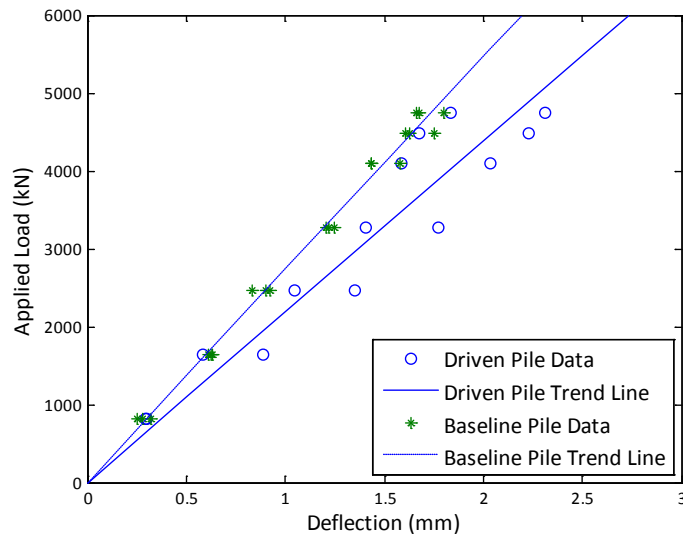
Figure 6.8 Deflection during Axial Compression of Concrete-Filled Piles
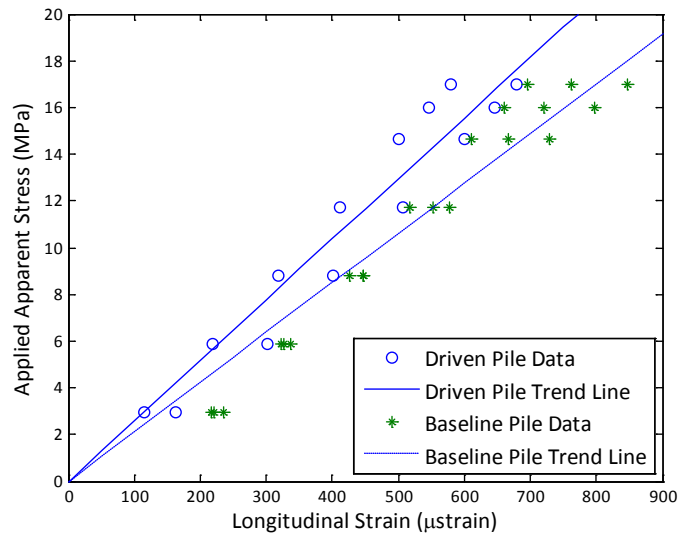
Figure 6.9 Longitudinal Strain during Axial Compression of Concrete-Filled Piles
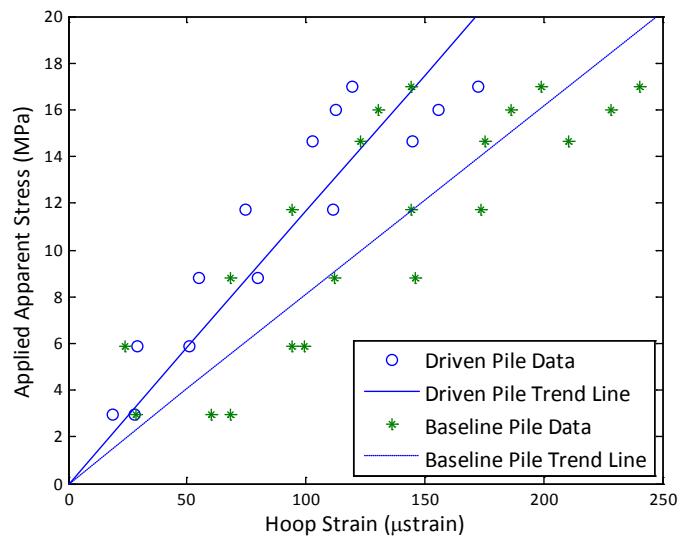
Figure 6.10 Hoop Strain during Axial Compression of Concrete-Filled Piles

Differences in concrete are believed to have caused the driven concrete-filled piles to be stiffer than baseline piles. Concrete for driven piles was provided by Auburn Concrete, and concrete for baseline piles was provided by Owen J Folsom Inc. Both concrete mixes were proportioned to meet specifications for MaineDOT Class A concrete

with a target 28 day compressive strength of 30 MPa (4350 psi), but the amount of cure

time was 6.5 times higher for the driven pile samples. A summary of concrete properties

for axial compression testing can be seen in Table 6.6.

Table 6.6 Concrete Properties for Axial Compression Testing

	Baseline Piles	Driven Piles
Cure Time at Cylinder Test (Days)	35	12
f'$_c$ of Cylinders (MPa)	33.2	32.3
f'c Corrected to 28 Days (MPa)	32.0	38.2
Cure Time at Axial Pile Compression Test (Days)	39	253
f'$_c$ Corrected to Axial Pile Test Date (MPa)	33.6	44.1

Concrete cylinder strengths were converted to 28 day strength and strength at the

time of axial testing using Equation 6.1 [57]. It should be noted that this correlation was

developed for concrete using Type I cement and moist-cured at 21 °C (70 °F).

$$f'_{c(t)} = f'_{c(28)} \left(\frac{t}{4 + 0.85 * t} \right)$$
<div align="right">Equation 6.1</div>

6.3.3 Discussion of Axial Compression Test Results

All FRP pile sections, hollow and concrete-filled, achieved the proof load of 4450

kN (1000 kip). A summary of axial compression testing properties can be seen in Table

6.7. The longitudinal modulus of hollow piles compares well with the elastic modulus

found in coupon level testing. The modulus of compressive coupons was found to be 25.3

GPa (3670 ksi). The differences between these two moduli may be due to the scale of the

test, use of nominal dimensions, or strain range of the test. Hollow pile sections tested in axial compression were evaluated over a strain range of approximately 0 to 4,000 microstrain, while compression coupons were evaluated from 3,000 to 10,000 microstrain. The modulus of elasticity for compressive coupons is 28.4 GPa (4120 ksi), when calculated from 0 to 4,000 microstrain.

Table 6.7 Properties of FRP Pile Sections in Axial Compression

Pile Type	Condition	Longitudinal Modulus (GPa)	Apparent Longitudinal Modulus (GPa)	Poisson's Ratio
Hollow Piles	Baseline	26.6	—	0.36
	Driven	26.5	—	0.38
Concrete-Filled Piles	Baseline	—	21.2	—
	Driven	—	25.9	—

CHAPTER 7 DURABILITY PROPERTIES OF FRP PILES

7.1 Literature Review

Chin et al [58] investigated changes in tensile properties and glass transition temperature of vinyl ester and polyester resin castings that were exposed to ultraviolet (UV) radiation, moisture, alkaline, and saline environments. Chin et al [59] did not note any significant changes in the loss modulus or storage modulus during glass transition temperature testing of conditioned samples. Tensile testing did not yield any definitive trends either, as the samples with reduced strength had a large scatter of tensile capacities.

Guzman and Brøndsted [60] researched the effects of salt water immersion on glass FRP samples. Longitudinal tension samples with multi-directional reinforcement lost 24% of their strength and approximately 22% of their strain at failure after being conditioned for 8 years. However, the modulus of the samples was only reduced by 7%.

Hongwang and Huang [61] tested glass and polyester composite materials exposed to UV radiation. This program examined the flexural deformation and tensile strength of the material after exposure ranging from 30 to 210 days. The flexural deformation under 0.2 N (0.05 lbs) increased 87.4% after 210 days of exposure. The tensile strength decreased 5.3% after 210 days of exposure. Hongwang and Huang [61] attribute these trends to thermo-oxidation, photodegradtion, and a loss of bond between the fibers and matrix.

Pando et al [62] examined the effects of submerging circular FRP shells in fresh water. This test program evaluated properties as a function of time and moisture content. The results of testing were used to create a simplified model of the long-term structural capacity of FRP piles. The model showed a loss of 5% in the axial direction and 24% in flexural.

Shokrieh and Bayat [63] tested tension, compression, and shear samples exposed to 3, 6, and 12 months of simulated UV exposure using a UV chamber. These samples were constructed with a thickness of 1 mm (0.039 in) for tensile tests and 3 mm (0.12 in) for compressive tests, using glass fibers and an unsaturated polyester resin. Samples lost 38.4% of their tensile strength, 18.8% of their shear strength, and 3.8% of their compressive strength after 100 hours of accelerated UV exposure.

Afshar et al [64] examined the effects of UV radiation and moisture absorption on the flexural properties of carbon fiber and vinylester composites used in the marine industry. This study found that vinylester composites experience degradation at their exposed surface, with the reduction of flexural properties being most notable in the transverse direction. Afshar et al [64] note that the flexural testing of environmentally conditioned gives a larger decrease in mechanical properties because surface damage is aligned with the extreme tension and/or compression fiber. This effect would not be seen in tensile testing. It was found that longitudinal and transverse flexural strength was decreased by 10% and 40% respectively.

7.2 AASHTO Requirements

Fiber reinforced polymer (FRP) samples were tested according to Section 2.2.4.4 of the American Association of State Highway and Transportation Officials (AASHTO) Guide Specifications for Design of Bonded FRP Systems for Repair and Strengthening of Concrete Bridge Elements [1]. This specifies that samples must retain 85% of the ultimate tensile strain and glass transition temperature after the following environmental conditioning:

- "Water – Samples shall be immersed in distilled water having a temperature of 100 +/- 3°F (38 +/- 2°C) and tested after 1,000, 3,000, and 10,000 hours of exposure.

- Alternating Ultraviolet Light and Condensation Humidity – Samples shall be conditioned in an apparatus under Cycle 1-UV exposure condition according to American Society for Testing and Materials (ASTM) G154 Standard Practice. Samples shall be tested within two hours after removal from the apparatus.

- Alkali – The sample shall be immersed in a saturated solution of calcium hydroxide (pH ~11) at ambient temperature of 73 +/- 3 °F (23 +/- 2°C) for 1,000, 3,000, and 10,000 hours prior to testing. The pH level shall be monitored and the solution shall be maintained as needed.

- Freeze-Thaw – Composite samples shall be exposed to 100 repeated freezing and thawing in an apparatus meeting the requirements of ASTM C666."

7.3 Testing Program

FRP panels measuring nominally 533 mm (21 in) by 356 mm (14 in) were cut

from the same FRP plates used for mechanical property testing. The edges of these panels

were sealed with Derakane 8084, an epoxy vinyl ester resin meeting the durability

requirements set by AASHTO, to limit the penetration of moisture at the edges. The

dimensions of the panels provided 51 mm (2 in) of extra material at the edge of the panel

to further limit the effects of moisture penetration at the edges of the panels. This can be

seen in Figure 7.1.

(a)   (b)
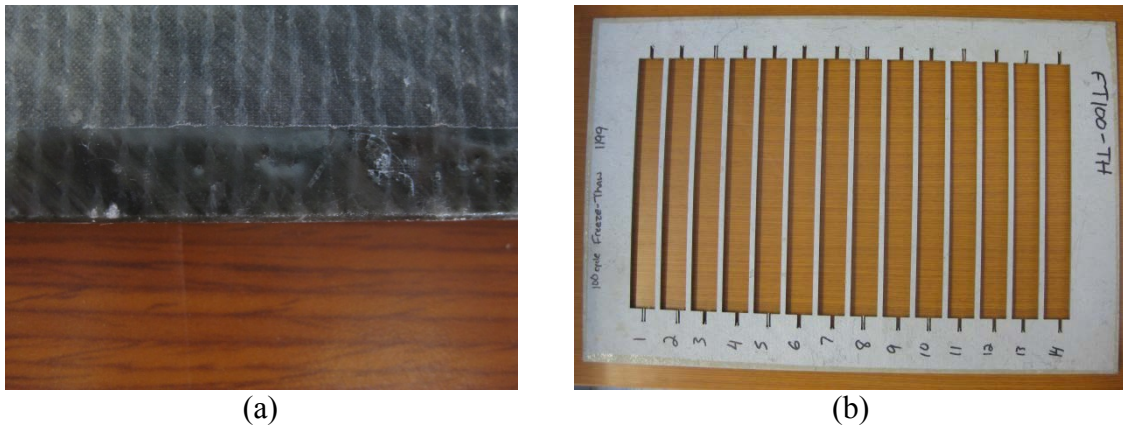
Figure 7.1 Sealed Edges (a) and Edge Distance (b) on FRP Panels for Conditioning

These panels were conditioned according to the environmental exposure

conditions set by AASHTO. When duration of the exposure condition was completed, the

plates were stored at 23 °C (73 °F) and 50% relative humidity until they could be tested.

7.3.1 Alkali Environment

Samples were conditioned in containers of an alkali solution comprised of

distilled water and calcium hydroxide with a target pH of 11 and temperature of 23 °C

(73 °F). Samples were conditioned in a Parameter Generation and Control model 3478-

4-W environmental chamber for exposure times of 1,000 hours, 3,000 hours, and 10,000 hours. This can be seen in Figure 7.2. Temperature, water level, and pH were monitored and adjusted as necessary throughout the exposure time.

Figure 7.2 Alkali Exposure Test

The results of tension tests on samples conditioned in an alkali solution can be seen in Table 7.1 and Table 7.2 for longitudinal and hoop tension respectively.

Table 7.1 Longitudinal Tension Properties of Alkali Exposure Samples

Conditioning	Statistic	Ultimate Stress in X (MPa)	Ultimate Strain in X (µstrain)	Modulus of Elasticity in X (GPa)	Poisson's Ratio
1,000 Hour Alkali Exposure	Mean	497	2.34E+04	23.4	0.37
	Std Dev	35	1.92E+03	0.3	0.01
	COV	7.0%	8.2%	1.4%	3.1%
3,000 Hour Alkali Exposure	Mean	491	2.21E+04	24.0	0.35
	Std Dev	16	1.29E+03	0.3	0.01
	COV	3.2%	5.8%	1.3%	1.4%
10,000 Hour Alkali Exposure	Mean	474	2.13E+04	23.7	0.35
	Std Dev	11	4.68E+02	0.3	0.01
	COV	2.4%	2.2%	1.4%	3.0%

Table 7.2 Hoop Tension Properties of Alkali Exposure Samples

Conditioning	Statistic	Ultimate Stress in Y (MPa)	Ultimate Strain in Y (µstrain)	Modulus of Elasticity in Y (GPa)	Poisson's Ratio
1,000 Hour Alkali Exposure	Mean	159	1.80E+04	16.1	0.33
	Std Dev	7	8.68E+02	0.7	0.05
	COV	4.2%	4.8%	4.2%	13.5%
3,000 Hour Alkali Exposure	Mean	174	1.95E+04	13.7	0.33
	Std Dev	6	6.77E+02	1.4	0.02
	COV	3.5%	3.5%	10.4%	5.8%
10,000 Hour Alkali Exposure	Mean	175	1.99E+04	15.3	0.34
	Std Dev	9	1.04E+03	1.1	0.02
	COV	5.3%	5.2%	7.0%	4.5%

Table 7.3 Glass Transition Properties of Alkali Exposure Samples

Conditioning	Onset of Change in Slope of Storage Modulus (°C)	Peak of Loss Modulus (°C)	Peak of Tan Delta (°C)
1,000 Hour Alkali Exposure	84.2	94.2	115.3
3,000 Hour Alkali Exposure	85.4	98.9	114.4
10,000 Hour Alkali Exposure	97.2	106.9	121.6

7.3.2 Moisture Absorption

Samples were conditioned in a bath of distilled water with a target temperature of 38 °C (100 °F). Containers of water were placed in a VWR Scientific HAFO 1600 Series oven for exposure times of 1,000 hours, 3,000 hours, and 10,000 hours. This can be seen in Figure 7.3. Water levels and temperature were monitored and adjusted as necessary throughout the exposure time.

Figure 7.3 Water Exposure Test

The results of tension tests on samples conditioned in a water bath can be seen in Table 7.4 and Table 7.5 for longitudinal and hoop tension respectively.

Table 7.4 Longitudinal Tension Properties of Water Exposure Samples

Conditioning	Statistic	Ultimate Stress in X (MPa)	Ultimate Strain in X (μstrain)	Modulus of Elasticity in X (GPa)	Poisson's Ratio
1,000 Hour Water Exposure	Mean	498	2.46E+04	22.1	0.32
	Std Dev	16	1.33E+03	0.4	0.01
	COV	3.3%	5.4%	1.6%	1.7%
3,000 Hour Water Exposure	Mean	461	1.97E+04	24.2	0.34
	Std Dev	25	1.40E+03	0.4	0.01
	COV	5.4%	7.1%	1.5%	2.7%
10,000 Hour Water Exposure	Mean	441	1.96E+04	23.6	0.35
	Std Dev	14	6.89E+02	0.4	0.01
	COV	3.2%	3.5%	1.8%	1.9%

Table 7.5 Hoop Tension Properties of Water Exposure Samples

Conditioning	Statistic	Ultimate Stress in Y (MPa)	Ultimate Strain in Y (µstrain)	Modulus of Elasticity in Y (GPa)	Poisson's Ratio
1,000 Hour Water Exposure	Mean	170	2.20E+04	13.1	0.13
	Std Dev	2	9.53E+02	1.7	0.04
	COV	1.1%	4.3%	13.1%	27.0%
3,000 Hour Water Exposure	Mean	144	1.69E+04	13.4	0.34
	Std Dev	9	1.24E+03	1.3	0.02
	COV	6.1%	7.3%	10.0%	4.5%
10,000 Hour Water Exposure	Mean	173	2.07E+04	14.2	0.14
	Std Dev	6	1.49E+03	0.3	0.01
	COV	3.7%	7.2%	1.9%	10.3%

Table 7.6 Glass Transition Properties of Water Exposure Samples

Conditioning	Onset of Change in Slope of Storage Modulus (°C)	Peak of Loss Modulus (°C)	Peak of Tan Delta (°C)
1,000 Hour Water Exposure	85.2	96.4	113.8
3,000 Hour Water Exposure	80.0	90.5	105.5
10,000 Hour Water Exposure	92.9	106.8	121.2

7.3.3 UV and Condensation Humidity

Ultraviolet (UV)/condensation humidity testing was conducted in accordance with ASTM G154 [65] using a UVA-340 ultraviolet lamp at an irradiance of 0.89 W/m^2/nm. Neither the ASTM standard or AASHTO [1] specified a duration for this exposure type, so an exposure time of 1,000 hours was selected. A typical cycle for UV/Condensation Humidity can be seen in Table 7.7.

Table 7.7 Typical UV/Condensation Humidity Test Cycle

Cycle	Step	Duration	Type	Temp. (°C)
1	1	8 hours	UV	60
	2	4 hours	Condensation	50

Samples were placed in a Q-Panel Lab Products QUV/spray test chamber for the specified exposure time. This can be seen in Figure 7.4. The FRP panels have a coating to limit degradation due to ultraviolet light. When panels were placed in the conditioning chamber, the coating was placed on the side of the chamber with the UV lamps to mimic the orientation of the coating on the outside of the full scale FRP piles.

Figure 7.4 UV/Condensation Humidity Test Chamber

The results of tension tests on samples conditioned in the ultraviolet light and condensation humidity chamber can be seen in Table 7.8 and Table 7.9 for longitudinal and hoop tension respectively.

Table 7.8 Longitudinal Tension Properties of UV/Condensation Humidity Samples

Conditioning	Statistic	Ultimate Stress in X (MPa)	Ultimate Strain in X (µstrain)	Modulus of Elasticity in X (GPa)	Poisson's Ratio
1,000 Hour Exposure	Mean	534	2.34E+04	24.0	0.32
	Std Dev	14	1.83E+03	0.5	0.01
	COV	2.6%	7.8%	2.1%	3.0%

Table 7.9 Hoop Tension Properties of UV/Condensation Humidity Samples

Conditioning	Statistic	Ultimate Stress in Y (MPa)	Ultimate Strain in Y (µstrain)	Modulus of Elasticity in Y (GPa)	Poisson's Ratio
1,000 Hour Exposure	Mean	169	2.04E+04	14.0	0.12
	Std Dev	11	1.61E+03	0.5	0.02
	COV	6.4%	7.9%	3.8%	17.9%

Table 7.10 Glass Transition Properties of UV/Condensation Humidity Samples

Conditioning	Onset of Change in Slope of Storage Modulus (°C)	Peak of Loss Modulus (°C)	Peak of Tan Delta (°C)
1,000 Hour Exposure	92.6	113.9	128.8

7.3.4 Freeze-Thaw

Freeze-thaw testing was conducted in general accordance with ASTM C666 [66].

Samples were subjected to 100 cycles of freezing at -18 °C (0 °F) and thawing at 4 °C

(40 °F). The standard specifies that that samples be "surrounded by not less than 1/32 in

[1 mm] nor more than 1/8 in [3 mm] of water at all times" or "completely surrounded by

air during the freezing phase of the cycle and by water during the thawing phase." The

samples in this test were subjected to a target relative humidity of 100% during the

thawing phase and 0% during the freezing phase. A typical cycle of this test is presented

in Table 7.11.

Table 7.11 Typical Cycle of Freeze-Thaw Exposure

Cycle	Step	Duration	Initial Temp. (°F)	Final Temp. (°F)	Relative Humidity (%)
1	1	3 Hours	40	40	100
	2	10 Minutes	40	0	0
	3	3 Hours	0	0	0
	4	15 Minutes	0	40	0

Samples were placed on 25.4 mm (1 in) spacers inside an ESPEC ESL-3CA

freeze-thaw chamber to allow air to circulate evenly over the plates. The freeze-thaw

chamber and sample configuration can be seen in Figure 7.5.

(a)   (b)
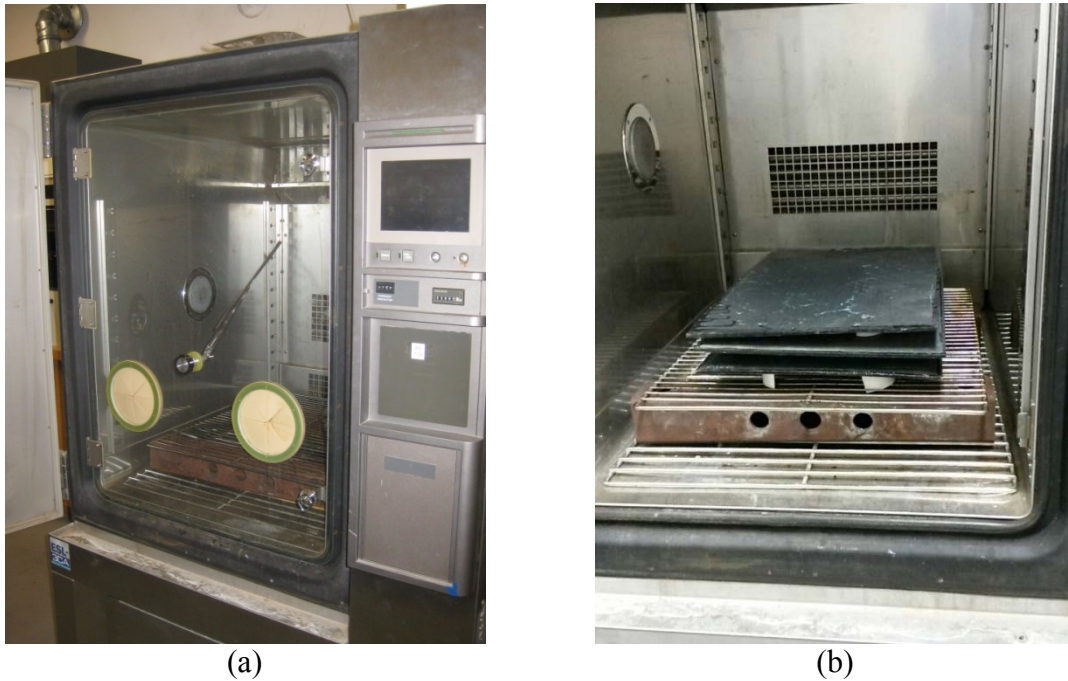
Figure 7.5 Freeze-Thaw Chamber (a) and Sample Configuration (b)

The results of tension tests on samples conditioned in a freeze-thaw chamber can

be seen in Table 7.12 and Table 7.13 for longitudinal and hoop tension respectively.

Table 7.12 Longitudinal Tension Properties of Freeze-Thaw Samples

Conditioning	Statistic	Ultimate Stress in X (MPa)	Ultimate Strain in X (μstrain)	Modulus of Elasticity in X (GPa)	Poisson's Ratio
100 Freeze-Thaw Cycles	Mean	411	1.88E+04	23.1	0.35
	Std Dev	23	1.72E+03	0.4	0.01
	COV	5.6%	9.1%	1.7%	1.9%

Table 7.13 Hoop Tension Properties of Freeze-Thaw Samples

Conditioning	Statistic	Ultimate Stress in Y (MPa)	Ultimate Strain in Y (μstrain)	Modulus of Elasticity in Y (GPa)	Poisson's Ratio
100 Freeze-Thaw Cycles	Mean	175	2.11E+04	14.4	0.14
	Std Dev	10	1.39E+03	0.5	0.02
	COV	5.6%	6.6%	3.6%	12.0%

Table 7.14 Glass Transition Properties of Freeze-Thaw Samples

Conditioning	Onset of Change in Slope of Storage Modulus (°C)	Peak of Loss Modulus (°C)	Peak of Tan Delta (°C)
100 Freeze-Thaw Cycles	92.6	103.5	119.2

7.4 Discussion of Durability Properties of FRP Plates

The FRP samples for this test program did not meet the AASHTO requirement for 85% retention of ultimate tensile strain after conditioning, with tension coupons losing up to 26.4% of their baseline value. The change in properties for ultimate strain, ultimate stress, and modulus of elasticity can be seen in Table 7.15 and Table 7.16 for longitudinal and hoop tension respectively. Changes in glass transition properties can be seen in Table 7.17. Negative percent lost denotes an increase in the material property.

Table 7.15 Change in Material Properties of Longitudinal Tension Samples after
Environmental Conditioning

Conditioning	Ultimate Strain in X (μstrain)	Percent Lost	Ultimate Stress in X (MPa)	Percent Lost	Modulus of Elasticity (GPa)	Percent Lost
Baseline	2.56E+04	—	530	—	22.5	—
1,000 Hour Alkali	2.34E+04	8.5	497	6.3	23.4	-4.0
3,000 Hour Alkali	2.21E+04	13.6	491	7.4	24.0	-6.8
10,000 Hour Alkali	2.13E+04	**16.9**	474	10.5	23.7	-5.1
1,000 Hour Water	2.46E+04	4.0	498	6.1	22.1	2.0
3,000 Hour Water	1.97E+04	**23.2**	461	13.1	24.2	-7.5
10,000 Hour Water	1.96E+04	**23.5**	441	**16.8**	23.6	-4.9
100 Freeze-Thaw Cycles	1.88E+04	**26.4**	411	**22.5**	23.1	-2.6
1,000 Hour UV and Condensation	2.34E+04	8.3	534	-0.6	24.0	-6.7

Table 7.16 Change in Material Properties of Hoop Tension Samples after Environmental Conditioning

Conditioning	Ultimate Strain in Y (µstrain)	Percent Lost	Ultimate Stress in Y (MPa)	Percent Lost	Modulus of Elasticity (GPa)	Percent Lost
Baseline	2.27E+04	—	174	—	13.7	—
1,000 Hour Alkali	1.80E+04	**20.7**	159	9.0	16.1	-18.1
3,000 Hour Alkali	1.95E+04	14.3	174	0.3	13.7	-0.6
10,000 Hour Alkali	1.99E+04	12.5	175	-0.6	15.3	-12.2
1,000 Hour Water	2.20E+04	3.1	170	2.7	13.1	3.8
3,000 Hour Water	1.69E+04	**25.6**	144	**17.4**	13.4	1.8
10,000 Hour Water	2.07E+04	8.7	173	0.5	14.2	-3.9
100 Freeze-Thaw Cycles	2.11E+04	7.1	175	-0.5	14.4	-5.8
1,000 Hour UV and Condensation	2.04E+04	10.2	169	2.7	14.0	-2.6

Table 7.17 Change in Properties of Glass Transition Temperature Samples after
Environmental Conditioning

Conditioning	Onset of Change in Slope of Storage Modulus (°C)	Percent Lost	Peak of Loss Modulus (°C)	Percent Lost	Peak of Tan Delta (°C)	Percent Lost
Baseline	86.8	—	93.2	—	118.5	—
1,000 Hour Alkali	84.2	3.0	94.2	-1.1	115.3	2.7
3,000 Hour Alkali	85.4	1.6	98.9	-6.2	114.4	3.4
10,000 Hour Alkali	97.2	-12.0	106.9	-14.8	121.6	-2.6
1,000 Hour Water	85.2	1.8	96.4	-3.5	113.8	4.0
3,000 Hour Water	80.0	7.9	90.5	2.9	105.5	11.0
10,000 Hour Water	92.9	-7.1	106.8	-14.6	121.2	-2.2
100 Freeze-Thaw Cycles	92.6	-6.7	103.5	-11.1	119.2	-0.6
1,000 Hour UV and Condensation	96.9	-11.6	113.9	-22.3	128.8	-8.7

Tensile properties may have also been influenced by variation in the material and manufacturing defects. This is especially noticeable for the change in ultimate stress of longitudinal and hoop samples that were exposed to freeze-thaw cycles. Longitudinal tension samples lost 22.5% of their baseline ultimate stress, while hoop tension samples increased by 0.5% despite being exposed to the same conditions. Some manufacturing defects that were seen in durability samples are misaligned reinforcing fabric and warping of the FRP panels. An example of misaligned fibers can be seen in Figure 7.6. It

was only possible to see misaligned fibers in one of the two layers of reinforcement, because the opposite side of the panels was covered in a blue coating.

(a)   (b)
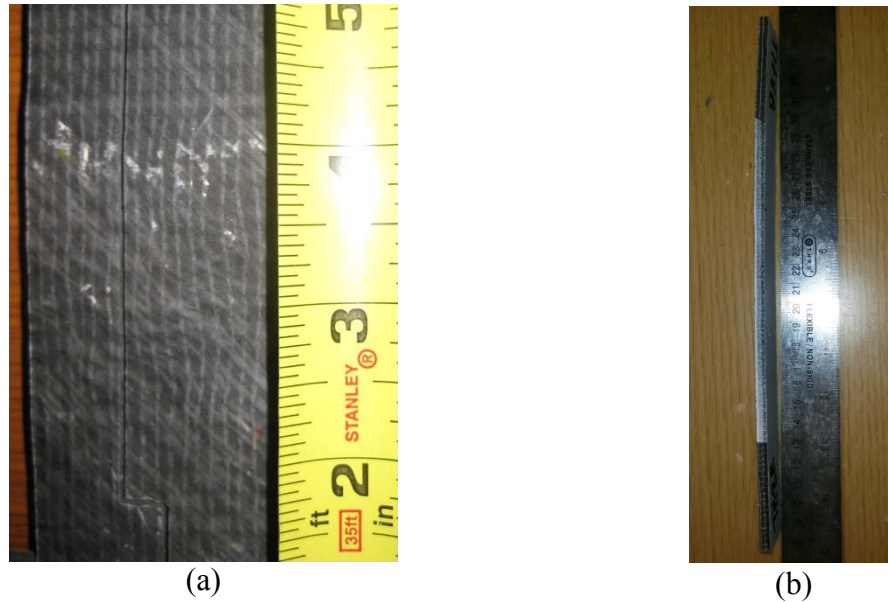
Figure 7.6 Misaligned Fibers (a) and Warping (b) in Durability Samples

Sets of unconditioned tension and glass transition temperature coupons were tested over the duration of environmental conditioning to evaluate the change in the material over time. These samples were stored indoors in a heated and cooled facility, but temperature and humidity were not monitored or maintained at a constant value. Results of these tests can be seen in Table 7.18, Table 7.19, and Table 7.20. There is no data for Baseline Set C of longitudinal tension samples because 6 out of 12 samples failed in the grips of the Instron test machine and 2 additional samples experienced an error in data acquisition.

131

Table 7.18 Change in Properties of Unconditioned Longitudinal Tension Samples

Conditioning	Ultimate Strain in X (µstrain)	Percent Lost	Ultimate Stress in X (MPa)	Percent Lost	Modulus of Elasticity (GPa)	Percent Lost
Baseline (June 2013)	2.56E+04	—	530	—	22.5	—
Baseline Set B (May 2014)	2.39E+04	6.7	516	2.7	23.7	-5.5
Baseline Set C (November 2014)	No Data		No Data		No Data	
Baseline Set D (February 2014)	2.45E+04	4.2	545	-2.7	24.0	-6.6

Table 7.19 Change in Properties of Unconditioned Hoop Tension Samples

Conditioning	Ultimate Strain in Y (µstrain)	Percent Lost	Ultimate Stress in Y (MPa)	Percent Lost	Modulus of Elasticity (GPa)	Percent Lost
Baseline (June 2013)	2.27E+04	—	174	—	13.7	—
Baseline Set B (May 2014)	2.02E+04	11.1	184	-5.4	13.3	2.8
Baseline Set C (November 2014)	1.71E+04	**24.6**	156	10.2	12.2	10.9
Baseline Set D (February 2014)	1.77E+04	**21.9**	166	4.6	15.0	-10.2

Table 7.20 Change in Properties of Unconditioned Glass Transition Temperature Samples

Conditioning	Onset of Change in Slope of Storage Modulus (°C)	Percent Lost	Peak of Loss Modulus (°C)	Percent Lost	Peak of Tan Delta (°C)	Percent Lost
Baseline (June 2013)	86.8	–	93.2	–	118.5	–
Baseline Set B (May 2014)	No Data		No Data		No Data	
Baseline Set C (November 2014)	94.6	-9.0	107.5	-15.4	112.0	-1.2
Baseline Set D (February 2014)	99.0	-14.0	106.6	-14.4	122.3	-3.2

Unconditioned sets of tensile samples also showed variation in ultimate stress and strain. Two sets of baseline hoop tension tests did not retain 85% of the baseline value found in June 2013, even though they were not exposed to environmental conditioning. This further illustrates the influence of defects on the trends in material properties after environmental exposure.

CHAPTER 8 CONCLUSIONS AND RECOMMENDATIONS FOR FUTURE WORK

Peak interface friction angles were found to be 78% of the peak angle of internal friction, with an average value of 30.8 degrees. Constant volume interface friction angles were found to 80% of the constant volume angle of internal friction, with an average value of 29.0 degrees. This is higher than values given by Naval Facilities Engineering Command [67] for steel on gravel-sand mixtures (22 degrees) and formed concrete on gravel-sand mixtures (22 to 26 degrees). This appears to be due to soil particles becoming embedded in the relatively soft FRP surface.

Hollow and concrete-filled FRP piles achieved geotechnical capacities greater than 1780 kN (400 kip) before hollow piles became visibly damaged. During the restrike, a pile helmet that provided some lateral restraint and plywood cushioning appeared to prevent the heads of hollow piles from failing at similar stresses and capacities seen during initial driving.

Hollow FRP piles examined in this program exhibited low driving stresses at failure. Pile heads failed at 11% of the coupon level compressive strength. A reduction factor of 0.10 for the ultimate driving stress of hollow piles may be appropriate for this manufacturing process and resin/reinforcement system until driving performance can be investigated further.

Toe driving appears to provide a promising solution to this problem by reducing driving stresses and converting them from compression to tension. This may change the

failure mode during driving from delamination in compression to fiber rupture in tension and allow for higher driving stresses. Full-scale tests in dense soils will need to be conducted to evaluate toe driving performance. Until this can be investigated, it seems that FRP piles should be used primarily as friction piles or driven while filled with reinforced concrete.

It may also be beneficial to use a conical pile tip. A conical tip may reduce the effects of stress concentrations when sloping bedrock or cobbles and boulders are encountered.

Both piles driven while filled with non-expansive concrete showed a loss of composite action during flexural testing. It is believed that tensile driving stresses caused the concrete to crack through the cross section. The use of expansive concrete may create a "pre-stressing" effect that would provide greater longitudinal reinforcement for the concrete. Otherwise, it may be necessary to drive concrete-filled FRP piles with longitudinal reinforcement to prevent tensile cracking during driving. If steel reinforcing bars are undesirable due to durability concerns, FRP reinforcing bars may be used. Steel reinforcing bars showed favorable performance in flexural tests conducted by Cole and Fam [51]. These FRP tubes showed higher strength and stiffness, greater ductility, and a progressive failure.

Temperatures at the pile head may need to be controlled to prevent the FRP shell from surpassing its glass transition temperature. Future studies of FRP pile driving should monitor temperatures to ensure they do not exceed the glass transition temperature and weaken the FRP shell.

The ultimate moment capacity of hollow and concrete-filled piles did not appear to be affected by driving or cyclic loading. Baseline piles created an upper and lower bound of moment capacity which bracketed all driven and load-cycled piles. Flexural testing showed a wide range of moment capacities for hollow and concrete-filled piles, so additional testing should be conducted confirm these trends. It is currently unclear whether this was caused by the small sample size and manufacturing defects or if the piles were unaffected by driving and cyclic loading.

Flexural testing did not show any significant reduction in stiffness due to driving or cyclic loading. When comparing the stiffness calculated from the moment-curvature relationship, the driven hollow pile was reduced by 2.1% and load-cycled concrete-filled piles were increased by an average of 28.2%. However, the two load-cycled piles saw 10.1% and 14.3% reduction in stiffness during cyclic loading. This reduction in stiffness was not observed when comparing their initial static test and static tests to failure.

Ultimate stresses and strains found in coupon tests did not provide an accurate prediction of the failure of FRP piles in flexure. Hollow piles failed at an average of 22% of the compressive strain seen during coupon testing. Concrete-filled piles failed at an average of 51% of the tensile strain seen during coupon testing. This may be due to the presence of defects in the FRP shell, variations in the thickness of the FRP shell, or not achieving adequate resin penetration in thicker laminates. Further testing should be conducted to quantify the frequency of occurrence and structural effects of some typical defects in FRP shell. Design reduction factors of 0.20 for compressive strength and ultimate strain and 0.40 for tensile strength and ultimate strain are deemed appropriate for this manufacturing process and resin/reinforcement and have been incorporated into

design and construction specifications for the MaineDOT. Future modifications to the manufacturing process and/or further testing may prove these values to be conservative.

Coupon properties appear to be a good predictor of stiffness properties observed in flexural testing. This may indicate that defects have a less significant effect on the prediction of stiffness compared to ultimate moment capacity.

All piles tested in axial compression achieved the proof load of 4450 kN (1000 kips). Driving did not appear to affect the longitudinal modulus of hollow FRP pile sections. The longitudinal modulus found in the hollow pile tests was comparable to the elastic modulus found during coupon testing.

FRP plates were exposed to environmental conditions outlined by AASHTO [1]. Tension samples cut from these plates did not meet the minimum requirements for retention of ultimate strain set by AASHTO. If this resin and reinforcement are used, an extended durability study should be conducted to provide appropriate environmental reduction factors to account for the performance of the piles throughout their life cycle. In order to satisfy the requirements of AASHTO, a resin with greater environmental resistance should be selected and verified through environmental conditioning.

REFERENCES

1. American Association of State Highway and Transportation Officials, *Guide Specifications for Design of Bonded FRP Systems for Repair and Strengthening of Concrete Bridge Elements*, AASHTO, Editor. 2012.

2. Pando, M.A., et al., *A Laboratory and Field Study of Composite Piles for Bridge Substructures*, F.H. Administration, Editor. 2006. p. 384.

3. Iskander, M.G. and Hassan, M., *State of the practice review in FRP composite piling.* Journal of Composites for Construction, 1998. **2**(3): p. 116-120.

4. Bakis, C.E., et al., *Fiber-Reinforced Polymer Composites for Construction - State-of-the-Art Review.* Journal of Composites for Construction, 2002. **6**(2): p. 73-87.

5. VECTORPLY Corporation, *E-QX 10200*. 2011.

6. CCP Composites, *STYPOL 040-8006 and 040-8084 Polyester Closed Molding Resins*. 2012.

7. GOM mbH, *ARAMIS v6.1.1*. 2009.

8. ASTM International, *ASTM Standard D3039-08: Standard Test Method for Tensile Properties of Polymer Matrix Composite Materials*. 2008: West Conshohocken, PA.

9. American Society for Testing and Materials, *ASTM D6641-09: Compressive Properties of Polymer Matrix Composite Materials Using a Combined Loading Compression (CLC) Test Fixture*. 2009.

10. ASTM International, *ASTM Standard D7078-12: Standard Test Method for Shear Properties of Composite Materials by V-Notched Rail Shear Method*. 2012: West Conshohocken, PA.

11. ASTM International, *ASTM Standard E1640-09: Standard Test Method for Assignment of the Glass Transition Temperature By Dynamic Mechanical Analysis*. 2009: West Conshohocken, PA.

12. Thermal Analysis Instruments, *Measurement of the Glass Transition Temperature Using Dynamic Mechanical Analysis*.

13. Terzaghi, K., Peck, R.B., and Mesri, G., *Soil Mechanics in Engineering Practice*. Third ed. 1996, New York, NY: John Wiley & Sons, Inc.

14. Atkinson, J., *The Mechanics of Soils and Foundations*. Second ed. 2010, New York, NY: Taylor and Francis.

15. Pando, M., et al. *Interface shear tests on FRP composite piles*. in *Proceedings, International Deep Foundations Congress, American Society of Civil Engineers, Orlando, Florida*. 2002.

16. Sakr, M., El Naggar, M., and Nehdi, M., *Interface characteristics and laboratory constructability tests of novel fiber-reinforced polymer/concrete piles.* Journal of Composites for Construction, 2005. **9**(3): p. 274-283.

17. Frost, J. and Han, J., *Behavior of interfaces between fiber-reinforced polymers and sands.* Journal of geotechnical and geoenvironmental engineering, 1999. **125**(8): p. 633-640.

18. Reddy, E.S., Chapman, D., and Sastry, V., *Direct shear interface test for shaft capacity of piles in sand.* Geotechnical Testing Journal, 2000. **23**(2).

19. ASTM International, *ASTM Standard D3080-11: Standard Test Method for Direct Shear Test of Soils Under Consolidated Drained Conditions*. 2012.

20. Maine Department of Transportation, *Standard Specifications*. 2002.

21. ASTM International, *ASTM Standard D6913-04 (09): Standard Test Methods for Particle-Size Distribution (Gradation) of Soils Using Sieve Analysis*. 2004: West Conshohocken, PA.

22. ASTM International, *ASTM Standard D854-10: Standard Test Method for Specific Gravity of Soil Solids by Water Pycnometer*. 2010: West Conshohocken, PA.

23. ASTM International, *ASTM Standard D4253-00 (06): Standard Test Methods for Maximum Index Density and Unit Weight of Soils Using a Vibratory Table*. 2006: West Conshohocken, PA.

24. ASTM International, *ASTM Standard D1557 -12: Standard Test Methods for Laboratory Compaction Characteristics of Soil Using Modified Effort (56,000 ft-lbf/ft3 (2,700 kN-m/m3))*. 2012: West Conshohocken, PA.

25. ASTM International, *ASTM Standard D4254-00 (06): Standard Test Method for Minimum Index Density and Unit Weight of Soils and Calculation of Relative Density*. 2006: West Conshohocken, PA.

26. ASTM International, *ASTM Standard D4318-10: Standard Test Method for Liquid Limit, Plastic Limit, and Plasticity Index of Soils*. 2010: West Conshohocken, PA.

27. O'Rourke, T., Druschel, S., and Netravali, A., *Shear strength characteristics of sand-polymer interfaces.* Journal of geotechnical engineering, 1990. **116**(3): p. 451-469.

28. Mirmiran, A., Shao, Y., and Shahawy, M., *Analysis and field tests on the performance of composite tubes under pile driving impact.* Composite Structures, 2002. **55**(2): p. 127-135.

29. Sakr, M., Naggar, M.H.E., and Nehdi, M., *Novel toe driving for thin-walled piles and performance of fiberglass-reinforced polymer (FRP) pile segments.* Canadian geotechnical journal, 2004. **41**(2): p. 313-325.

30. Iyer, S., *The Feasability Study on Glass Fiber Reinforced Polymer (GFRP) Tubes Filled with Concrete for Pile/Column for Bridges*, Ohio Department of Transportation, Editor. 2001.

31. Guades, E. and Aravinthan, T., *Residual properties of square FRP composite tubes subjected to repeated axial impact.* Composite Structures, 2013. **95**: p. 354-365.

32. Baxter, C.D., et al., *Field Study of Composite Piles in the Marine Environment*, University of Rhode Island Departments of Ocean/Civil and Environmental Engineering, Editor. 2005. p. 68.

33. Profound BV, *TNOWAVE Wave Equation Program, Unknown Version.* n.d.

34. Lawrence, D., et al., *FRP Composite Pile Driving at the Richmond-Dresden Bridge over the Kennebec River.* 2014, University of Maine Advanced Structures and Composites Center.

35. Maine Department of Transportation, *Geotechnical Design Report for the Replacement of: Maine Kennebec Bridge, Route 197 over Kennebec River, Richmond and Dresden, Maine*, L. Krusinski and K. Maguire, Editors. 2012.

36. Maine Test Borings, *Richmond-Dresden Supplementary Borings.* 2013.

37. Delmag, *Diesel Pile Hammer Technical Data.* 2010.

38. Pile Dynamics Inc., *Case pile Wave Analysis Program (CAPWAP), Unknown Version.* n.d.

39. Pile Dynamics Inc., *Pile Driving Analyzer (PDA), Unkown Version.* n.d.

40. GZA GeoEnvironmental Inc., *EOD HarborPile Pile Driving Report.* 2013: Norwood, MA.

41. GZA GeoEnvironmental Inc., *Dynamic Pile Restrike Testing Results - HarborPile Test Program.* 2013: Norwood, MA.

42. Maine Department of Transportation, *Pile Driving Logs - EOD.* 2013.

43. Maine Department of Transportation, *Pile Driving Logs - Restrike.* 2013.

44. Hannigan, P.J., et al., *Design and Construction of Driven Pile Foundations*, F.H. Administration, Editor. 2006.

45. American Concrete Institute, *Building Code Requirements for Structural Concrete (ACI 318M-08) and Commentary*. 2008.

46. Canadian Plywood Association, *Material Safety Data Sheet: CANPLY Exterior Plywood*. 2013.

47. Helmi, K., Fam, A., and Mufti, A., *Field Installation, splicing, and flexural testing of hybrid FRP/Concrete piles.* ACI Special Publication, 2005. **230**.

48. Fam, A.Z. and Rizkalla, S.H., *Flexural behavior of concrete-filled fiber-reinforced polymer circular tubes.* Journal of Composites for Construction, 2002. **6**(2): p. 123-132.

49. Ahmad, I., Zhu, Z., and Mirmiran, A., *Behavior of short and deep beams made of concrete-filled fiber-reinforced polymer tubes.* Journal of Composites for Construction, 2008. **12**(1): p. 102-110.

50. Davol, A., Burgueno, R., and Seible, F., *Flexural behavior of circular concrete filled FRP shells.* Journal of structural engineering, 2001. **127**(7): p. 810-817.

51. Cole, B. and Fam, A., *Flexural load testing of concrete-filled FRP tubes with longitudinal steel and FRP rebar.* Journal of Composites for Construction, 2006. **10**(2): p. 161-171.

52. Helmi, K., Fam, A., and Mufti, A., *Behavior of concrete filled FRP tubes under fully reversed cyclic bending.* Arabian Journal for Science and Engineering, 2006. **31**(1): p. 215.

53. Ahmad, I., Zhu, Z., and Mirmiran, A., *Fatigue behavior of concrete-filled fiber-reinforced polymer tubes.* Journal of Composites for Construction, 2008. **12**(4): p. 478-487.

54. Zhu, Z., Ahmad, I., and Mirmiran, A., *Fatigue Modeling of Concrete-Filled Fiber-Reinforced Polymer Tubes.* Journal of Composites for Construction, 2009. **13**(6): p. 582-590.

55. ASTM International, *ASTM Standard D2584-11: Standard Test Method for Ignition Loss of Cured Reinforced Resins*. 2011: West Conshohocken, PA.

56. American Association of State Highway and Transportation Officials, *AASHTO LRFD Guide Specifications for Design of Concrete-Filled FRP Tubes for Flexural and Axial Members*. 2012.

57. American Concrete Institute, *Prediction of Creep, Shrinkage, and Temperature Effects in Concrete Structures*, A.C. 209, Editor. 1992, American Concrete Institute.

59. Chin, J.W., Nguyen, T., and Aouadl, K., *Effects of environmental exposure on fiber-reinforced plastic (FRP) materials used in construction.* Journal of Composites Technology and Research, 1997. **19**: p. 205-213.

60. Guzman, V.A. and Brøndsted, P., *Effects of moisture on glass fiber-reinforced polymer composites.* Journal of Composite Materials, 2014: p. 0021998314527330.

61. Hongwang, Q. and Huang, G., *Mechanical behaviors of glass/polyester composites after UV radiation.* Journal of Composite Materials, 2011. **45**(19): p. 1939-1943.

62. Pando, M., et al. *Durability of concrete-filled tubular FRP piles.* in *The 3rd Int. Conf. on Composites in Infrastructure, ICCI.* 2002.

63. Shokrieh, M.M. and Bayat, A., *Effects of Ultraviolet Radiation on Mechanical Properties of Glass/Polyester Composites.* Journal of Composite Materials, 2007. **41**(20): p. 2443-2455.

64. Afshar, A., et al., *Effect of long-term exposure to marine environments on the flexural properties of carbon fiber vinylester composites.* Composite Structures, 2015. **126**: p. 72-77.

65. ASTM International, *ASTM Standard G154-12a: Standard Practice for Operating Fluorescent Ultraviolet (UV) Lamp Apparatus for Exposure of Nonmetallic Materials.* 2012: West Conshohocken, PA.

66. ASTM International, *ASTM Standard C666-03 (08): Standard Test Method for Resistance of Concrete to Rapid Freezing and Thawing.* 2008: West Conshohocken, PA.

67. Navy, U., *Design Manual: Foundations and Earth Structures.* 1986, NAVFAC DM7.

BIOGRAPHY OF THE AUTHOR

Dale Lawrence was born in Harrisburg, PA on May 29, 1990. He is the son of Richard and Jane Lawrence, and grandson of Walter and Vera Lawrence and William and Louise Kerrigan. He grew up in Hershey, PA where he attended Lower Dauphin High School. While enrolled in high school, he became captain of the football team and played lacrosse before graduating in 2009.

Dale attended the University of Maine and graduated with a Bachelor of Science degree in Civil Engineering in 2009. During his undergraduate career, he maintained an internship with the Pennsylvania Department of Transportation. He returned to the University of Maine to pursue a Master's degree in Civil and Environmental Engineering with a focus in geotechnical engineering.

Dale is a candidate for the Master of Science degree in Civil Engineering from The University of Maine in May 2015.